Spring 2023

CRYSTAL PLASTICITY FINITE ELEMENT MODELING OF MAGNESIUM ALLOYS AND EXPERIMENTAL CHARACTERIZATION OF A TRIP HIGH ENTROPY ALLOY

Jacob Weiss
University of New Hampshire, Durham

CRYSTAL PLASTICITY FINITE ELEMENT MODELING OF MAGNESIUM ALLOYS AND EXPERIMENTAL CHARACTERIZATION OF A TRIP HIGH ENTROPY ALLOY

BY

Jacob Daniel Weiss

B.S. Mechanical Engineering, University of New Hampshire, 2020

THESIS

Submitted to the University of New Hampshire in Partial Fulfillment of the Requirements for the Degree of

Master of Science in Materials Science

May 2023

THESIS COMMITTEE PAGE

This thesis/dissertation is to be examined and approved in partial fulfillment of the requirements for the degree of

Master of Science in Materials Science by:

Marko Knezevic, Professor of Mechanical Engineering

Todd Gross, Professor of Mechanical Engineering

Igor Tsukrov, Professor of Mechanical Engineering

On April 21st, 2023

Approval signatures are to be on file with the University of New Hampshire Graduate School.

Table of Contents

Contents

Table of Contents iii

Acknowledgements vi

Abstract vii

Introduction 1

Chapter 1: Embedding strain-rate sensitivities of multiple deformation mechanisms to predict the behavior of a precipitate-hardened WE43 alloy under a wide range of strain rates 3

Abstract 4

1. Introduction 6

2. Experimental background 10

2.1 *Material* 10

2.2 Suite of mechanical testing 11

3. Multiscale model for precipitate hardened hcp Mg alloy 14

3.1 T-CPFE 14

3.2 Slip and twinning systems in WE43 17

3.3 Twin domains within grains 18

3.4 Incorporating two types of strain rate sensitivities 18

3.4.1 Constant structure SRS 19

3.4.2 Evolving structure SRS: model for slip and twin resistances 21

3.5 Initial slip resistance for slip and twinning 23

3.6 Contribution of precipitate shearing to slip resistance 24

3.7 DFT calculations of the APB energy in precipitates in WE43-T6 26

3.8 Characterizing the slip resistance parameters 28

3.9 Taylor cylinder impact test model setup 30

4. Results 31

4.1 Rate sensitivities. 31

4.2 Hardening parameters. 32

4.3 Slip and twinning activities during monotonic testing 36

4.4 Predicting microstructure evolution at even higher rates of strain 40

5. Discussion 53

6. Conclusions 54
Acknowledgements 55
References 55
Chapter 2: A parametric study into the influence of Taylor-type scale-bridging artifacts on accuracy of multi-level crystal plasticity finite element models for Mg alloys 66
Abstract 67
1. Introduction 69
2. Modeling framework 73
2.1 T-CPFE formulation 74
2.2 Finite element model meshes 78
3. Experimental data 82
4. Results 83
4.1 Effects of homogenization scheme at 2% strain 84
4.2 Large strain behavior 87
5. Discussion 92
6. Conclusion 96
Acknowledgements 97
Appendix A 97
References 99
Chapter 3: Assessing strength of phases in a quadruplex high entropy alloy via high-throughput nanoindentation to clarify origins of strain hardening 109
Abstract 110
1. Introduction 112
2. Experimental Procedures 115
2.1 Material processing 115
2.2 Mechanical testing 115
2.3 Microstructural characterization 116
2.4 Nanoindentation 117
3. Results 119
3.1 Mechanical testing for overall properties 119
3.2 Microstructural characteristics 120
3.3 Correlated EBSD and nanoindentation mapping for local properties 128
4. Discussion 132
5. Conclusions 136

Acknowledgements 138
Appendix 138
References 140
Conclusions and Future Work 147

Acknowledgements

I’d like to thank my advisor, Marko Knezevic, for the research opportunity he granted me over the last three years. The research experience I gained made me a more well-rounded engineer and will allow me to reach for opportunities that were not open before. I’d also like to thank my fellow graduate students, Dan Savage, Nemanja Kljestan, Evgenii Vasilev, and Nikolai Matukno, and the UIC for their guidance, support and help along the way. And of course, I’d like to thank my family and friends for their support.

Abstract

This work presents two crystal plasticity finite element studies on magnesium alloys and an experimental characterization of a high entropy alloy. The first of two crystal plasticity studies presents a high strain rate deformation characterization via a split Hopkinson bar Taylor impact of a WE43 magnesium alloy. This study showed that crystal plasticity finite element modeling (CPFE) was able to model WE43 texture evolution, twin volume fraction along the length of the cylinder, and anisotropy with four different material orientations at high strain rates when compared to experimental data. The second study investigated the Taylor-type model homogenization response of the virtual polycrystal and how to best spread the crystal orientations over the finite element (FE) mesh for accurate modeling of Mg alloys specifically AZ31. It was found that 6 embedded crystals per integration point proved most optimal when compared to a full-field explicit grain mesh model. The third study investigated phase transformation hardness values and strain hardening characteristics for a four-phase high entropy alloy by nanoindentation. The material exhibited great strength based on phase transformation during plastic deformation upon compression.

Introduction

Crystal plasticity is a mesoscale crystallographic technique used to model mechanical behavior of polycrystalline materials. From this, the relationship between stress and strain can be rationalized by capturing the underlying physics at the crystal level. All three studies presented here utilize the understanding of crystal plasticity either computationally or experimentally. Here, all three materials investigated have hexagonal close packed phases which are captured experimentally by EBSD (electron backscatter diffraction) for a HEA, and modeled computationally by crystal plasticity finite element modeling for two magnesium alloys. Crystal plasticity finite element modeling uses constitutive laws at the mesoscale to successfully characterize materials based upon experimentally obtained data.

For the first two chapters of this thesis, crystal plasticity finite element modeling was used to characterize and model WE43 and AZ31 magnesium alloys. The work uses a recently developed multi-level constitutive model for polycrystalline metals which deform by elasticity, crystallographic slip, and deformation twinning.

The first chapter presents a comprehensive set of mechanical and microstructure data recorded during quasi-static, high strain rate split Hopkinson bar, and impact tests on specimens of WE43 Mg. The experiment is simulated and interpreted using an advanced Taylor-type crystal plasticity finite element (T-CPFE) model. The T-CPFE model is formulated physically to embed two sources of strain-rate sensitivities inherent to each slip and twinning mode in WE43, one that occurs under constant structure and another that affects the structure evolution. After calibration and validation, the model proved to predict characteristics at larger strain rates than those used for model calibration. Specifically, mechanical response, specimen geometry changes, twin

volume fractions, and texture evolution are predicted for different orientations of the Taylor cylinders.

The second chapter of this thesis presents a parametric study into the influence of Taylor-type scale-bridging artifacts on the accuracy of crystal plasticity finite element modeling for Mg alloys. This work seeks to establish an optimal number of crystal orientations to spread over integration points for accurate modeling of Mg alloys. It was found that six crystals per integration point are optimal in smoothing local deformation while allowing heterogeneous deformation over the mesh.

The third and final chapter focuses on the experimental analysis of a TRIP high entropy alloy (HEA) $Fe_{42}Mn_{28}Co_{10}Cr_{15}Si_5$ (in at%), using rolling and compression. Nanoindentation, optical microscopy, and electron backscatter diffraction (EBSD) were used to characterize the present microstructure at different levels of deformation to fracture allowing for hardness parameters to be characterized per phase over increasing levels of strain. Strain hardening characteristics of the material are clarified.

Chapter 1: Embedding strain-rate sensitivities of multiple deformation mechanisms to predict the behavior of a precipitate-hardened WE43 alloy under a wide range of strain rates

This chapter has been submitted to the International Journal of Plasticity on April 10th, 2023, and is currently under review.

My contribution to this work was to model WE43 high strain rate Taylor impact simulations for four initial material orientations. After simulations were complete, I post processed the obtained data and produced figures (1,2,5,8,9,10,11,12,13,14,15) in the paper. The text was written in a standard student-mentor relationship along with contributions from University of California, Santa Barbara, Utah State University, and DEVCOM Army Research Laboratory.

Embedding strain-rate sensitivities of multiple deformation mechanisms to predict the behavior of a precipitate-hardened WE43 alloy under a wide range of strain rates

Jacob Weiss[a], Yanqing Su[b], Brandon A. McWilliams[c], Irene J. Beyerlein[d], and Marko Knezevic[a,*]

[a]Department of Mechanical Engineering, University of New Hampshire, Durham, NH 03824, USA.

[b]Department of Mechanical and Aerospace Engineering, Utah State University, Logan UT 84322-4130, USA.

[c]Army Research Directorate, DEVCOM Army Research Laboratory, Aberdeen Proving Ground, MD 21005, USA.

[d]Department of Mechanical Engineering, Materials Department, University of California, Santa Barbara, Santa Barbara, California 93106-5070, USA.

*Corresponding author: E-mail address: marko.knezevic@unh.edu (M. Knezevic).

Abstract

A rare earth Mg alloy, WE43, exhibits high strength, good ductility, and low anisotropy and strain rate sensitivity. As such, the alloy is a viable candidate for high strain rate applications. In this

work, a comprehensive set of mechanical and microstructure data recorded during quasi-static, high strain rate split Hopkinson bar (SHB), and impact tests on specimens of WE43 Mg alloy reported in (Savage et al., 2020) is simulated and interpreted using an advanced Taylor-type crystal plasticity finite element (T-CPFE) model. The T-CPFE model is formulated physically to embed two sources of strain-rate sensitivities inherent to each slip and twinning mode in WE43, one that occurs under constant structure and another that affects structure evolution. The model parameters are established for the alloy by achieving agreement in the stress-strain response and microstructure evolution under quasi-static and SHB tests. Density functional theory calculations of anti-phase boundary (APB) energy are carried out to explain origins of the unusually large initial slip resistance for basal dislocations, which shear precipitates in the alloy. The initial slip resistances of the prismatic and pyramidal dislocations are, instead, rationalized by Orowan looping around precipitates. After calibration and validation, the model is shown to successfully predict WE43 response at much larger strain rates than those used for model calibration. Specifically, mechanical response, specimen geometry changes, twin volume fractions, and texture evolution are predicted for different orientations of the Taylor cylinders. Details of the modeling framework, comparison between simulation and experimental results, and insights from the results are presented and discussed.

Keywords: WE43; Impact; Microstructures; Crystal Plasticity; T-CPFE

1. Introduction

Structural Mg alloys, such as WE43, have received much attention for its combined lightweightness and high strength (Bhattacharyya et al., 2016; Imandoust et al., 2017). While advantageously less dense, Mg alloys are generally relatively weak compared to conventional steel and Al alloys. With the T6 age-hardening treatment, the Mg WE43-T6 alloy exhibits relative high strength due to the formation of precipitates (Bhattacharyya et al., 2018; Kandalam et al., 2015). Among many experimental studies, the deformation response and strength of WE43 over a wide range of strain rates, from quasi-static 10^{-4}/s to 10^{6}/s, have been studied (Xiang et al., 2018). It is found that WE43 in the T6 condition exhibits good ductility, low plastic anisotropy and tension/compression asymmetry, and little strain rate sensitivity in these properties, all outstanding properties that make it a good candidate for many high strain rate, high impact applications (Agnew et al., 2014; Miraglia et al., 2007). These properties are a consequence of precipitates, which effect the ratio between the activation stress for basal, prismatic, and pyramidal dislocations (Nie, 2012; Nie and Muddle, 2000). Because the ratios are reduced compared to other Mg alloys like AZ31 (Kabirian et al., 2015), slip systems belonging to different modes can activate simultaneously. Reduced twinning activity in WE43 reduces asymmetry and propensity to strain localizations. Texture intensity in these alloys is only moderately strong influencing small anisotropy. These attributes are uncommon for Mg alloys and other hexagonal close packed (hcp) metallic alloys in general, which usually are greatly plastically anisotropic. To date, WE43 is commercially available and in use in structural applications, such as components in lightweight armored ground vehicles, helicopter rotor heads, and even orthopedic implants (Cho et al., 2009; Liu et al., 2022). The alloy has good vibration damping capacity (Sugimoto et al., 1977) as well as low acoustic impedance

characteristics (Martin et al., 2006). These properties can additionally benefit the vehicle applications. The alloy can also be processed by additive manufacturing (Gangireddy et al., 2019).

One pressing issue with WE43 is that while clearly a structurally desirable material, its deformation behavior is challenging to understand and predict. The reasons for its unusually superior performance, such as low anisotropy and relatively law strain rate sensitivity are attributed to precipitates, but details are yet to be clarified. WE43, like most low symmetry hcp metals, deforms simultaneously by multiple slip and twin modes (Yoo, 1981). The macroscopic response of WE43 consequently is the result of a complex set of interactions between slip, twinning, and the precipitates and the microstructure evolution changes their activity and interactions. Each of these mechanisms have an individual dependency on strain rate (Korla and Chokshi, 2010; Watanabe and Ishikawa, 2009) and how their operation leads to macroscopic strain rate sensitivity and anisotropy is unclear. Expanding the use of WE43 in critical, high-impact applications such as in aerospace components and defense armor, relies on predicting changes in its response as the rate of strain changes. Further, especially in the higher strain-rate conditions, the material can experience high levels of strain and substantial microstructural changes, such as changes in texture, formation of twins, and accumulated stored dislocation density (Feather et al., 2019). Many of these high-strain-rate situations involve multi-axial loading as well. These high rates and multi-axial conditions are often challenging to mimic in high-throughput laboratory tests. Most laboratory tests involve simple test geometries, such as bars or cylinders, and under uniaxial loading (Follansbee, 1985; Maudlin et al., 1999).

To link laboratory to structural situations, one approach often taken is to employ a model that is calibrated with the simpler laboratory tests and can be used to simulate these more complex conditions encountered in application (Knezevic et al., 2016a). To relate the deformation

mechanism activity and microstructural evolution in materials like WE43, crystal plasticity (CP) theory-based modeling is essential. Generally, for modeling polycrystalline material deformation, CP formulations have been employed in either mean-field polycrystal plasticity models (Lebensohn and Tomé, 1993) or full field models, such as finite element (FE) (Kalidindi et al., 1992; Knezevic et al., 2014b) or fast-Fourier transform (FFT) (Eghtesad et al., 2020; Lebensohn et al., 2012). For many Mg alloys and WE43, crystal plasticity based constitutive laws have been developed that account for multiple mode activity, evolve the hardening in the deformation mechanisms, such as slip and twinning, and evolve the microstructure, such as grain shape changes, twin lamellae reorientation, and texture (Nugmanov et al., 2018; Proust et al., 2007). In more recent times, models have been advanced to treat the interaction of slip with precipitates, essential for precipitation hardened alloys (Ghorbanpour et al., 2017). To simulate high strain rate deformation, models are applied to uniaxial laboratory test data first, such as quasi-static tests or split Hopkinson bar (SHB) tests (Jahedi et al., 2018a; Knezevic et al., 2013; Zecevic and Knezevic, 2018). To achieve a range of strain rates, both the former traditional compression tests and the SHB tests are included in the testing suite and these tests are repeated at different strain rates (Chen and Gray, 1996; Livescu et al., 2016). The models are typically demonstrated to predict material behavior within the same strain rate regime as it was calibrated.

An ideal test for characterizing material behavior for a broad range of ultra-high strain rates in one sample, and for advancing a model accuracy in the high strain rate regime is the Taylor cylinder (TC) impact test (Maudlin et al., 1999; Takajo et al., 2018). The TC test propels at high velocity cylindrical sample at a rigid target. A variation of high rates in the range of 10^6/s can be achieved along the length of the TC (Feng et al., 2022; Zecevic et al., 2016). The TC is challenging to simulate in FE frameworks. For WE43, a series of TC tests have been conducted and its post-

deformation microstructure examined finding significant changes in texture, grain shape, and deformation twinning (Savage et al., 2020). The well-known disadvantage of the TC test is that it cannot provide a stress-strain curve, usually used to calibrate a model. Thus, a model that can successfully simulate the constitutive response of the TC test as well as the stress-strain response is the common way to circumvent this problem (Vasilev et al., 2020).

Modeling the TC test has been mainly accomplished using FE frameworks, although smooth particle hydrodynamics (SPH) methods can be used (Eghtesad and Knezevic, 2018). The advantage of a full field mechanics model like the FE method is that it can predict the time evolution and spatially heterogeneous mechanical fields during the TC. To simulate strain rate effects on microstructural evolution in the TC test, however, an FE model incorporating a CP formulation is needed to predict slip patterns, and texture and twinning evolution. A full CPFE formulation of the temporal and spatial mechanical fields over the period and specimen of the TC tests would be too computationally intensive, particularly when testing multiple conditions, material types and orientations are required. One approach to reduce computation time is to simulate the TC test using standard FE and use the output as boundary conditions for subsequent, separate CP calculations (Knezevic et al., 2009; Savage and Knezevic, 2015). This handshaking approach for hcp alloys is less desirable since the mechanical fields are inherently tied to microstructure evolution and deformation mechanisms. To provide concurrent CP evolution in a polycrystal and heterogeneous 3D fields in a computationally efficient manner, a model considering a Taylor-type homogenization at each integration point in a finite deformation crystal plasticity finite element model, called T-CPFE, was developed (Ardeljan et al., 2016). T-CPFE aims to link crystal deformation accommodated by multiple slip and twinning modes to a Taylor-type polycrystal. In previous work (Feather et al., 2019), the T-CPFE model was applied to model

the deformation behavior of the WE43 alloy in uniaxial testing (Feather et al., 2019) but never to simulate a TC test.

In this work we present a multiscale model for hcp metals that builds on the T-CPFE approach. The goal is to advance its formulation such that it can extrapolate to much higher strain rates, such as in a TC test, than those used to calibrate it. To do so, the formulation considers two sources of strain rate sensitivity for each slip and twinning system, one that occurs under constant structure and another that is a consequence of evolving structure. As a second advancement to T-CPFE, it indirectly considers the response of each slip mode to either precipitate shearing or bowing. With WE43, we demonstrate that the advanced multi-level T-CPFE can be calibrated using quasi-static to medium rate SHB tests and accurately predict the texture evolution, twinning evolution and dimensional shape changes at any spatio-temporal location in the specimen undergoing TC testing.

2. Experimental background

2.1 *Material*

The WE43 used in the present study was age-hardened according to the T6 treatment. T6 consists of a solution treatment step at 536 °C for 24 h and an aging step at 205°C for 48 h (Jahedi et al., 2018b; Jiang et al., 2017). The solution treatment step leads to static recrystallization and the aging step provides a favorable size and distribution of precipitates. The condition allows for higher strain-rates to be probed by TC tests and for constitutive model development.

2.2 *Suite of mechanical testing*

For model development and validation, we make use of a comprehensive set of data containing quasi-static, high strain rate, and impact deformation of WE43 Mg alloy, all reported in (Savage et al., 2020). The data are briefly reviewed below.

Compression tests were performed at room temperature at quasi-static strain rates of 0.001 /s. Specimens were made from a rolled plate in three directions: rolling direction (RD), transverse direction (TD), and normal direction (ND). Stress-strain curves will be shown later. Figure 1 shows the measured initial textures represented by three pole figures in the four specimen orientations (Savage et al., 2020). The measurements were performed using neutron diffraction (NeD) in High-Pressure-Preferred Orientation (HIPPO) diffractometer at Los Alamos National Laboratory. The basal poles of the grains are strongly aligned along the ND. The compression direction with respect to the oriented basal pole thus varies for these four orientations, with ND sample directly compressing the poles. Since there is a wide spread of the poles about the ND slightly tilted in RD, the orientation relationship between the compression direction and the other three samples are similar. In the model, these textures are used in the simulations and embedded at every integration point of the FE meshes as represented using 152 weighted orientations using the procedure described in (Eghtesad et al., 2018).

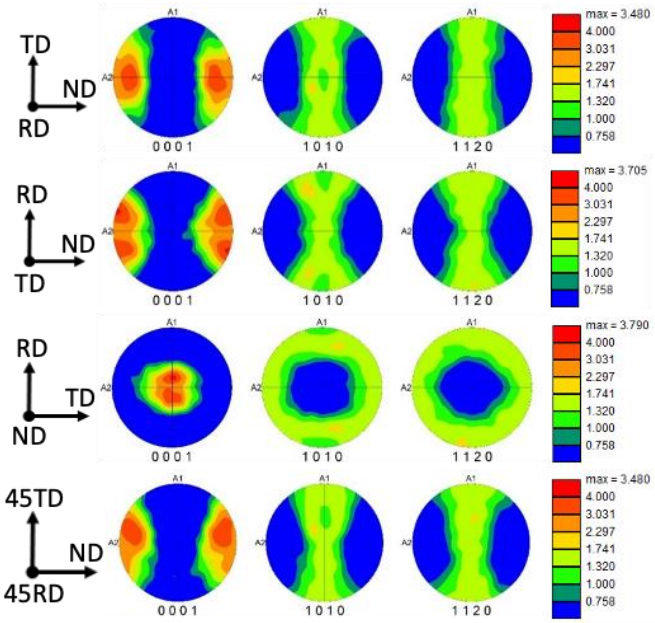

Fig. 1. Pole figures measured by NeD showing the initial texture in the specimens of WE43-T6 alloy. The specimens are compressed along the axis perpendicular to the pole figures.

For the stress-strain response at higher strain rates, SHB testing was carried out. A few specimens were tested along the TD direction at strain-rates between 523 /s and 2544 /s. Taylor cylinder specimens were machined from the rolled WE43-T6 plate such that the cylinder axis aligned either with RD, TD, ND, or in-plane 45° from the RD, of the plate. The length of the cylinders ranged from 36.83 mm to 38.40 mm and the diameter was 7.57 mm, respectively. The cylinders are launched as a projectile toward a steel target. The velocity of the shot studied ranged from 181.6 to 192.3 m/s. Table 1 summarizes the geometry of the four cylinders and their impact conditions.

Table 1. Axes of cylinders relative to the frame of the WE43-T6 plate, imposed velocities, initial dimensions, and final lengths after the impacts for the four Taylor cylinders.

Cylinder axis	Velocity (m/s)	Initial length (mm)	Initial diameter (mm)	Final length (mm)
RD	188.1	38.40	7.57	35.96
TD	181.6	38.18	7.57	36.03
ND	192.3	36.83	7.57	34.47
45RD	188.1	38.23	7.57	35.82

Bulk texture evolution in all TCs after the impacts was measured using NeD. Figure 2 highlights the many locations along a representative TC sample where the measurements are made. Upper-bound estimates of the twin volume fractions for the $\{10\bar{1}2\}\langle10\bar{1}\bar{1}\rangle$ tension twins were determined from the textures. The data will be presented later. The element sets from which texture was exported for comparisons of measured and simulated texture evolution are also shown in the figure.

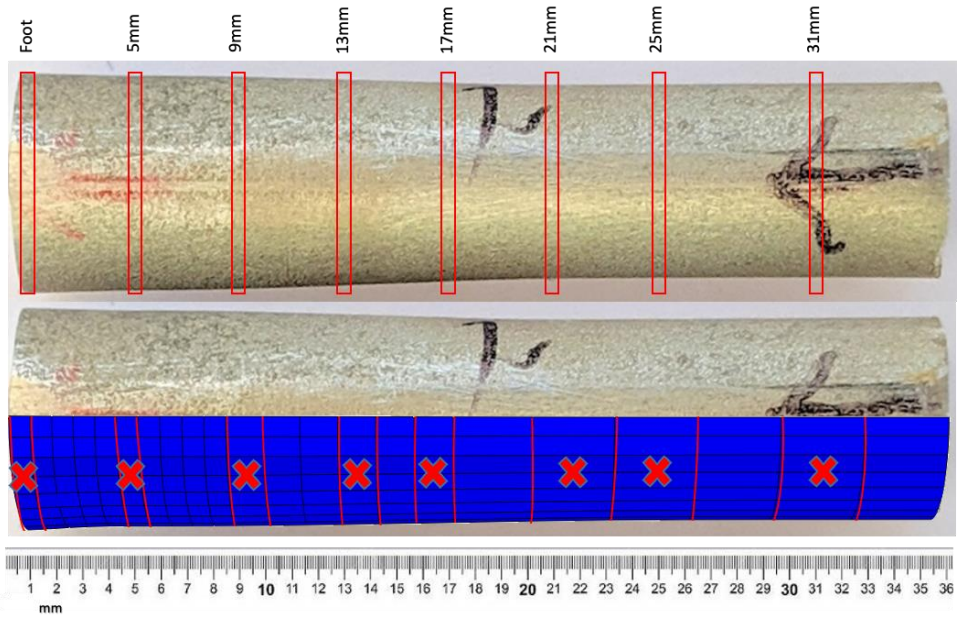

Fig. 2. Regions of 2 mm in width identifying locations where texture measurements by NeD in HIPPO along each Taylor cylinder were performed. Corresponding element sets used to export texture from the models for comparisons of measured and simulated texture evolution.

3. Multiscale model for precipitate hardened hcp Mg alloy

3.1 T-CPFE

In the present work, we use T-CPFE, a model that combines the full-field finite element and Taylor-type crystal plasticity models (Ardeljan et al., 2016). The first meso-scale level of homogenization is performed using the full-constraints Taylor model (T-), while the second macroscopic level of homogenization is performed using finite elements. The second level of the homogenization is relaxing the intrinsic assumption of the Taylor model pertaining to the iso deformation gradient or iso velocity gradient applied over a polycrystal. Each FE integration point represents a subset of grains belonging to the sub-polycrystal. T-CPFE is a multi-scale model that

links deformation of individual grains, accommodated by slip/twinning, at the microscale to a Taylor-type polycrystal at each integration point of the FE mesh at the macro scale. The advantage of T-CPFE over the Taylor-type homogenization is that it can simulate geometrical changes and inhomogeneous deformation, such as in the TC tests of interest here. The advantage of T-CPFE over full-field CPFE is that many more grains can be simulated with less computation time. In prior work, the T-CPFE model was used to predict and interpret the deformation behavior of WE43 alloy in (Feather et al., 2019). Subsequently, the model was later advanced to consider strain-rate sensitivities inherent to deformation mechanisms in (Feather et al., 2021) to enable modeling of high strain rate deformation of alloys. Here we further advance it to consider two distinct types of strain rate sensitivities and precipitates. In the remainder of this section, the different components of this newer version are presented.

In the description that follows, tensor quantities are denoted as bold; tensor components and scalars are made italic and not bold; indices s, α, t, and β are used for slip systems, slip modes, twin systems, and twin modes, respectively; $\cdot$ is used to denote a dot product, while $\otimes$ is a tensor product. N^{sl} and N^{tw} will be the total number of slip and twin systems.

The T-CPFE model is a user material subroutine (UMAT) implemented in Abaqus. In this type of implementation, the implicit FE solver iteratively provides a guess of the displacement field at time, τ (t+Δt), given the boundary conditions over the FE model. To this end, a deformation gradient, $\mathbf{F}$, is used to interrogate the UMAT for each gauss at each FE integration point. The UMAT solves for the Cauchy stress, $\overline{\boldsymbol{\sigma}}$, and provides the Jacobian along with updated set of state variables. The solution procedure moves on to the next time increment if the given boundary conditions and stress equilibrium are satisfied. The Cauchy stress at each integration point is taken as a volume average of crystal stresses in grains and twins as

$$\bar{\boldsymbol{\sigma}} = \langle \boldsymbol{\sigma} \rangle = \sum_{k=1}^{N_{grains}} \nu_k \boldsymbol{\sigma}_k \ , \tag{1}$$

where k enumerates grains and twins, ν are weights, and $\langle\ \rangle$ denotes the volume average.

Grains and twins embedded at a given FE integration point undergo the same applied deformation gradient, $\mathbf{F}$, according to the Taylor-type model assumption. The tensor $\mathbf{F}$ is multiplicatively decomposed into its elastic and plastic parts as

$$\mathbf{F} = \mathbf{F}^e \mathbf{F}^p. \tag{2}$$

The rate of change of $\mathbf{F}^p$ is

$$\dot{\mathbf{F}}^p = \mathbf{L}^p \mathbf{F}^p. \tag{3}$$

Integrating the above equation from the time at the beginning of the given strain increment, t, to the end of it, $\tau = t+\Delta t$, yields

$$\mathbf{F}^p(\tau) = exp(\mathbf{L}^p(\tau)\Delta t)\mathbf{F}^p(t). \tag{4}$$

The constitutive relations at the grain level are

$$\mathbf{T} = \mathbf{C}\mathbf{E}^e, \text{ with } \mathbf{T} = \mathbf{F}^{e^{-1}}\{(det\mathbf{F}^e)\boldsymbol{\sigma}\}\mathbf{F}^{e^{-T}} \text{ and } \mathbf{E}^e = \frac{1}{2}\{\mathbf{F}^{e^T}\mathbf{F}^e - \mathbf{I}\}, \tag{5}$$

in which, $\mathbf{T}$ is the second Piola-Kirchhoff stress, $\mathbf{E}^e$ is the Lagrangian strain, and $\mathbf{C}$ is the fourth-order elasticity tensor. The elasticity tensor per grain is calculated based on C_{11} = 59,500 MPa, C_{12} = 26,100 MPa, C_{13} = 21,800 MPa, C_{33} = 65,600 MPa, C_{44} = 16,300 MPa crystal constants for Mg (Duvvuru et al., 2007; Knezevic and Kalidindi, 2007; Landry and Knezevic, 2015; Slutsky and Garland, 1957).

To obtain stress, $\mathbf{F}^e$ must be obtained first using $\mathbf{F}^e(\tau) = \mathbf{F}\mathbf{F}^{p^{-1}}(\tau) = \mathbf{F}\mathbf{F}^{p^{-1}}(t)\{\mathbf{I} - \Delta t\mathbf{L}^p(\tau)\}$ for what $\mathbf{L}^p$ must be known. $\mathbf{L}$, corresponding to $\mathbf{F}$, is additively decomposed to its plastic part, $\mathbf{L}^p$, and elastic part, $\mathbf{L}^e$. The former accounts for plasticity accommodated by slip and twinning as

$$\mathbf{L} = \mathbf{L}^e + \mathbf{L}^p = \mathbf{L}^e + \mathbf{L}^{sl} + \mathbf{L}^{tw} = \mathbf{L}^e + \sum_s^{N^{sl}} \dot{\gamma}^s \mathbf{S}_0^s + \sum_t^{N^{tw}} \dot{f}^t S^t \mathbf{S}_0^t, \quad (6)$$

in which $\mathbf{S}_0^s = \mathbf{b}_0^s \otimes \mathbf{n}_0^s$ and $\mathbf{S}_0^t = \mathbf{b}_0^t \otimes \mathbf{n}_0^t$ are Schmid tensors for slip, *s*, and twinning, *t*, in the reference configuration, $_0$. These tensors are based $\mathbf{b}_0^s$ and $\mathbf{b}_0^t$ representing Burgers vectors and $\mathbf{n}_0^s$, and $\mathbf{n}_0^t$ representing plane normal vectors. Moreover, $\dot{\gamma}^s$ is the rate of shearing, S^t is the intrinsic shear strain for twin systems, and $\dot{f}^t = \frac{\dot{\gamma}^t}{S^t}$ is the rate of change of twin volume fraction (Kalidindi, 1998; Van Houtte, 1978).

3.2 Slip and twinning systems in WE43

The model formulation requires assigning a set of available slip and twinning modes. For WE43, we use modes that have been reported in experiments and these are: basal <a> $\{0001\}\langle\bar{1}\bar{1}20\rangle$, prismatic <a> $\{\bar{1}100\}\langle\bar{1}\bar{1}20\rangle$, and pyramidal <c+a> type I $\{10\bar{1}1\}\langle11\bar{2}\bar{3}\rangle$ and type II $\{\bar{1}\bar{1}22\}\langle11\bar{2}3\rangle$. The twinning modes made available to the calculations here are c-axis extension twinning $\{10\bar{1}2\}\langle10\overline{\bar{1}1}\rangle$ (TTW1), c-axis extension twinning $\{11\bar{2}1\}\langle11\overline{2\bar{6}}\rangle$ (TTW2), c-axis contraction twinning $\{10\bar{1}1\}\langle10\overline{\bar{1}2}\rangle$ (CTW), and double twinning $\{10\bar{1}1\}$-$\{10\bar{1}2\}\}$ (DTW). TTW1 twin shear is 0.1289 and its twin/matrix orientation relationship (OR) is 86˚ about the <$1\bar{1}20$> direction. TTW2 has a much larger twin shear of 0.6158 and the twin/matrix orientation

relationship is 34˚ about the <10$\bar{1}$0> direction. CTW has a twin shear of 0.1377 with an OR of approximately 56˚ about the same <1$\bar{1}$20> direction (Yoo, 1981).

3.3 Twin domains within grains

Formation of twin domains with the twin/matrix orientation within the grains is modeled via the composite grain formulation (Proust et al., 2007). Using CG, the formation of one or more twin variant domains in the same grain can be modeled. Each newly formed twin variant is a new grain undergoing the Taylor-type homogenization per FE integration point.

3.4 Incorporating two types of strain rate sensitivities

Most applications of crystal visco-plasticity theory adopt a viscoplastic power-law relationship to relate the shearing rates for slip and twinning, $\dot{\gamma}^s$ and $\dot{\gamma}^t$, to stress (Asaro and Needleman, 1985; Hutchinson, 1976; Kalidindi, 1998). The power-law form is the same for slip and twinning, with the key difference being that twinning is restricted to only the positive twin shearing sense). The power-law equation for slip systems, *s*, is only presented

$$\dot{\gamma}^s=\dot{\gamma}_0 \left(\frac{|\tau^s|}{\tau_c^s(\dot{\varepsilon},T)}\right)^{\frac{1}{m}} \text{sign}(\tau^s) \text{ with } \tau^s = \mathbf{T}\cdot\mathbf{S}_0^s, \quad (7)$$

where $\dot{\gamma}_0$ is a reference value of shearing rate ($\dot{\gamma}_0 = 0.001\ \text{s}^{-1}$), τ^s is the resolved shear stress on *s*, and τ_c^s is a value of slip system resistance to slip. The power-law exponent $\frac{1}{m}$ is inversely related to the strain rate sensitivity (SRS) m.

There are two types of rate sensitivities captured in the flow rule Eq. (7). One sensitivity is the constant structure sensitivity governed by the exponent $\frac{1}{m} = n$. It represents the SRS under a fixed slip resistance constant τ_c^s and constant dislocation density. The second sensitivity is referred to as the *evolving structure* sensitivity and pertains to rate sensitive evolution of the dislocation density. The present model aims to properly represent both sources of SRS.

3.4.1 Constant structure SRS

The SRS reduces as n increases. As $n \to \infty$ the shearing rates and stress become strain rate insensitive. Physically, $\frac{1}{m} = n$ can vary but the ease of converging on a solution can depend on it. First, if n is too small ($n < 20$), the selection of active slip systems can be not unique. Increasing the exponent beyond 20 does not change active slip systems, and thus does not change the direction of strain rate/stress but only the magnitude of the stress. Low values of the exponent (<100) are numerically easy to handle but cause significant issues when attempting to simulate high strain-rate deformation leading to unrealistically high values of stress (Knezevic et al., 2016b; Zecevic et al., 2016). In contrast high values of the exponent (>100) are numerically challenging to solve as the equations become extremely stiff but the strain-rate sensitivity values are realistic for alloys.

Overcoming these issues and allowing for constant structure sensitivity for a wide range of strain rate sensitivities are enabled using a recently developed numerical scheme referred to as the *k*-modification (*k*-mod) method (Knezevic et al., 2016b). The method was implemented in T-CPFE for AZ31 in (Feather et al., 2021). However, the model was not used to simulate a SRS response of a component until the present work. In the *k*-mod method, an applied plastic stretching tensor,

$\mathbf{D}^{app}$, available at each integration point, is modified to influence the magnitude of stress in grains as

$$\mathbf{D}^{p} = \frac{\mathbf{D}^{app}}{|\mathbf{D}^{app}|}|\mathbf{D}^{app}|^{\frac{1}{k+1}}, \tag{8}$$

where $\mathbf{D}^{p} = \frac{1}{2}\left(\mathbf{L}^{p} + \mathbf{L}^{pT}\right)$. The inverse relationship is:

$$\mathbf{D}^{app} = \mathbf{D}^{p}|\mathbf{D}^{app}|^{\frac{k}{k+1}} = \mathbf{D}^{p}|\mathbf{D}^{p}|^{k}. \tag{9}$$

Eqs. (8) and (9) imply that $\mathbf{D}^{p}$ attains unity as k increases. If we now consider an applied stretching, $\mathbf{D}^{app}$, scaled as $\lambda\mathbf{D}^{app}$ then the modified stretching used for evaluating stress in grains is $\lambda^{\frac{1}{k+1}}\mathbf{D}^{p}$. The same rate of stretching is applied to every constituent crystal in a Taylor polycrystal at each integration point. Consequently, the grain stresses, $\mathbf{T}$ and $\boldsymbol{\sigma}$ scale accordingly i.e., $\lambda^{\frac{1}{(k+1)n}}\boldsymbol{\sigma}$. The homogenized macroscopic stress is then $\lambda^{\frac{1}{(k+1)n}}\overline{\boldsymbol{\sigma}}$. While a change in k influences the stretching and stress tensors, it does not affect the selection of active slip/twin systems, which is driven only by n. In summary, the k-mod regulates the strain rate sensitivity, m, through a combination of both n and k: m=1/((k+1)n).

Since the k-mod method changes the rate of plastic stretching accommodated by individual grains from $\mathbf{D}^{app}$ to $\mathbf{D}^{p}$, to ensure that every grain accommodates the applied rate of stretching, $\mathbf{D}^{app}$, the calculated shearing rates are adjusted as

$$\mathbf{D}^{p,app} = \frac{\left|\mathbf{D}^{app}\right|}{\left|\mathbf{D}^{app}\right|^{\frac{1}{k+1}}}\sum_{s}\mathbf{P}_{0}^{s}\dot{\gamma}^{s} = \sum_{s}\mathbf{P}_{0}^{s}\dot{\gamma}_{k-\mathrm{mod}}^{s} \text{ with } \mathbf{P}_{0}^{s} = \frac{1}{2}(\mathbf{S}_{0}^{s} + (\mathbf{S}_{0}^{s})^{T}), \tag{10}$$

such that the shearing rates in T-CPFE are

$$\dot{\gamma}^s_{k-\mathrm{mod}} = \frac{\left|\mathbf{D}^{app}\right|}{\left|\mathbf{D}^{app}\right|^{\frac{1}{k+1}}} \dot{\gamma}_0 \left(\frac{\left|\mathbf{T}\cdot\mathbf{P}^s_0\right|}{\tau_c{}^s} \right)^n \mathrm{sgn}\left(\mathbf{T}\cdot\mathbf{P}^s_0\right). \quad (11)$$

3.4.2 Evolving structure SRS: model for slip and twin resistances

The strain rate sensitivity embedded in the exponent n is distinct from the *evolving structure* strain-rate sensitive associated with the evolution of slip resistances, τ_c^s, and underlying dislocation density as described by the thermodynamics of slip (Follansbee and Kocks, 1988; Kocks et al., 1975). Here we describe the hardening law that evolves the slip and twin (Ardeljan et al., 2016). While the evolution laws are a function of temperature and strain rate, we focus the law description on the role of strain-rate. The temperature T in our calculations is fixed at room temperature, 295 K.

The resistance to slip is given by

$$\tau_c^s(\dot{\varepsilon}, T) = \tau_0^\alpha + \tau_{for}^s(\dot{\varepsilon}, T) + \tau_{sub}^\alpha(\dot{\varepsilon}, T), \quad (12)$$

where τ_0^α is the slip resistance per slip mode α that is unrelated to dislocation density evolution.

The τ_{for}^s is the contribution due to storage of the forest dislocation density, and τ_{sub}^α is the contribution due to storage of the substructure dislocation density. These terms are a function of dislocation density populations, $\rho_{for}^s(\dot{\varepsilon}, T)$ and $\rho_{sub}(\dot{\varepsilon}, T)$, as follows (Madec et al., 2002)

$$\tau_{for}^s = b^\alpha \mu^\alpha \sqrt{\chi^{ss'} \rho_{for}^{s'}},\ \tau_{sub}^\alpha = 0.086 \mu^\alpha b^\alpha \sqrt{\rho_{sub}}\, log\left(\frac{1}{b^\alpha \sqrt{\rho_{sub}}}\right), \quad (13)$$

where $\chi^{ss'}$ is a matrix of dislocation interactions with the diagonal terms (s=s') set to 0.81 and the off-diagonal terms to zero (Lavrentev, 1980; Mecking and Kocks, 1981). The forest dislocation population evolves using (Essmann and Mughrabi, 1979; Mecking and Kocks, 1981)

$$\frac{\partial \rho_{for}^{s}}{\partial \gamma^{s'}} = \frac{\partial \rho_{gen,for}^{s}}{\partial \gamma^{s'}} - \frac{\partial \rho_{rem,for}^{s}}{\partial \gamma^{s'}} = k_1^{\alpha}\sqrt{\rho_{for}^{s}} - k_2^{s}(\dot{\varepsilon},T)\rho_{for}^{s}, \quad \Delta\rho_{for}^{s} = \frac{\partial \rho_{for}^{s}}{\partial \gamma^{s'}}\left|\Delta\gamma^{s}\right|, \tag{14}$$

where k_1^{α} is the coefficient for storage rate and $k_2^{\alpha}(\dot{\varepsilon},T)$ is the coefficient on the dynamic recovery rate (Beyerlein and Tomé, 2008). Their ratio is given by

$$\frac{k_1^{\alpha}}{k_2^{s}(\dot{\varepsilon},T)} = \frac{1}{\sqrt{\left(\chi^{s's}\right)^{-1}\left(\frac{\tau_{sat}^{\alpha}}{b^{\alpha}\mu^{\alpha}}\right)^{2}}}, \; \tau_{sat}^{\alpha} = \frac{D^{\alpha}(b^{\alpha})^{3}g^{\alpha}\mu^{\alpha}}{\left(D^{\alpha}(b^{\alpha})^{3} - kTln\left(\frac{\dot{\varepsilon}}{\dot{\varepsilon}_0}\right)\right)}. \tag{15}$$

where k is Boltzmann's constant, $\dot{\varepsilon}_0$ is a reference strain-rate (10^7 s^{-1}), g^{α} is an activation enthalpy, and D^{α} is a drag stress. The substructure dislocation population increments following

$$\Delta\rho_{sub} = \sum_s q^{\alpha} b^{\alpha}\sqrt{\rho_{sub}}\,\frac{\partial \rho_{rem,for}^{s}}{\partial \gamma^{s'}}\left|\Delta\gamma^{s'}\right|, \tag{16}$$

where q^{α} is a coefficient on the rate at which dislocation debris form from the dynamic recovery reactions.

The resistance to twining is given by

$$\tau_c^{t}(\dot{\varepsilon},T) = \tau_0^{\beta} + \tau_{slip}^{\beta}(\dot{\varepsilon},T). \tag{17}$$

The friction term for twin resistance is

$$\tau_0^{\beta} = \tau_{prop}^{\beta} + \left(\tau_{crit}^{\beta} - \tau_{prop}^{\beta}\right)exp\left(-\sum_s \frac{\rho_{for}^{s}}{\rho_{sat}^{s}}\right), \tag{18}$$

with the nucleation stress τ_{crit}^{β} and propagation stress τ_{prop}^{β} (Beyerlein and Tomé, 2008; Savage et al., 2021). The contribution to twin hardening due to slip-twin and twin-twin interactions is given by

$$\tau_{slip}^{\beta} = \mu^{\beta} \sum_s C^{\alpha\beta}(\dot{\varepsilon}) b^{\beta} b^{\alpha} \rho_{for}^{s}. \quad (19)$$

The $C^{\beta\alpha}(\dot{\varepsilon})$ is an interaction matrix sensitive to strain rate. The Burgers vectors values for WE43 are 1.38x10^{-10} m for the two types of extension twins and 9.24x10^{-11} m for the contraction twins. Twin variants form in grains when the twin fraction f^t reach a critical value. This is set to 2% for TTW1 and TTW2 and 1% for CTW and DTW. Twin variants inherit parameters such as dislocation densities and slip/twin resistances from the parent grain upon formation. The number of grains embedded at that FE integration points increases with each new twin variant formed. Growth/thickening of twins is governed by a transfer of volume fraction from the parent grain to the variant according to the amount of shear strain accommodated.

3.5 Initial slip resistance for slip and twinning.

The hardening model for each slip and twin mode α contains an initial slip resistance τ_0^{α}. The initial resistances to slip in WE43 embed the strengthening contributions from lattice resistance, grain boundary barrier effect (i.e. the Hall-Petch-like (HP) effect) and precipitates interactions (Bhattacharyya et al., 2018)

$$\tau_0^{\alpha} = \tau_{0,0}^{\alpha} + \tau_{HP}^{s} + \tau_{ppt}^{\alpha}. \quad (20)$$

τ_{HP}^{s} is the barrier (Hall-Petch (HP)-like) term evolving per slip system *s* due to twin lamellae since the grain size barrier effects is already embedded in $\tau_{0,0}^{\alpha}$. It is given by

$$\tau_{HP}^{s} = \mu^{\alpha} H_i^{\alpha} \sqrt{\frac{b^{\alpha}}{d_{mfp}^{s}}}, \quad (21)$$

where b^{α} is magnitude of the Burgers vector per mode α (3.2094 x 10^{-10} m for basal slip, 3.2094 x 10^{-10} m for prismatic slip, and 6.12 x 10^{-10} m for pyramidal slip), and μ^{α} is the effective isotropic shear modulus (16,500 MPa for WE43 (Watanabe et al., 2004)). The coefficients H_i^{α} per slip mode for systems pertain to grains having lamellae of either TTW1 (i = 1) or TTW2 (i = 2) or CTW (i = 3) or DTW (i = 4). The d_{mfp}^{s} is the mean-free-path for dislocations and is estimated as the distance between adjacent twin lamellae per grain using (Proust et al., 2007)

$$d_{mfp}^{s} = \frac{(1-f^{pts})d_c}{\sin(\theta)}, \quad (22)$$

where f^{pts} is the predominant twinning system (PTS) volume fraction, θ is the angle spanning between the given slip system and twin system planes, and d_c is the spacing estimated as the ratio between the average grain size and number of twin lamellae per grain. While the model allows formation of multiple twin variants per grain, the predominant twin variant is used to estimate d_{mfp}^{s}. For WE43, we use $d_g = 25\ \mu m$ and the three for the observed number of lamellae per grain.

3.6 Contribution of precipitate shearing to slip resistance

The initial resistances to slip in WE43 include a term due to precipitates τ_{ppt}^{α}. Earlier work has reported that β' precipitates are sheared by basal <**a**> dislocations (Bhattacharyya et al., 2018). For the case of particle shearing, APB strengthening is the major contributor to the slip resistance as the shearing interface creation and underlying coherency strains contribute very little (Bhattacharyya et al., 2018). The work presented in (Bhattacharyya et al., 2018) provided an

empirical approach to estimate a contribution of dislocation shearing and underlying APB to the initial slip resistance of basal slip systems:

$$\tau_{sphere} = \frac{\gamma_{APB}}{2b}\left(\frac{2r_p^{sphere}}{\lambda_{basal}^{sphere}} - f^{sphere}\right), \tag{23}$$

$$\tau_{plate} = \frac{\gamma_{APB}}{2b}\left(\frac{2r_p^{plate}}{\lambda_{basal}^{plate}} - f^{plate}\right) \tag{24}$$

where γ_{APB} is the APB energy, r_p^{sphere} is radius of spherical precipitates, while r_p^{plate} is an equivalent radius of plate shaped precipitates. The λ_{basal}^{sphere} and λ_{basal}^{plate} are effective interparticle spacings for sphere-type and plate-type precipitates. Finally, f^{sphere} and f^{plate} are volume factions. Detailed characterization in prior works (Bhattacharyya et al., 2017; Bhattacharyya et al., 2018) established the values as follows: r_p^{sphere} = 9.44e-9 m, r_p^{plate} = 3.3138e-09 m, λ_{basal}^{sphere} = 1.7960e-07 m, λ_{basal}^{plate} = 4.0801e-08 m, f^{sphere} = 0.76% and f^{plate} = 1.92%. The work in (Bhattacharyya et al., 2018) did not perform the calculations of APB.

Unlike the basal <**a**> dislocations, the non-basal <**a**> and <**c**+**a**> dislocations do not shear precipitates but bow around them. This type of strengthening is referred to as Orowan strengthening (Bhattacharyya et al., 2018). Orowan strength predictions are therefore an appropriate treatment for non-basal <**a**> and <**c**+**a**> dislocations. Estimates were provided in (Bhattacharyya et al., 2018) as 60 MPa and 120 MPa for prismatic and pyramidal slip systems, respectively. Considering larger lattice resistance and grain size barrier HP contributions to the resistance of the non-basal <**a**> and <**c**+**a**> glide than for basal (Bhattacharyya et al., 2018), the established initial slip resistances in this work for these slip systems will be discussed as reasonable.

There is no established model for the effect of precipitates, either shearable or non-shearable, on the strength of twinning (Robson et al., 2011). Some atomistic and micromechanical computational studies on Mg and Mg alloys have shown that precipitates can hinder twin boundary migration and redirect their propagation pathways, but nonetheless do not completely suppress twinning (Leu et al., 2022; Xie et al., 2021). Here we focus on the effect of precipitates on slip only.

3.7 DFT calculations of the APB energy in precipitates in WE43-T6

Density functional theory calculations are conducted via VASP to calculate the γ_{APB} of the precipitates (Kresse and Furthmüller, 1996). Based on the projector augmented wave method (Blöchl, 1994; Kresse and Joubert, 1999), a pseudopotential using a plane-wave basis with a cutoff energy of 515.87 eV is adopted. To approximate the exchange-correlation energy functional, the Perdew-Burke-Ernzerhof formulation of the generalized gradient approximation is used (Perdew et al., 1996). The conjugate gradient scheme is employed for the electronic self-consistent loop. Convergence is reached when the total free energy change between two steps is smaller than 10^{-4} eV. The Brillouin zone is constructed by the Monkhorst-Pack scheme (Monkhorst and Pack, 1976), with a smearing width of 0.2 eV based on the Methfessel-Paxton smearing method (Methfessel and Paxton, 1989). The numbers of valence electrons per atom are 10, 11, and 11 for Mg, Nd, and Y, respectively.

Transmission electron microscopy experiments confirmed that the β' precipitate in WE43 has a based centered orthorhombic (BCO) structure (Bhattacharyya et al., 2018). In a pure metal, each BCO primitive unit cell contains two atoms. In the alloy, however, the chemical composition of

the β’ precipitate is $Mg_{12}NdY$, which indicates that a primitive unit cell should contain at least 14 atoms, of which 12 are Mg, one is Nd, and one is Y.

Given the composition $Mg_{12}NdY$, the atomic configuration must be further specified for subsequent calculations of the APB energy. The type of element that occupies each atomic site is not known from experiments. Hence, when constructing the simulation cells, we consider all 26 (= 13×14 / 7) possible atomic configurations (Su et al., 2019a). As shown in Figure 3, each cell contains seven base planes, each of which contains two atoms. The three lattice parameters a_0, b_0, and c_0 in each cell are calculated via the approach from (Su et al., 2020). We observe that any of these lattice parameters could vary by a factor of 2 among the 26 configurations. In one particular configuration, all three lattice parameters agreed well with the experimental values reported in (Bhattacharyya et al., 2018). We selected this atomic configuration, shown in Fig. 3, for subsequent calculations of the APB energy.

Basal dislocations shear the base plane in the β’ precipitate (Bhattacharyya et al., 2018). In a unit cell of 14 atoms, there are up to seven unique base planes, and for each plane, there are two unique shearing directions, giving rise to 14 possible APB energies. Each APB energy is calculated as follows. First, one part of the simulation cell is shifted along the Burgers vector direction by b with respect to the remaining part of the cell. We let b be the magnitude of the Burgers vector of the dislocation. Second, the top and bottom atomic layers are fixed while the remaining atomic layers are allowed to relax along the slip plane normal. The ionic relaxation stops when the difference in the total energy between two steps is smaller than 10^{-3} eV/atom. The APB energy is calculated as the shift-induced surplus energy divided by the slip plane area, using procedures similar to those for the generalized stacking fault energies in (Su et al., 2019b).

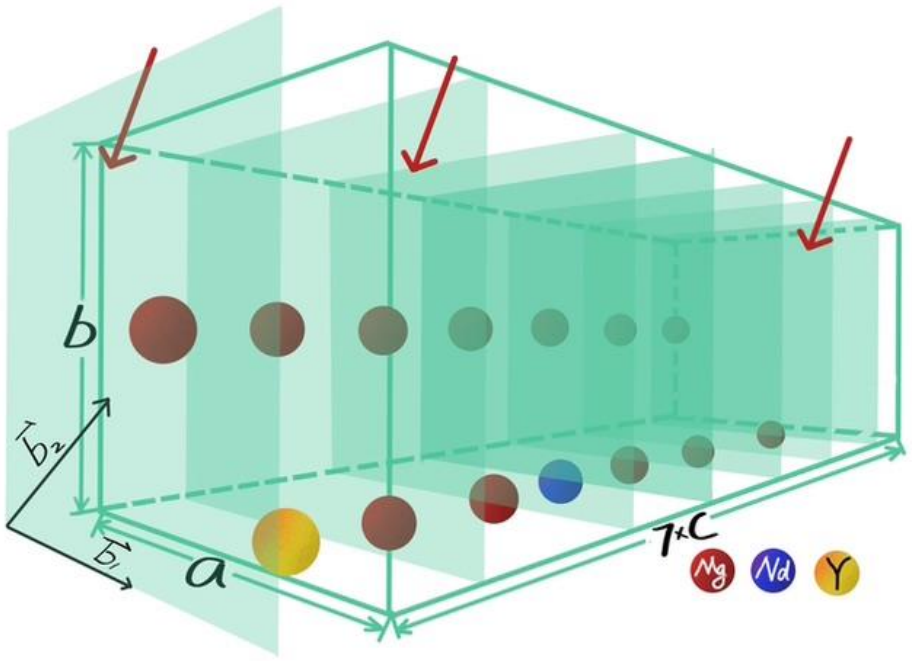

Figure 3. Unit cell of one configuration of the $Mg_{12}NdY$ precipitate. All possible shearing planes are shown. The arrows point to planes which provided positive APB energies.

3.8 Characterizing the slip resistance parameters

The parameters associated with the evolution of the slip resistance are calibrated by fitting the simulated stress-strain response to the measured one. Our aim is to find a set of parameters that fits all tests in all directions and at all strain rates in quasi-static and medium rate SHB tests. Once found, they are used without further adjustment for the even higher rate TC tests to be discussed shortly. Fig. 4 compares the simulated and measured flow stress responses of WE43 along RD, TD, and ND under quasi-static conditions (0.001/s strain rate) and along TD under high strain rates of 1160/s and 2250/s. The simulations were performed using one element model using T-CPFE in Abaqus. The only changes to the FE model for these tests were the prescribed loading direction

and strain rate. With only one set of the right hardening parameters for each slip and twinning system, the model successfully simulates both the effects of loading direction and strain rate on the flow stress response of WE43. The implications of these parameters will be discussed shortly in the results section.

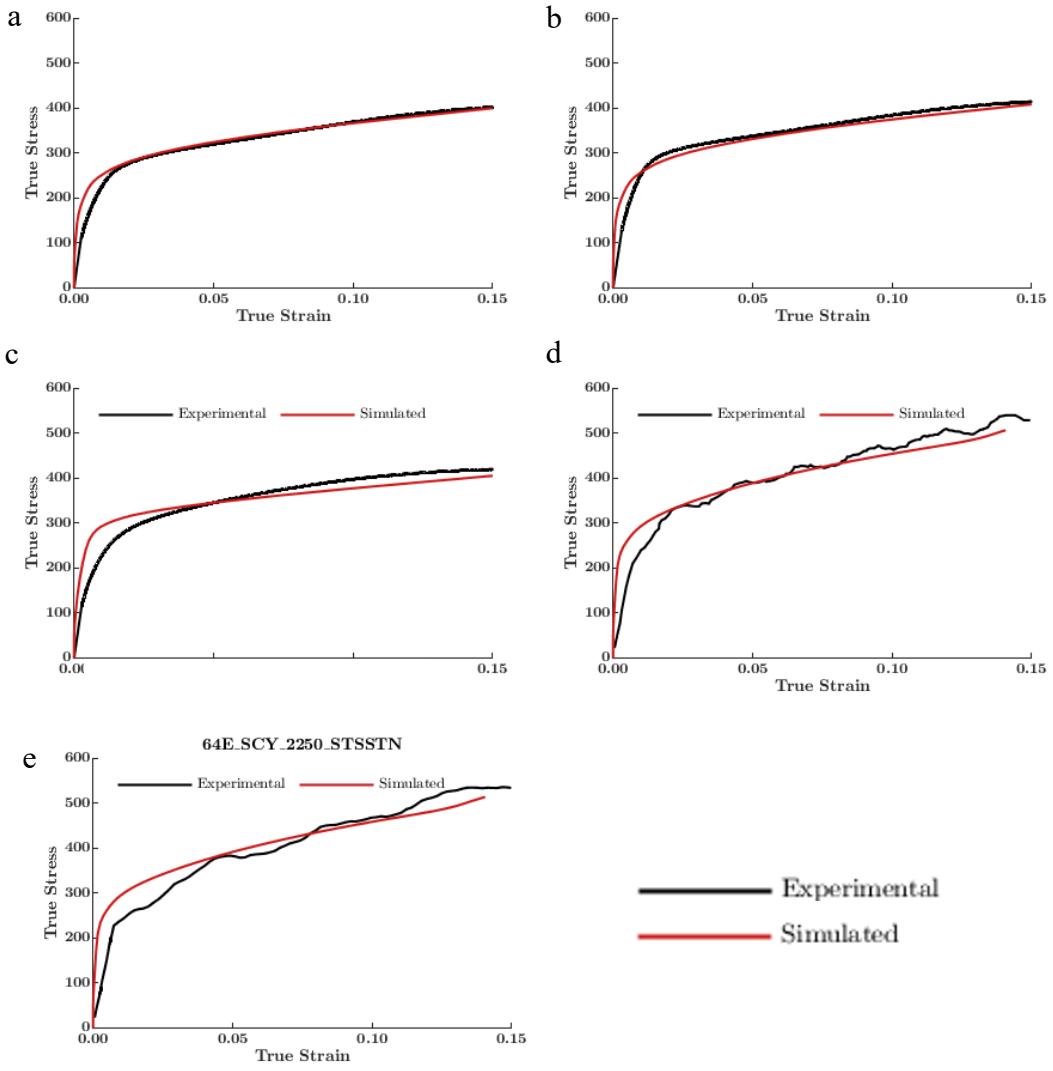

Fig. 4. Experimentally measured and simulated true stress-true strain curves recorded under quasi-static compression ($\dot{\varepsilon}$ = 10^{-3}/s) along (a) RD, (b) TD, and (c) ND and in split Hokinson bar

compression along TD under the average strain rates of (d) 1160/s and (e) 2250/s. The experimental data are taken from (Ghorbanpour et al., 2019; Savage et al., 2020).

3.9 Taylor cylinder impact test model setup

Finally, the constitutive model described in the prior sections is applied for each integration point in the T-CPFE model of a TC sample. For the FE analysis, Abaqus Standard dynamic is used, and Figure 5 shows the FE mesh of the rigid, frictionless surface, and the Taylor cylinder. To reduce computation time, we make use of the symmetry of the cylinder and model only a quarter of the cylinder. The mesh consists of 873 linear hexahedral (C3D8) elements and the appropriateness of this mesh density has been demonstrated earlier in [39]. The cylinder is pushed into the rigid surface at a given velocity in the direction shown [38]. In the calculations that follow the applied velocity per cylinder is the same as in the experimental tests (Table 1).

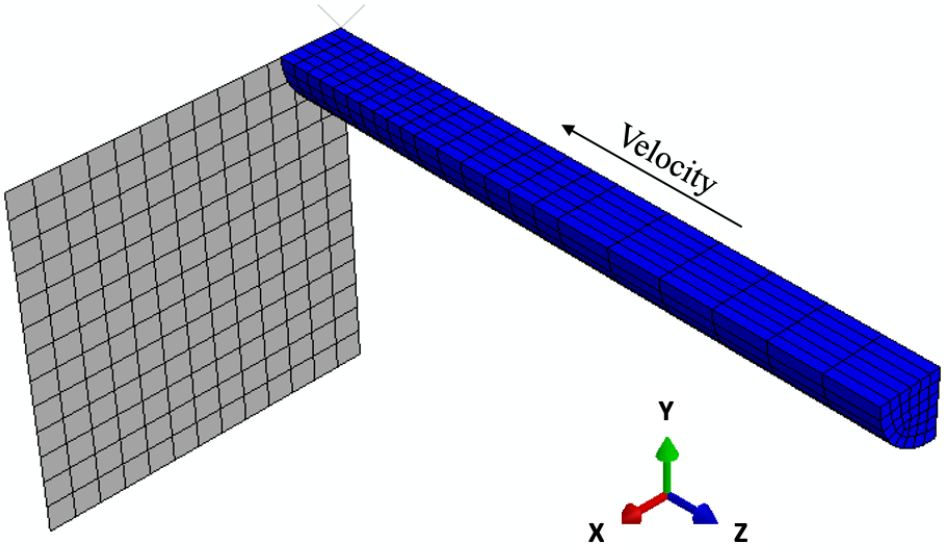

Fig. 5. Simulation setup for the Taylor impact simulations consisting of a cylinder and an analytical rigid surface representing the wall. The quarter model mesh of the cylinder consists of 873 C3D8 elements.

4. Results

4.1 Rate sensitivities.

Table 2 and Table 3 present respectively the strain rate exponents per slip and twin modes identified from the calibration. They suggest that prismatic slip has the greatest strain rate sensitivity, while that for basal slip is virtually negligible. Compared to prismatic and pyramidal slip, twinning has negligible rate sensitivity like basal slip. These values will be used in the TC simulations to follow.

Table 2. Values of n^{α} and k^{α} that achieve agreement with the measured mechanical tests for SRS per slip mode in (Korla and Chokshi, 2010; Ulacia et al., 2010; Watanabe and Ishikawa, 2009).

Parameter	Basal, $\alpha = 1$	Prismatic, $\alpha = 2$	Pyramidal I and II, $\alpha = 3{,}4$
n^{α}	20	20	20
k^{α}	49999	1.28	5.74
$n^{\alpha}\,(k^{\alpha}+1)$	1000000	42.6	134.8
m^{α}	0.000001	0.0235	0.00742

Table 3. Values of n^{α} and k^{α} that achieve agreement with the measured mechanical tests for SRS per twin mode in (Korla and Chokshi, 2010; Watanabe and Ishikawa, 2009).

Parameter	Extension, $\beta = 1$	Contraction, $\beta = 2$
n^{β}	20	20
k^{β}	49999	49999
$n^{\beta}\ (k^{\beta} + 1)$	1000000	1000000
m^{β}	0.000001	0.000001

4.2 Hardening parameters.

A single set of hardening parameters is established for WE43 from the calibration against the material response at low and medium rates Fig. 4. These are given in Table 4 for slip modes and Table 5 for twin modes. These hardening parameters are refined relative to those from our earlier work (Feather et al., 2019) for two reasons. First, the present model incorporates two sources of strain-rate sensitivities, both constant and evolving structure sensitivities, and these two effects are found to vary among the slip and twin modes. Second, the present model considers the individual effect of precipitates on the different slip modes. From the data in Tables 3 and 4, the ratio of the initial resistances at room temperature for the basal, prismatic, pyramidal I and II slip modes and TTW1, TTW2, and CTW twinning modes are 1 : 2.05 : 4.85 : 5.44 : 3.09 : 4.20 : 6.32 (Tables 3 and 4). Basal slip is the easiest and then prismatic slip. The two pyramidal slip modes are the harder slip modes and also harder than the two extension twin modes. The preference for type I

vs. type II pryamidal slip has been debated (Xie et al., 2016; Zecevic et al., 2018), but recent Mg alloy experiments have observed a greater propensity for type I in Mg alloys with rare earths (Yaddanapudi et al., 2021). The results here suggest that type II pryamidal slip would be the harder one than type I pyramidal slip. These ratios for slip are smaller than those for AZ31, which is consistent with the fact that WE43 is known to be less plastically anisotropic than AZ31. We also predict that twinning is generally harder to activate in WE43 than in AZ31, which again is consistent with the observation that the propensity for twinning is lower in WE43 than AZ31.

Table 4. Fitted hardening law parameters for the evolution of slip resistances.

α – slip mode	Basal slip $\{0001\}\langle\bar{1}\bar{1}20\rangle$	Prismatic slip $\{\bar{1}100\}\langle\bar{1}\bar{1}20\rangle$	Pyramidal slip $\{10\bar{1}1\}\langle11\bar{2}\bar{3}\rangle$	Pyramidal slip $\{\bar{1}\bar{1}22\}\langle11\bar{2}3\rangle$
τ_0^α [MPa]	32	70	165	185
k_1^α [m^{-1}]	7.4E7	2.75E8	1.0E8	
g^α	0.004	0.003	0.004	
D^α [MPa]	245	250	285	
q^α	352	260	280	
H_1^α	0.03	0.08	0.08	
H_2^α	0.03	0.08	0.08	
H_3^α	0.8	0.9	1	
H_4^α	0.8	0.9	1	

Table 5. Fitted hardening law parameters for the evolution of twin resistances.

β – twin mode	Extension twin I $\{10\bar{1}2\}\langle 10\bar{1}\bar{1}\rangle$	Extension twin II $\{11\bar{2}1\}\langle 11\bar{2}\bar{6}\rangle$	Contraction twin $\{10\bar{1}1\}\langle 10\bar{1}\bar{2}\rangle$
τ_{crit}^{β} [MPa]	105	143	215
τ_{prop}^{β} [MPa]	90	131	190
$C^{\alpha\beta}, \alpha = 1$	$2.8E4 - 342 \ln(\dot{\varepsilon})$	$1.9E4 - 68 \ln(\dot{\varepsilon})$	$6.5E3 - 68 \ln(\dot{\varepsilon})$
$C^{\alpha\beta}, \alpha = 2$	$2.8E4 - 2.4E3 \ln(\dot{\varepsilon})$	$1.9E4 - 68 \ln(\dot{\varepsilon})$	$5.7E3 - 615 \ln(\dot{\varepsilon})$
$C^{\alpha\beta}, \alpha = 3$	$3.4E4 - 5.4E3 \ln(\dot{\varepsilon})$	$2.6E4 - 68 \ln(\dot{\varepsilon})$	$5.3E3 - 683 \ln(\dot{\varepsilon})$
$C^{\alpha\beta}, \alpha = 4$	$3.4E4 - 5.4E3 \ln(\dot{\varepsilon})$	$2.6E4 - 68 \ln(\dot{\varepsilon})$	$5.5E3 - 683 \ln(\dot{\varepsilon})$

The strengthening contribution from β' precipitates, τ_{ppt}^{1}, for the basal slip mode $\alpha = 1$ is estimated from the DFT calculations for the APB energies. Table 1 presents the eight positive values of the APB energies, in units of mJ/m^2. They are found to vary widely and are strongly dependent on the shearing plane the basal dislocation may use to shear the precipitate. The planes with the lower APB are more likely to be sheared by the dislocation.

Table 6. APB energies for the β' precipitate, in units of mJ/m^2, as calculated via DFT. The β' precipitate has a based centered orthorhombic (BCO) structure. Each system represents a unique plane and slip direction in the unit cell.

	System1	System2	System3	System4	System5	System6	System7	System8
γ_{APB} [mJ/m^2] or 10^{-9} [MPa•m]	253.61	295.49	11.35	184.87	187.88	14.20	51.56	54.73

Table 7 presents the values calculated using Eqs. (23) and (24) for each γ_{APB} from Table 6. Average value after Pythagorean superposition of the eight values is 35.66 MPa. The calibrated value τ_0^α = 32 MPa for basal slip presented in Table 3 agrees very well with this value estimated using APB analysis, especially since precipitates with lower APB are more likely to be shared than those with higher APB. As a result, the average value of 35.66 MPa is an upper bound estimate. While the value τ_0^α includes other contributions, these are expected to be small. The solid solution strengthening for basal slip is small (Yasi et al., 2010) and the Hall-Petch coefficients provided in (Raeisinia et al., 2011) for grain size barrier strengthening in WE43 contributes < 1 MPa. Moreover, the lattice resistance can be ignored for basal slip (Bhattacharyya et al., 2018). Initial slip resistances are generally expected to depend on strain rate (Ardeljan et al., 2016; Knezevic et al., 2014a; Knezevic et al., 2013). The work here for WE43 did not find large strain rate dependence.

Table 7. The strengthening contribution from precipitates, τ_{ppt}^1 , for the basal slip mode $\alpha = 1$.

	System1	System2	System3	System4	System5	System6	System7	System8

τ_{sphere} [MPa]	38.65	45.03	1.73	28.17	28.63	2.16	7.86	8.34
τ_{plate} [MPa]	56.76	66.13	2.54	41.37	42.05	3.18	11.54	12.25
Pythagorean superposition for τ_{ppt}^{1} [MPa]	68.67	80.01	3.07	50.05	50.87	3.84	13.96	14.82

4.3 Slip and twinning activities during monotonic testing

The calculated slip and twin activities are presented in Fig. 6 for the quasi-static (0.001/s strain rate) tests in all three directions and the TD tests from the SHB. In all cases, the deformation is accommodated by slip with some amount of twinning, predominantly the $\{10\bar{1}2\}\langle 10\bar{1}\bar{1}\rangle$ extension twinning. Given the initial texture of the alloy, the in-plane TD, 45TD, and RD deformations are dominated by basal and prismatic slip, with the more active slip mode being basal slip. The activity of pyramidal slip increases with straining due to the development of $\{10\bar{1}2\}\langle 10\bar{1}\bar{1}\rangle$ twinned domains. While minor in content, the CTW and DTW twins activate in the high strain rate tests and at higher strain levels.

In the higher rate SHB tests, we observe that hardening is greater. Texture and texture evolution are known to lead to geometric hardening. However, this geometric hardening contribution would be present in both low- and high-rate tests and thus does not entirely explain the hardening behavior under high strain rates. In this model, the strain rate sensitive response of WE43 is captured as a combination of the power-law exponent and the strain rate sensitive hardening. These hardening

contributions increase with strain rate. Grains containing twins contribute to hardening through the Hall-Petch-like effect. The HP constants associated with the CTW and DTW twins are higher than those for the TTW twins. The contraction and double twins cause high barrier effects and hardening since these twins effectively cut the mean free path of mobile dislocations (Ardeljan et al., 2016; Knezevic et al., 2010), while the extension twins are known to cause a very small barrier effect because these twins grow quickly encompassing grains and transmit dislocations (Molodov et al., 2017). Last, the calculated activities indicate that the greater activity of extension $\{10\bar{1}2\}\langle 10\overline{11}\rangle$ twinning (TTW1) under high strain rate deformation causes more hardening in high-rate conditions than in quasi-static conditions. TTW1 plays a major role in the texture evolution. The effect is larger in the TD than in the RD samples given the initial texture in the alloy. More grains with their **c**-axis perpendicular to the loading direction exist in the TD than in the RD samples. Also, the pyramidal slip activated within the extension twin domains leads to hardening and this mechanism is greater under higher strain rates since more twins are present.

The calculated volume fraction of the $\{10\bar{1}2\}\langle 10\overline{11}\rangle$ deformation twins is shown in Fig. 7. In all tests, the volume fraction grows over the period of straining. For some tests, electron backscattered diffraction (EBSD) measurements of twin fractions were obtained and these datapoints (black symbols) are compared with the calculations. The excellent agreement is a testament to the predictability of the model to not only predict twin evolution via the inherent coupling between slip and twinning, but also to predict the strain rate sensitivity in slip and effect of precipitate hardening on slip resistances.

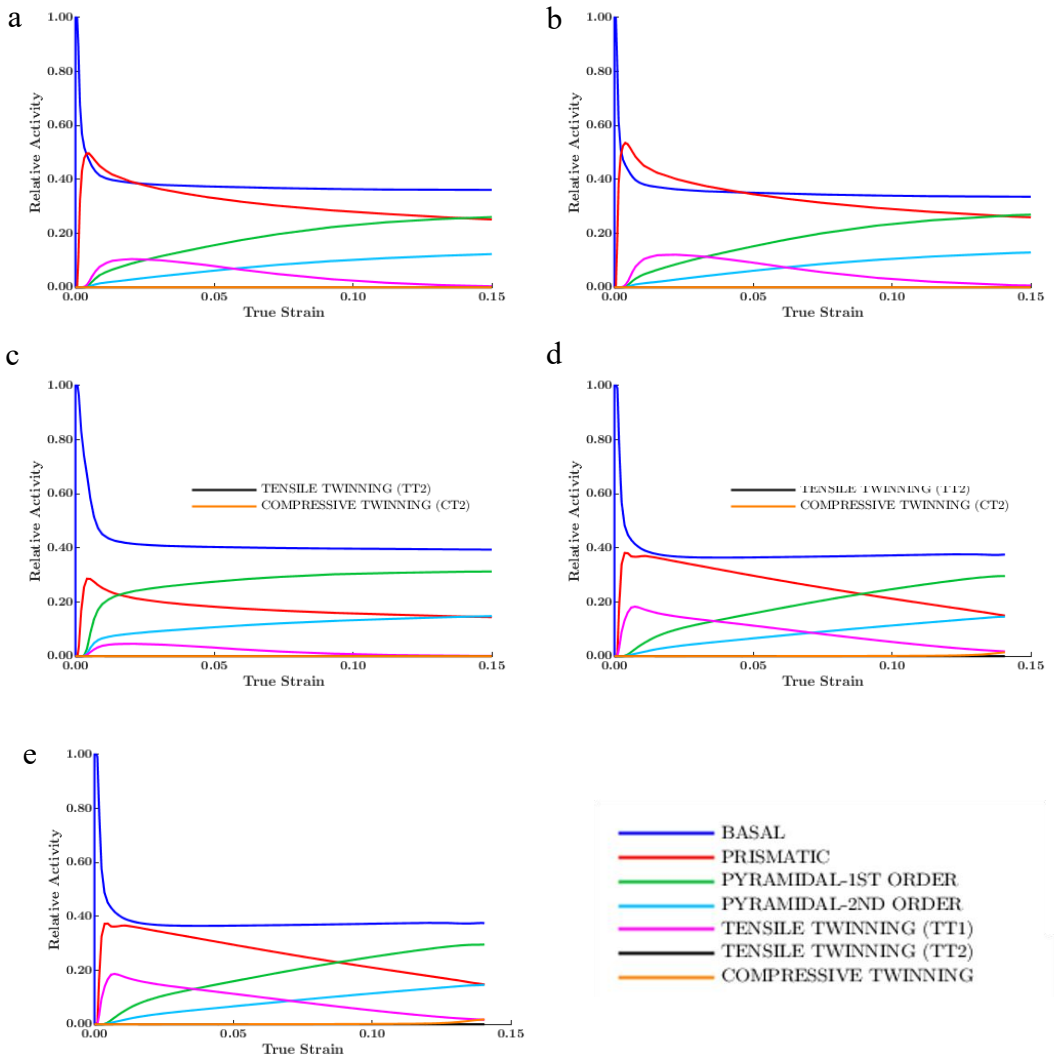

Fig. 6. Relative activities calculated by the model for each deformation mode accommodating the plasticity of the alloy under quasi-static compression ($\varepsilon = 10^{-3}$/s) along (a) RD, (b) TD, and (c) ND and in split Hokinson bar compression along TD under the average strain rates of (d) 1160/s and (e) 2250/s. The activities are averaged over both the parent grains and the twinned domains.

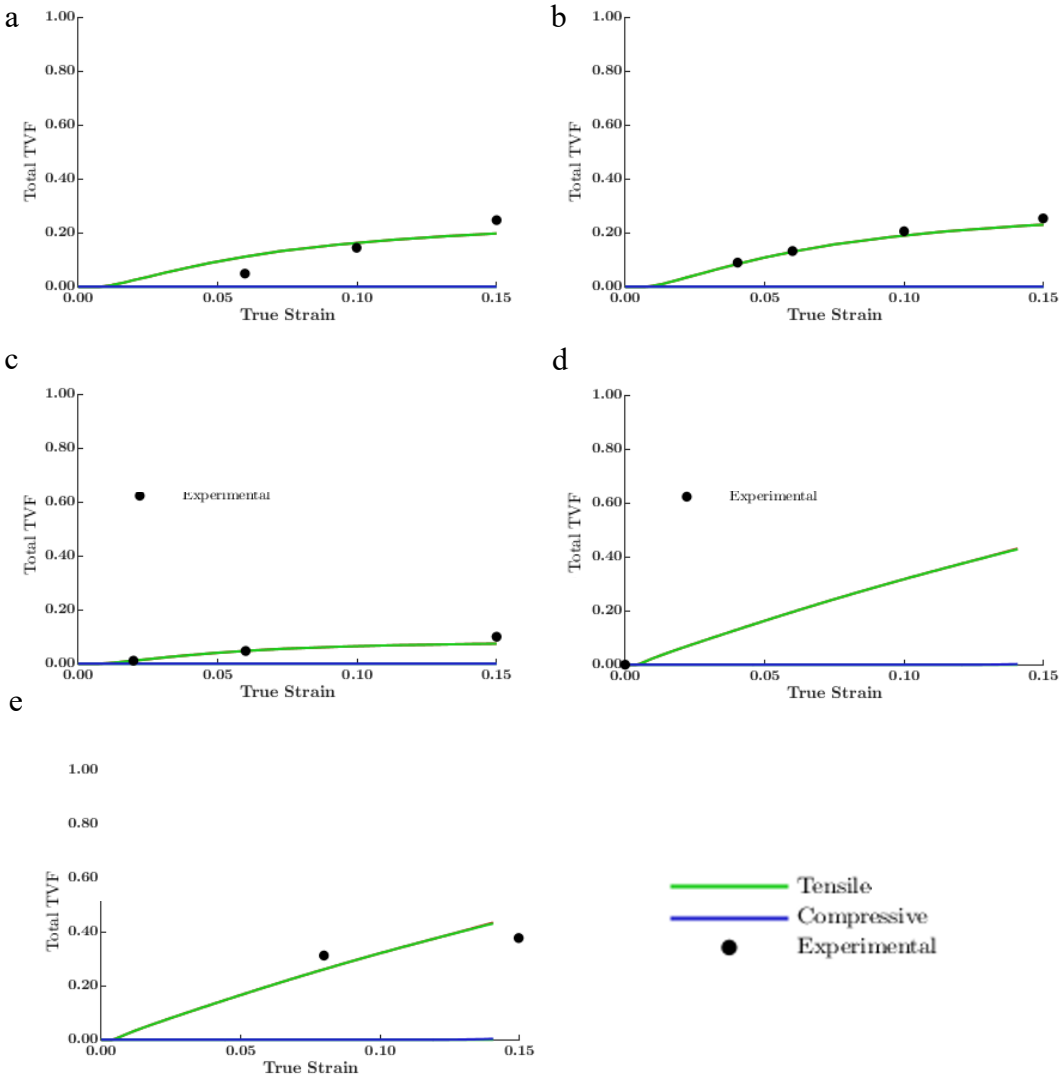

Fig. 7. Comparison of measured and calculated twin volume fractions (TVF) under quasi-static compression ($\varepsilon = 10^{-3}$/s) along (a) RD, (b) TD, and (c) ND and in split Hokinson bar compression along TD under the average strain rates of (d) 1160/s and (e) 2250/s.

4.4 Predicting microstructure evolution at even higher rates of strain

The model calibrated at low and medium strain rates are then used to predict the deformation response and underlying mechanisms during the TC. Fig. 8 shows the evolution of strain rate for the RD cylinder. Contours are similar for the remaining three cylinders and are not shown. Notably the peak rates generated in the tests are on the order 10^5/s, two orders of magnitude higher than those achieved in the SHB tests. The peak strain rate reaches about ~180,000/s. It is found that the region 13 - 17 mm from the foot experience the greatest strain rates over the time of the test.

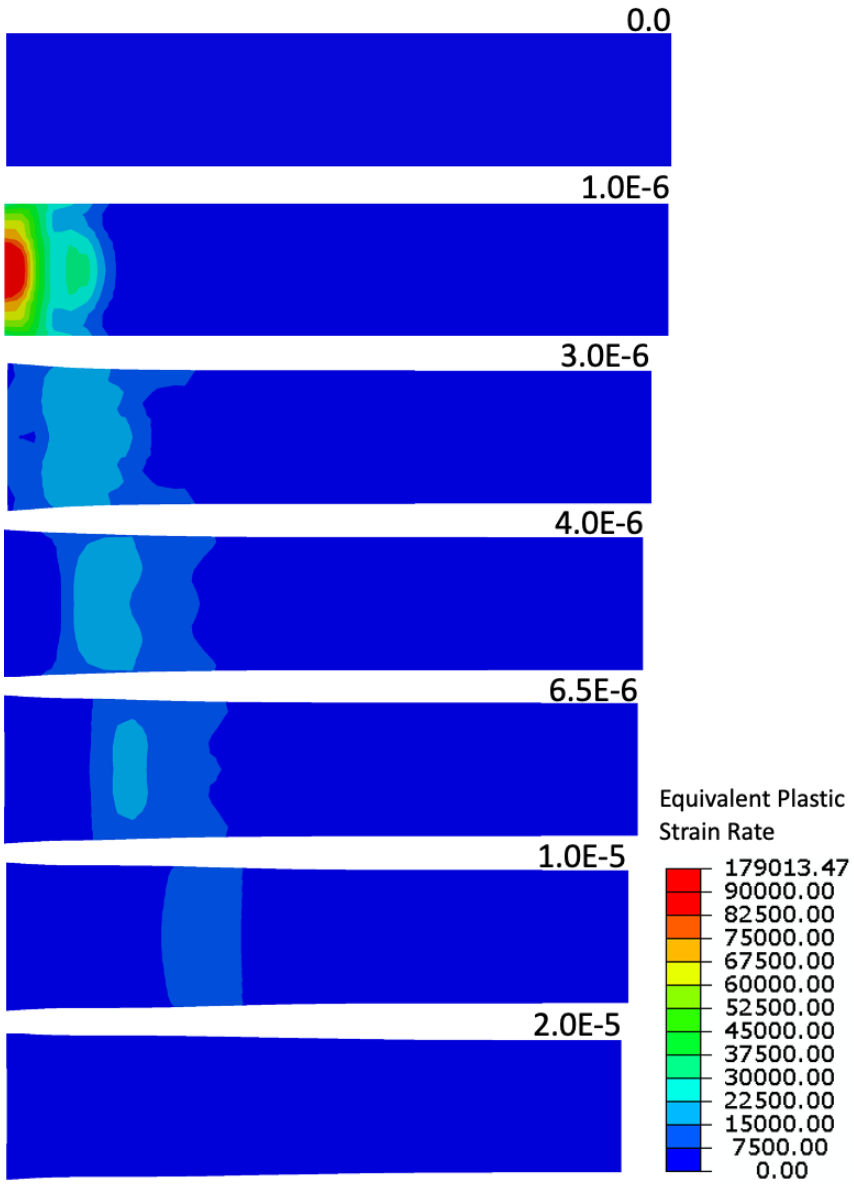

Fig. 8. Contour plots showing the evolution of equivalent plastic strain-rate fields over the RD Taylor cylinder at different times during impact.

Figure 9 shows the FE model predictions of plastic equivalent strain (PEEQ) after deformation for all four cylinders. The PEEQ maps among the four samples are similar, highlighting the near

plastic isotropy of WE43. As expected, the peak strain is achieved at the foot of each TC. The peak strain is about 25% and drops dramatically between 13-17 mm from the foot.

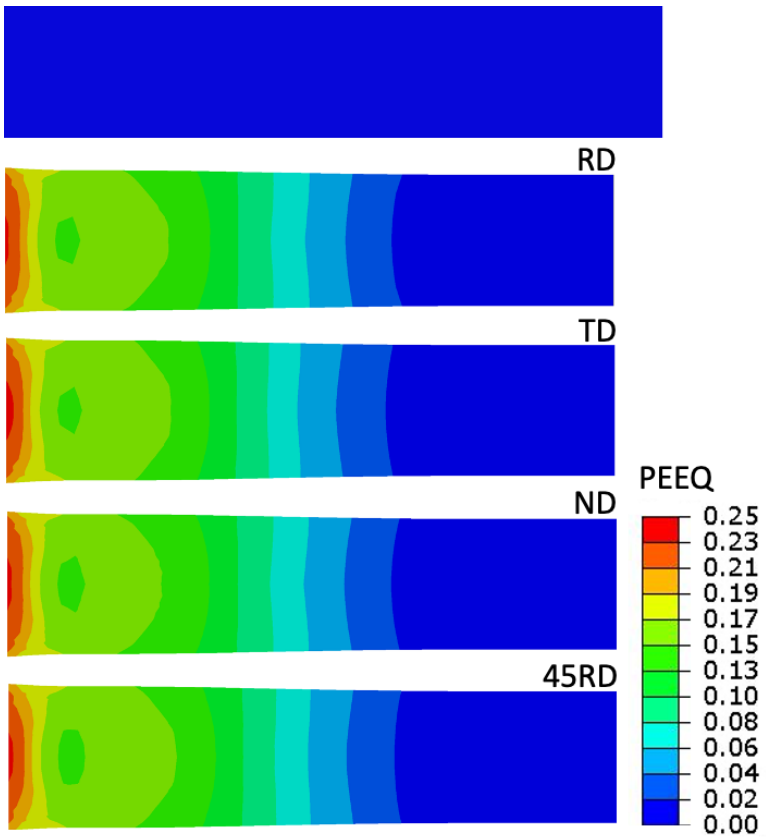

Fig. 9. Contours of equivalent plastic strain (PEEQ) fields over the four cylinders after their impact. An undeformed cylinder is shown on top for reference.

The multi-level model is validated with comparisons to experimental data from (Savage et al., 2020). Towards validating the estimates of strain levels, Figure 10 compares the simulated (left) and measured (right) cross-sectional geometries from the foot to the tail after the impact for all cylinders. Comparison of the radial strain with the experimental major and minor radial strains

reveal a reasonable FE radial strain distribution. This consistency suggests the strain levels are a good estimate. Any small discrepancies in the strain-rate estimate may be due to neglecting thermal anisotropic material behavior.

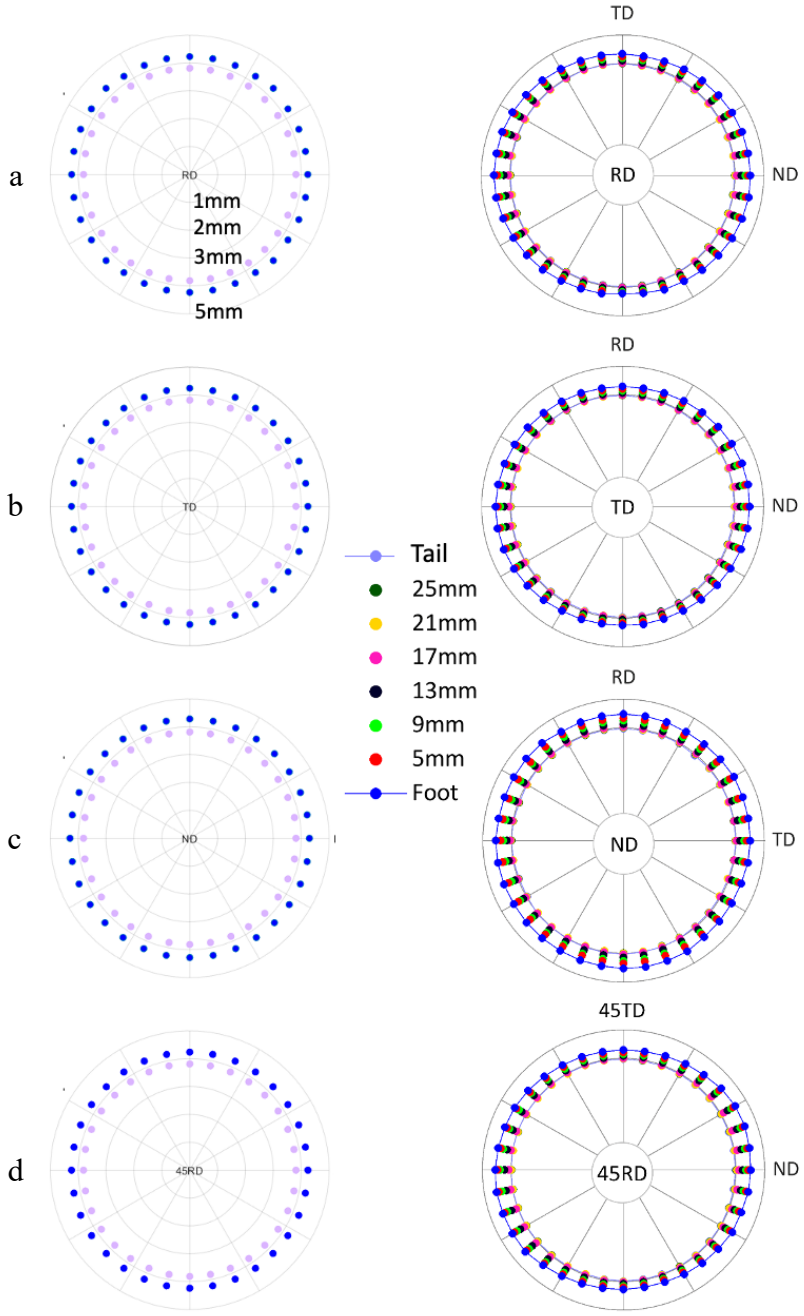

Fig. 10. Comparison of simulated (left) and measured (right) cross-sectional geometries from the foot to the tail after the impact for: (a) RD, (b) TD, (c) ND, and (d) 45RD cylinders. The experimental data are taken from (Savage et al., 2020).

The stringent test of the model is comparison with texture evolution along the TC. Texture evolution in hcp metals like WE43 are highly sensitive to the relative amounts of activity among the slip and twinning modes, which in turn depend on the rate sensitivity. Figures 11 – 14 compare the calculated and measured textures along all four cylinders. In all cases, the model captures the substantial texture evolution along the TC. It predicts the observation that the strong basal texture achieved at the foot is nearly the same in all four tests, regardless of the initial texture. It predicts the abrupt texture change that occurs approximately 17 mm from the foot in the TD, RD, and 45RD. In the ND test, at about 17 mm from the foot the texture strengthens with greater alignment of the basal poles along the ND. This regime is where the higher strain and strain rates were achieved.

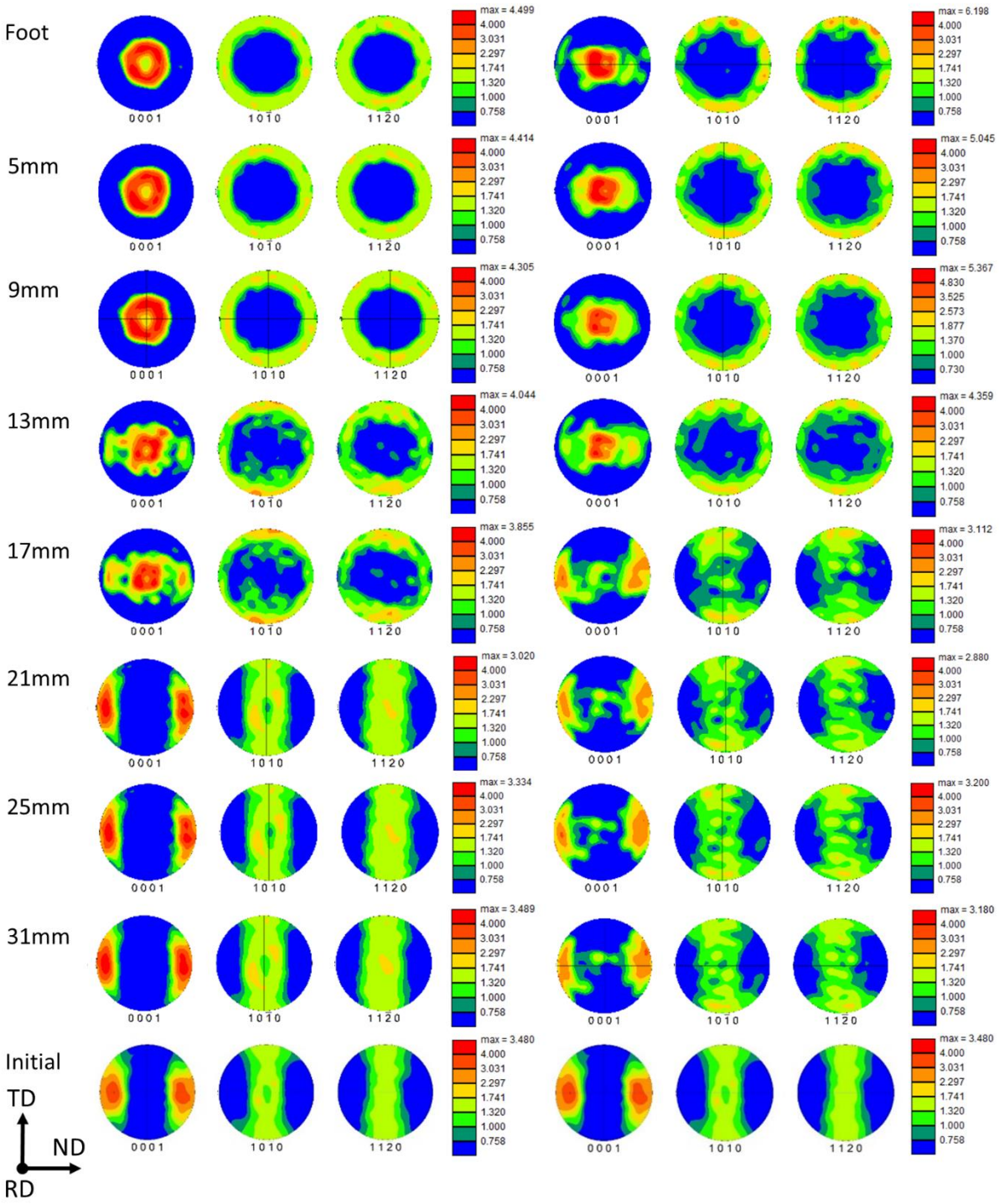

Fig. 11. Pole figures showing the comparison between simulated (left column) and measured by NeD (right column) texture evolution in a WE43 Taylor cylinder after deformation along the RD. The compression axis is at the center of the pole figures. The comparison is shown along the

cylinder at increasing distances from the foot as indicated in the figure. Pole figures of the undeformed state are also shown for reference. The experimental data are taken from (Savage et al., 2020).

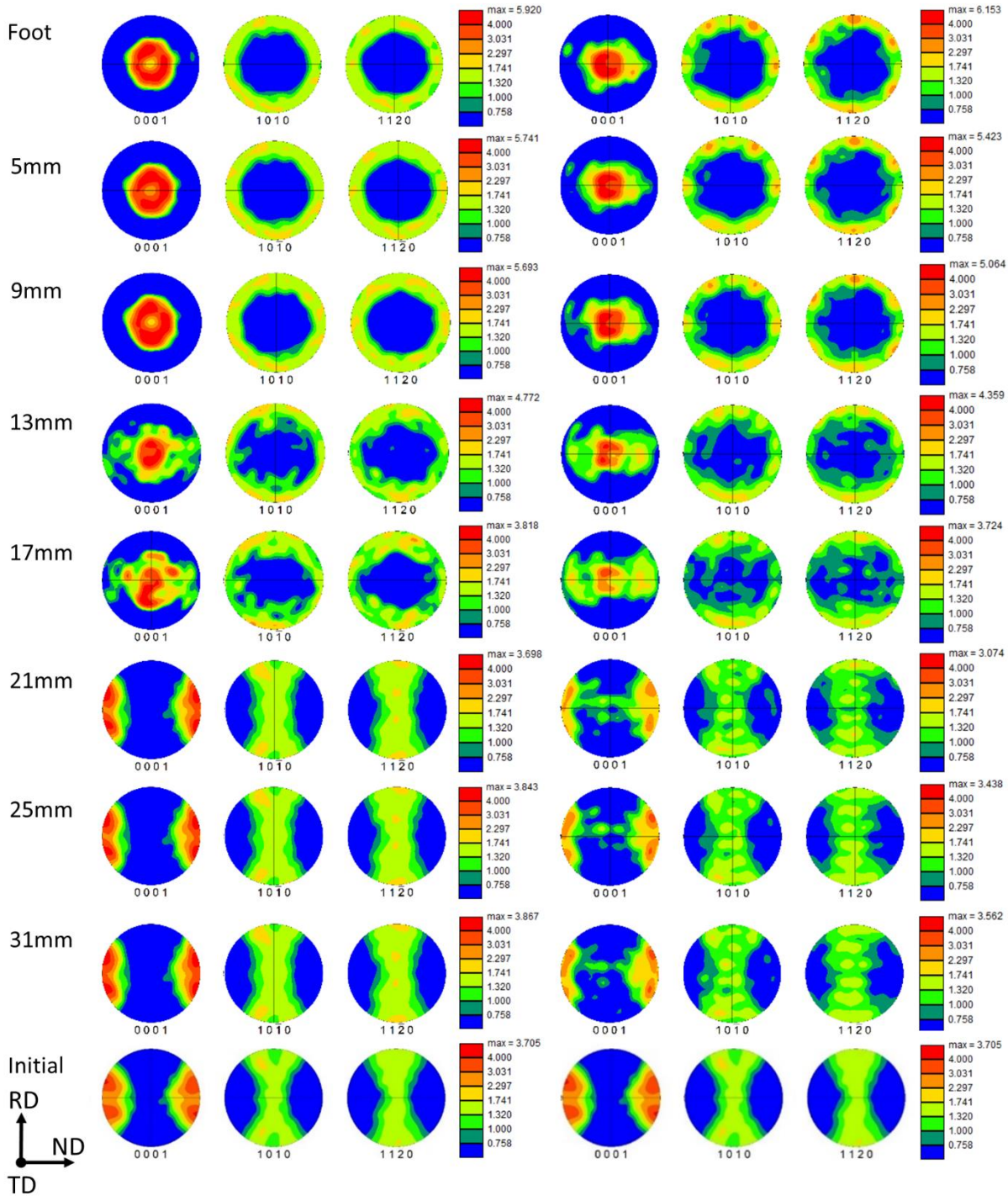

Fig. 12. Pole figures showing the comparison between simulated (left column) and measured by NeD (right column) texture evolution in a WE43 Taylor cylinder after deformation along the TD. The compression axis is at the center of the pole figures. The comparison is shown along the

cylinder at increasing distances from the foot as indicated in the figure. Pole figures of the undeformed state are also shown for reference. The experimental data are taken from (Savage et al., 2020).

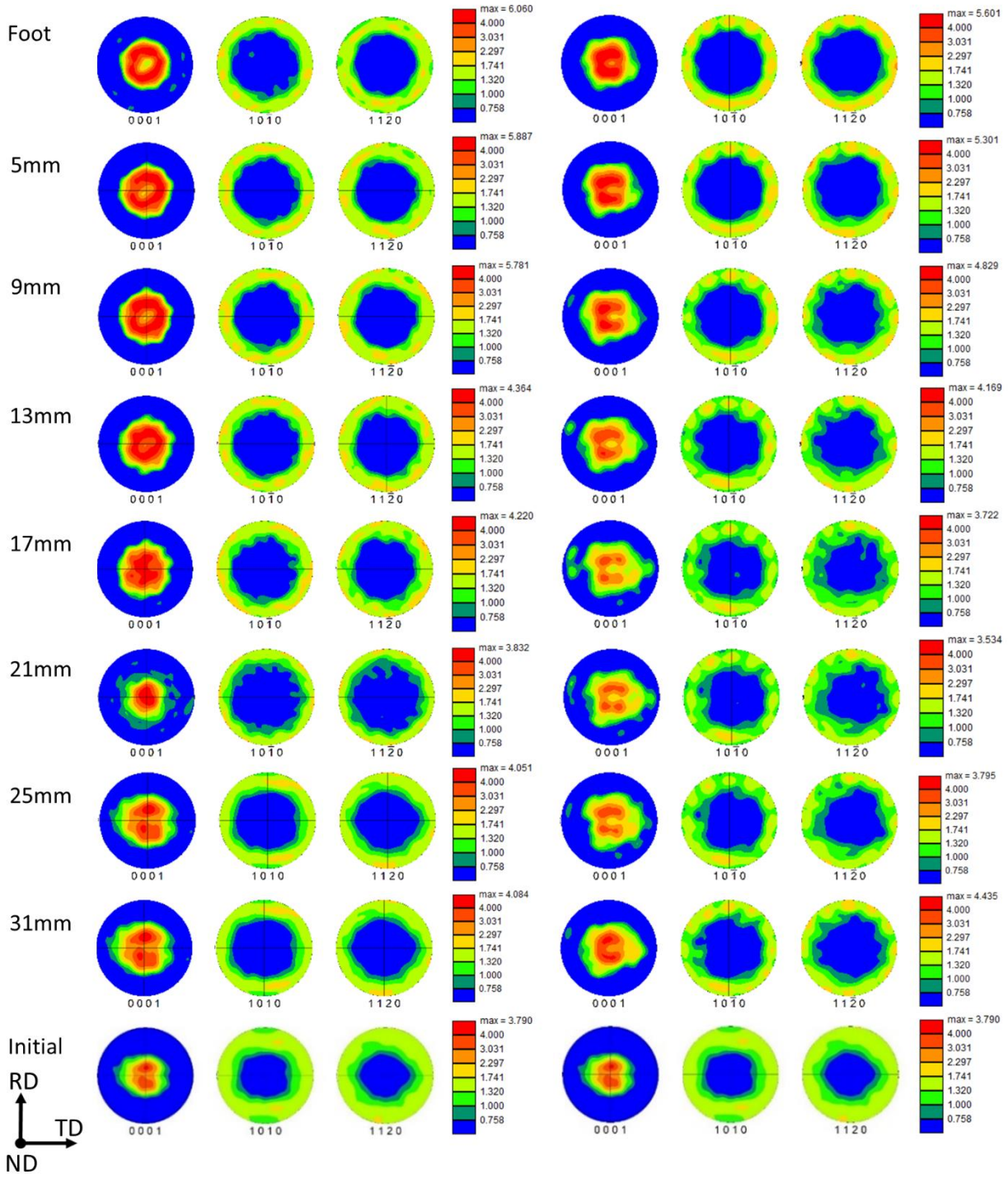

Fig. 13. Pole figures showing the comparison between simulated (left column) and measured by NeD (right column) texture evolution in a WE43 Taylor cylinder after deformation along the ND. The compression axis is at the center of the pole figures. The comparison is shown along the

cylinder at increasing distances from the foot as indicated in the figure. Pole figures of the undeformed state are also shown for reference. The experimental data are taken from (Savage et al., 2020).

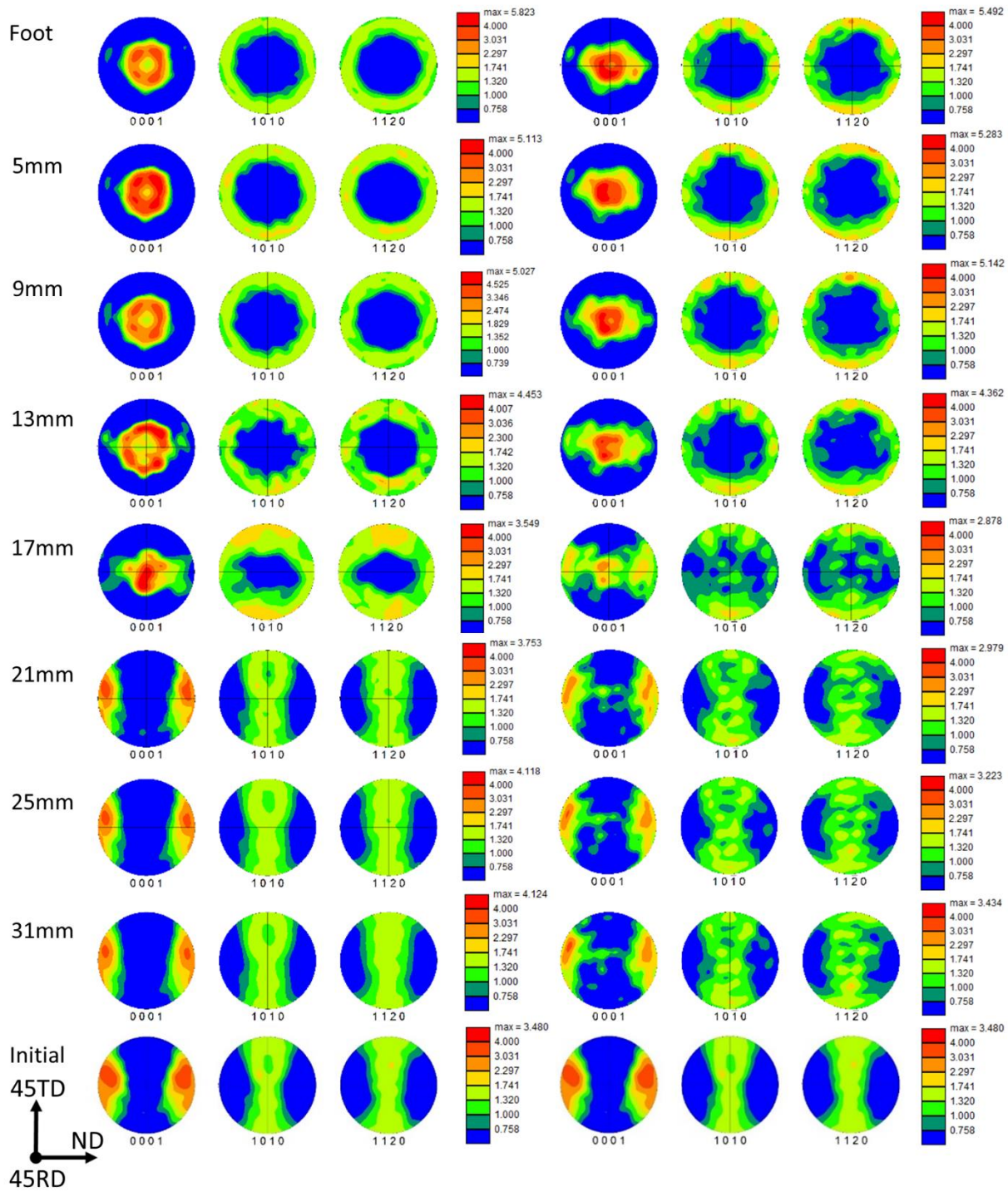

Fig. 14. Pole figures showing the comparison between simulated (left column) and measured by NeD (right column) texture evolution in a WE43 Taylor cylinder after deformation along the 45RD. The compression axis is at the center of the pole figures. The comparison is shown along

the cylinder at increasing distances from the foot as indicated in the figure. Pole figures of the undeformed state are also shown for reference. The experimental data are taken from (Savage et al., 2020).

Finally, as the most challenging test of the model concerns the development of twin domains along the length of the cylinder. Figure 15 compares the measured and predicted twin volume fractions along the cylinders after the impact. The change in the amounts of twinning along the cylinders are captured by the model in all tests. The model predicts the dramatic change in twinning between 13-17 mm from the foot of the cylinder. The model also captures the difference in twinning between the in-plane tests (RD, TD, and 45RD) and the out of plane ND test. It even predicts the order in the amounts of twinning among the in-plane tests, with the most in the TD, then 45RD and last RD.

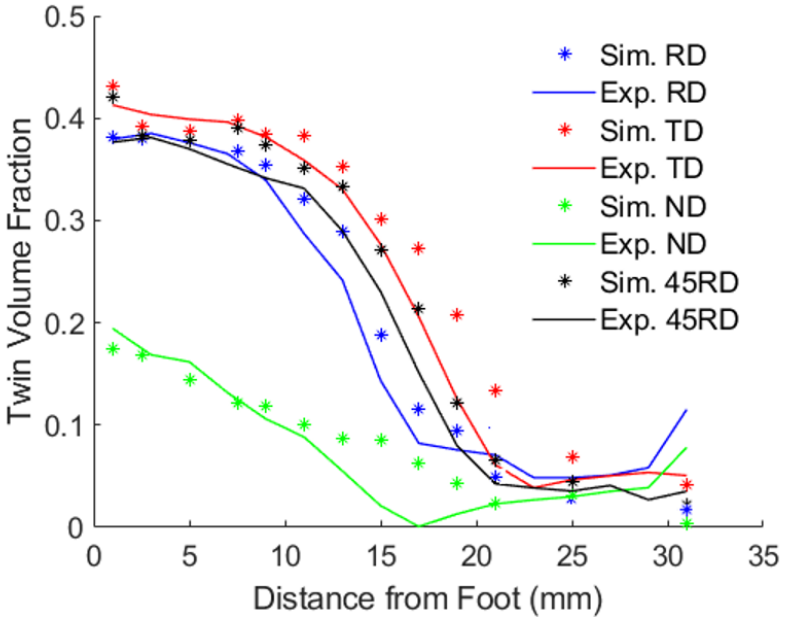

Fig. 15. Comparison of measured and predicted twin volume fractions along the cylinders after the impact. The experimental data are taken from (Savage et al., 2020).

5. Discussion

It should be emphasized that the simultaneous agreement with dimensional changes, texture evolution, and twinning development is achieved over a broad range of strain rates. Another notable feature is the fact that this multi-level model was calibrated using data from much simpler uniaxial tests carried out a lower strain rates than the TC test. The ability of the model to extrapolate to much higher strain rates is attributed to modeling the individual strain rate sensitive behavior for every slip and twinning system. The model further accounts for two types of sources for strain rate behavior. This work is the first time the strain rate sensitivity per slip/twin system is used in a CPFE formulation for modeling of a geometry.

The agreement is also achieved by accounting for the effect of precipitate shearing only in the basal slip mode and not the other slip modes or twinning modes. Despite this, the texture and twinning fraction were predicted remarkably well. This consistency would suggest that indeed precipitate shearing is mainly accomplished by basal dislocations. Given that basal slip is the easiest mode, we find that precipitates strengthen WE43 by substantially strengthening its most predominant and usually weakest slip family. As a result, resistances to slip over slip modes are not disparate in WE43, unlike in other Mg alloys like AZ31.

Although we focus the work on WE43, this is a model material system that can represent any material, particularly one that deforms by multiple slip and twinning modes. Thus, the model is sufficiently general that it can be applied to other hcp metals, such as Be, Ti, and Zr, and orthorhombic materials, such as uranium, that are known to deform by multiple systems. For many

of these materials, the application on the one hand may call for characterization at very high rates, while on the other hand most experimental data are available for uniaxial tests at quasi-static conditions. Characterization of the hardening parameters against experimental tests will likely continue to be an unavoidable step in any crystal plasticity model development for some time to come. The power of the present model lies in its first-time account for two types of strain rate sensitivity and the consequential ability to extrapolate to higher rates of strain.

6. Conclusions

In this work, a multi-level CPFE model is presented for modeling the constitutive response of WE43 under a wide range of strain rates. Two new modeling aspects are implemented. The first is two sources of strain rate sensitivity, one that occurs under constant structure and another that affects the evolving structure. The second is the individual effects of precipitates on slip modes, with shearing for basal slip and Orowan bowing for prismatic and pyramidal slip. The model parameters are found by achieving agreement in the stress-strain response under quasi-static and SHB tests. The effect of precipitates found by this process agrees with independent estimates of slip resistance using DFT calculations of APB energies. It is confirmed that the SRS sensitivity of basal slip and twinning are nearly negligible while that for prismatic slip is the greatest. The model predicts that the strain rates achieved in the Taylor cylinder tests are spread over six orders of magnitude. The peak strain rates are at least two orders of magnitude higher than those in the SHB tests. Based on calibration in the quasi-static and SHB tests, the model is shown to achieve excellent agreement in dimensional shape change, texture evolution, and twinning evolution for Taylor cylinder tests. The ability to extrapolate to higher strain rates than those used in calibration

is attributed to considering the physical sources of SRSs of each slip and twinning mode including the inherent constant structure SRS and the dislocation-based hardening SRS.

Acknowledgements

This research was sponsored by the DEVCOM Army Research Laboratory and was accomplished under cooperative agreement no. W911NF-21-2-0149. I.J.B. is grateful for support by the National Science Foundation under Grant Number 2051390. Use was made of computational facilities purchased with funds from the National Science Foundation (CNS1725797) and administered by the Center for Scientific Computing (CSC). The CSC is supported by the CNSI and the Materials Research Science and Engineering Center (MRSEC; NSF DMR 1720256) at UC Santa Barbara.

References

Agnew, S., Whittington, W., Oppedal, A., El Kadiri, H., Shaeffer, M., Ramesh, K., Bhattacharyya, J., Delorme, R., Davis, B., 2014. Dynamic behavior of a rare-earth-containing Mg alloy, WE43B-T5, plate with comparison to conventional alloy, AM30-F. Jom 66, 277-290.

Ardeljan, M., Beyerlein, I.J., McWilliams, B.A., Knezevic, M., 2016. Strain rate and temperature sensitive multi-level crystal plasticity model for large plastic deformation behavior: Application to AZ31 magnesium alloy. Int. J. Plast. 83, 90-109.

Asaro, R.J., Needleman, A., 1985. Texture development and strain hardening in rate dependent polycrystals. Acta Metall. Mater. 33, 923-953.

Beyerlein, I.J., Tomé, C.N., 2008. A dislocation-based constitutive law for pure Zr including temperature effects. Int. J. Plast. 24, 867-895.

Bhattacharyya, J.J., Wang, F., McQuade, P.J., Agnew, S.R., 2017. Deformation and fracture behavior of Mg alloy, WE43, after various aging heat treatments. Mater. Sci. Eng. A 705, 79-88.

Bhattacharyya, J.J., Wang, F., Stanford, N., Agnew, S.R., 2018. Slip mode dependency of dislocation shearing and looping of precipitates in Mg alloy WE43. Acta. Mater. 146, 55-62.

Bhattacharyya, J.J., Wang, F., Wu, P.D., Whittington, W.R., El Kadiri, H., Agnew, S.R., 2016. Demonstration of alloying, thermal activation, and latent hardening effects on quasi-static and dynamic polycrystal plasticity of Mg alloy, WE43-T5, plate. Int. J. Plast. 81, 123-151.

Blöchl, P.E., 1994. Projector augmented-wave method. Physical Review B 50, 17953.

Chen, S., Gray, G., 1996. Constitutive behavior of tantalum and tantalum-tungsten alloys. Metall. Mater. Trans. A 27, 2994-3006.

Cho, K., Sano, T., Doherty, K., Yen, C., Gazonas, G., Montgomery, J., Moy, P., Davis, B., DeLorme, R., 2009. Magnesium technology and manufacturing for ultra lightweight armored ground vehicles. DTIC Document.

Duvvuru, H.K., Knezevic, M., Mishra, R.K., Kalidindi, S.R., 2007. Application of microstructure sensitive design to FCC polycrystals. Materials science forum 546, 675-680.

Eghtesad, A., Barrett, T.J., Knezevic, M., 2018. Compact reconstruction of orientation distributions using generalized spherical harmonics to advance large-scale crystal plasticity modeling: Verification using cubic, hexagonal, and orthorhombic polycrystals. Acta. Mater. 155, 418-432.

Eghtesad, A., Germaschewski, K., Lebensohn, R.A., Knezevic, M., 2020. A multi-GPU implementation of a full-field crystal plasticity solver for efficient modeling of high-resolution microstructures. Computer Physics Communications 254, 107231.

Eghtesad, A., Knezevic, M., 2018. A new approach to fluid–structure interaction within graphics hardware accelerated smooth particle hydrodynamics considering heterogeneous particle size distribution. Computational Particle Mechanics 5, 387-409.

Essmann, U., Mughrabi, H., 1979. Annihilation of dislocations during tensile and cyclic deformation and limits of dislocation densities. Philosophical Magazine A 40, 731-756.

Feather, W.G., Ghorbanpour, S., Savage, D.J., Ardeljan, M., Jahedi, M., McWilliams, B.A., Gupta, N., Xiang, C., Vogel, S.C., Knezevic, M., 2019. Mechanical response, twinning, and texture evolution of WE43 magnesium-rare earth alloy as a function of strain rate: Experiments and multi-level crystal plasticity modeling. Int. J. Plast. 120, 180-204.

Feather, W.G., Savage, D.J., Knezevic, M., 2021. A crystal plasticity finite element model embedding strain-rate sensitivities inherent to deformation mechanisms: Application to alloy AZ31. Int. J. Plast. 143, 103031.

Feng, Z., Pokharel, R., Vogel, S.C., Lebensohn, R.A., Pagan, D., Zepeda-Alarcon, E., Clausen, B., Martinez, R., Gray, G.T., Knezevic, M., 2022. Crystal plasticity modeling of strain-induced martensitic transformations to predict strain rate and temperature sensitive behavior of 304 L steels: Applications to tension, compression, torsion, and impact. Int. J. Plast. 156, 103367.

Follansbee, P., Kocks, U., 1988. A constitutive description of the deformation of copper based on the use of the mechanical threshold stress as an internal state variable. Acta Metall. 36, 81-93.

Follansbee, P.S., 1985. High Strain Rate Compression Testing - The Hopkinson Bar. 9th edn. Vol. 8, Am. Soc. Metals, Metals Park, Ohio, pp. 198-203.

Gangireddy, S., Gwalani, B., Liu, K., Faierson, E.J., Mishra, R.S., 2019. Microstructure and mechanical behavior of an additive manufactured (AM) WE43-Mg alloy. Additive Manufacturing 26, 53-64.

Ghorbanpour, S., McWilliams, B.A., Knezevic, M., 2019. Effect of hot working and aging heat treatments on monotonic, cyclic, and fatigue behavior of WE43 magnesium alloy. Mater. Sci. Eng. A 747, 27-41.

Ghorbanpour, S., Zecevic, M., Kumar, A., Jahedi, M., Bicknell, J., Jorgensen, L., Beyerlein, I.J., Knezevic, M., 2017. A crystal plasticity model incorporating the effects of precipitates in superalloys: Application to tensile, compressive, and cyclic deformation of Inconel 718. Int. J. Plast. 99, 162-185.

Hutchinson, J.W., 1976. Bounds and self-consistent estimates for creep of polycrystalline materials. Proceedings of the Royal Society of London. Series A, Mathematical and Physical Sciences 348, 101-126.

Imandoust, A., Barrett, C.D., Al-Samman, T., Inal, K.A., El Kadiri, H., 2017. A review on the effect of rare-earth elements on texture evolution during processing of magnesium alloys. J. Mater. Sci. 52, 1-29.

Jahedi, M., McWilliams, B.A., Kellogg, F.R., Beyerlein, I.J., Knezevic, M., 2018a. Rate and temperature dependent deformation behavior of as-cast WE43 magnesium-rare earth alloy manufactured by direct-chill casting. Mater. Sci. Eng. A 712, 50-64.

Jahedi, M., McWilliams, B.A., Knezevic, M., 2018b. Deformation and fracture mechanisms in WE43 magnesium-rare earth alloy fabricated by direct-chill casting and rolling. Mater. Sci. Eng. A 726, 194-207.

Jiang, H.S., Zheng, M.Y., Qiao, X.G., Wu, K., Peng, Q.Y., Yang, S.H., Yuan, Y.H., Luo, J.H., 2017. Microstructure and mechanical properties of WE43 magnesium alloy fabricated by direct-chill casting. Mater. Sci. Eng. A 684, 158-164.

Kabirian, F., Khan, A.S., Gnäupel-Herlod, T., 2015. Visco-plastic modeling of mechanical responses and texture evolution in extruded AZ31 magnesium alloy for various loading conditions. Int. J. Plast. 68, 1-20.

Kalidindi, S.R., 1998. Incorporation of deformation twinning in crystal plasticity models. J. Mech. Phys. Solids 46, 267-271.

Kalidindi, S.R., Bronkhorst, C.A., Anand, L., 1992. Crystallographic texture evolution in bulk deformation processing of FCC metals. J. Mech. Phys. Solids 40, 537-569.

Kandalam, S., Agrawal, P., Avadhani, G.S., Kumar, S., Suwas, S., 2015. Precipitation response of the magnesium alloy WE43 in strained and unstrained conditions. J. Alloys Compd. 623, 317-323.

Knezevic, M., Al-Harbi, H.F., Kalidindi, S.R., 2009. Crystal plasticity simulations using discrete Fourier transforms. Acta. Mater. 57, 1777-1784.

Knezevic, M., Carpenter, J.S., Lovato, M.L., McCabe, R.J., 2014a. Deformation behavior of the cobalt-based superalloy Haynes 25: Experimental characterization and crystal plasticity modeling. Acta. Mater. 63, 162-168.

Knezevic, M., Crapps, J., Beyerlein, I.J., Coughlin, D.R., Clarke, K.D., McCabe, R.J., 2016a. Anisotropic modeling of structural components using embedded crystal plasticity constructive laws within finite elements. International Journal of Mechanical Sciences 105, 227-238.

Knezevic, M., Drach, B., Ardeljan, M., Beyerlein, I.J., 2014b. Three dimensional predictions of grain scale plasticity and grain boundaries using crystal plasticity finite element models. Computer Methods in Applied Mechanics and Engineering 277, 239-259.

Knezevic, M., Kalidindi, S.R., 2007. Fast computation of first-order elastic-plastic closures for polycrystalline cubic-orthorhombic microstructures. Comput. Mater. Sci. 39, 643-648.

Knezevic, M., Levinson, A., Harris, R., Mishra, R.K., Doherty, R.D., Kalidindi, S.R., 2010. Deformation twinning in AZ31: Influence on strain hardening and texture evolution. Acta. Mater. 58, 6230-6242.

Knezevic, M., McCabe, R.J., Tomé, C.N., Lebensohn, R.A., Chen, S.R., Cady, C.M., Gray Iii, G.T., Mihaila, B., 2013. Modeling mechanical response and texture evolution of α-uranium as a function of strain rate and temperature using polycrystal plasticity. Int. J. Plast. 43, 70-84.

Knezevic, M., Zecevic, M., Beyerlein, I.J., Lebensohn, R.A., 2016b. A numerical procedure enabling accurate descriptions of strain rate-sensitive flow of polycrystals within crystal visco-plasticity theory. Computer Methods in Applied Mechanics and Engineering 308, 468-482.

Kocks, U., Argon, A., Ashby, M., 1975. Thermodynamics and Kinetics of Slip. Prog. Mater. Sci. 19, 110-170.

Korla, R., Chokshi, A.H., 2010. Strain-rate sensitivity and microstructural evolution in a Mg–Al–Zn alloy. Scr. Mater. 63, 913-916.

Kresse, G., Furthmüller, J., 1996. Efficient iterative schemes for ab initio total-energy calculations using a plane-wave basis set. Physical Review B 54, 11169.

Kresse, G., Joubert, D., 1999. From ultrasoft pseudopotentials to the projector augmented-wave method. Physical Review B 59, 1758.

Landry, N., Knezevic, M., 2015. Delineation of First-Order Elastic Property Closures for Hexagonal Metals Using Fast Fourier Transforms. Materials 8, 6326-6345.

Lavrentev, F.F., 1980. The type of dislocation interaction as the factor determining work hardening. Materials Science and Engineering 46, 191-208.

Lebensohn, R.A., Kanjarla, A.K., Eisenlohr, P., 2012. An elasto-viscoplastic formulation based on fast Fourier transforms for the prediction of micromechanical fields in polycrystalline materials. Int. J. Plast. 32-33, 59-69.

Lebensohn, R.A., Tomé, C.N., 1993. A self-consistent anisotropic approach for the simulation of plastic deformation and texture development of polycrystals: Application to zirconium alloys. Acta Metall. Mater. 41, 2611-2624.

Leu, B., Kumar, M.A., Xie, K.Y., Beyerlein, I.J., 2022. Twinning pathways enabled by precipitates in AZ91. Materialia 21, 101292.

Liu, J., Liu, B., Min, S., Yin, B., Peng, B., Yu, Z., Wang, C., Ma, X., Wen, P., Tian, Y., Zheng, Y., 2022. Biodegradable magnesium alloy WE43 porous scaffolds fabricated by laser powder bed fusion for orthopedic applications: Process optimization, in vitro and in vivo investigation. Bioactive Materials 16, 301-319.

Livescu, V., Cady, C.M., Cerreta, E.K., Henrie, B.L., Gray, G.T., 2016. The high strain rate deformation behavior of high purity magnesium and AZ31B magnesium alloy, Essential Readings in Magnesium Technology. Springer, pp. 375-380.

Madec, R., Devincre, B., Kubin, L.P., 2002. From Dislocation Junctions to Forest Hardening. Physical Review Letters 89, 255508.

Martin, L.P., Orlikowski, D., Nguyen, J.H., 2006. Fabrication and characterization of graded impedance impactors for gas gun experiments from tape cast metal powders. Mater. Sci. Eng. A 427, 83-91.

Maudlin, P., Gray, G., Cady, C., Kaschner, G., 1999. High–rate material modelling and validation using the Taylor cylinder impact test. Philosophical Transactions of the Royal Society of London A: Mathematical, Physical and Engineering Sciences 357, 1707-1729.

Mecking, H., Kocks, U.F., 1981. Kinetics of flow and strain-hardening. Acta Metall. Mater. 29, 1865-1875.

Methfessel, M., Paxton, A., 1989. High-precision sampling for Brillouin-zone integration in metals. Physical Review B 40, 3616.

Miraglia, M., Dawson, P., Leffers, T., 2007. On the influence of mechanical environment on the emergence of brass textures in FCC metals. Acta. Mater. 55, 799-812.

Molodov, K.D., Al-Samman, T., Molodov, D.A., 2017. Profuse slip transmission across twin boundaries in magnesium. Acta. Mater. 124, 397-409.

Monkhorst, H.J., Pack, J.D., 1976. Special points for Brillouin-zone integrations. Physical Review B 13, 5188.

Nie, J.-F., 2012. Precipitation and Hardening in Magnesium Alloys. Metall. Mater. Trans. A 43, 3891-3939.

Nie, J.F., Muddle, B.C., 2000. Characterisation of strengthening precipitate phases in a Mg–Y–Nd alloy. Acta. Mater. 48, 1691-1703.

Nugmanov, D., Knezevic, M., Zecevic, M., Sitdikov, O., Markushev, M., Beyerlein, I.J., 2018. Origin of plastic anisotropy in (ultra)-fine-grained Mg–Zn–Zr alloy processed by isothermal multi-step forging and rolling: Experiments and modeling. Mater. Sci. Eng. A 713, 81-93.

Perdew, J.P., Burke, K., Ernzerhof, M., 1996. Generalized gradient approximation made simple. Physical review letters 77, 3865.

Proust, G., Tomé, C.N., Kaschner, G.C., 2007. Modeling texture, twinning and hardening evolution during deformation of hexagonal materials. Acta. Mater. 55, 2137-2148.

Raeisinia, B., Agnew, S.R., Akhtar, A., 2011. Incorporation of Solid Solution Alloying Effects into Polycrystal Modeling of Mg Alloys. Metall. Mater. Trans. A 42, 1418-1430.

Robson, J., Stanford, N., Barnett, M., 2011. Effect of precipitate shape on slip and twinning in magnesium alloys. Acta. Mater. 59, 1945-1956.

Savage, D.J., Feng, Z., Knezevic, M., 2021. Identification of crystal plasticity model parameters by multi-objective optimization integrating microstructural evolution and mechanical data. Computer Methods in Applied Mechanics and Engineering 379, 113747.

Savage, D.J., Knezevic, M., 2015. Computer implementations of iterative and non-iterative crystal plasticity solvers on high performance graphics hardware. Computational Mechanics 56, 677–690.

Savage, D.J., McWilliams, B.A., Vogel, S.C., Trujillo, C.P., Beyerlein, I.J., Knezevic, M., 2020. Mechanical behavior and texture evolution of WE43 magnesium-rare earth alloy in Split-Hopkinson Pressure Bar and Taylor Impact Cylinder Testing. International Journal of Impact Engineering 143, 103589.

Slutsky, L.J., Garland, C.W., 1957. Elastic Constants of Magnesium from 4.2 K to 300 K. Physical Review 107, 972-976.

Su, Y., Ardeljan, M., Knezevic, M., Jain, M., Pathak, S., Beyerlein, I.J., 2020. Elastic constants of pure body-centered cubic Mg in nanolaminates. Comput. Mater. Sci. 174, 109501.

Su, Y., Xu, S., Beyerlein, I.J., 2019a. Ab initio-informed phase-field modeling of dislocation core structures in equal-molar CoNiRu multi-principal element alloys. Modelling and Simulation in Materials Science and Engineering 27, 084001.

Su, Y., Xu, S., Beyerlein, I.J., 2019b. Density functional theory calculations of generalized stacking fault energy surfaces for eight face-centered cubic transition metals. J. Appl. Phys. 126, 105112.

Sugimoto, K., Niiya, K., Okamoto, T., Kishitake, K., 1977. A study of damping capacity in magnesium alloys. Transactions of the Japan Institute of Metals 18, 277-288.

Takajo, S., Brown, D.W., Clausen, B., Gray, G.T., Knapp, C.M., Martinez, D.T., Trujillo, C.P., Vogel, S.C., 2018. Spatially resolved texture and microstructure evolution of additively manufactured and gas gun deformed 304L stainless steel investigated by neutron diffraction and electron backscatter diffraction. Powder Diffraction 33, 141-146.

Ulacia, I., Dudamell, N.V., Gálvez, F., Yi, S., Pérez-Prado, M.T., Hurtado, I., 2010. Mechanical behavior and microstructural evolution of a Mg AZ31 sheet at dynamic strain rates. Acta. Mater. 58, 2988-2998.

Van Houtte, P., 1978. Simulation of the rolling and shear texture of brass by the Taylor theory adapted for mechanical twinning. Acta Metall. Mater. 26, 591-604.

Vasilev, E., Zecevic, M., McCabe, R.J., Knezevic, M., 2020. Experimental verification of a crystal plasticity-based simulation framework for predicting microstructure and geometric shape changes: Application to bending and Taylor impact testing of Zr. International Journal of Impact Engineering 144, 103655.

Watanabe, H., Ishikawa, K., 2009. Effect of texture on high temperature deformation behavior at high strain rates in a Mg–3Al–1Zn alloy. Mater. Sci. Eng. A 523, 304-311.

Watanabe, H., Mukai, T., Sugioka, M., Ishikawa, K., 2004. Elastic and damping properties from room temperature to 673 K in an AZ31 magnesium alloy. Scr. Mater. 51, 291-295.

Xiang, C., Gupta, N., Coelho, P., Cho, K., 2018. Effect of microstructure on tensile and compressive behavior of WE43 alloy in as cast and heat treated conditions. Mater. Sci. Eng. A 710, 74-85.

Xie, K.Y., Alam, Z., Caffee, A., Hemker, K.J., 2016. Pyramidal I slip in c-axis compressed Mg single crystals. Scr. Mater. 112, 75-78.

Xie, K.Y., Zhao, D., Leu, B., Ma, X., Jiao, Q., El-Awady, J.A., Weihs, T.P., Beyerlein, I.J., Kumar, M.A., 2021. Understanding the interaction of extension twinning and basal-plate precipitates in Mg-9Al using precession electron diffraction. Materialia 15, 101044.

Yaddanapudi, K., Leu, B., Kumar, M.A., Wang, X., Schoenung, J.M., Lavernia, E.J., Rupert, T.J., Beyerlein, I.J., Mahajan, S., 2021. Accommodation and formation of {1¯012} twins in Mg-Y alloys. Acta. Mater. 204, 116514.

Yasi, J.A., Hector, L.G., Trinkle, D.R., 2010. First-principles data for solid-solution strengthening of magnesium: From geometry and chemistry to properties. Acta. Mater. 58, 5704-5713.

Yoo, M.H., 1981. Slip, twinning, and fracture in hexagonal close-packed metals. Metall. Mater. Trans. A 12, 409–418.

Zecevic, M., Beyerlein, I.J., Knezevic, M., 2018. Activity of pyramidal I and II <c+a> slip in Mg alloys as revealed by texture development. J. Mech. Phys. Solids 111, 290-307.

Zecevic, M., Beyerlein, I.J., McCabe, R.J., McWilliams, B.A., Knezevic, M., 2016. Transitioning rate sensitivities across multiple length scales: Microstructure-property relationships in the Taylor cylinder impact test on zirconium. Int. J. Plast. 84, 138-159.

Zecevic, M., Knezevic, M., 2018. A new visco-plastic self-consistent formulation implicit in dislocation-based hardening within implicit finite elements: Application to high strain rate and impact deformation of tantalum. Computer Methods in Applied Mechanics and Engineering 341, 888-916.

Chapter 2: A parametric study into the influence of Taylor-type scale-bridging artifacts on accuracy of multi-level crystal plasticity finite element models for Mg alloys

This chapter has been submitted to the Journal of Mechanics and Materials on March 1st, 2023, and is currently under review.

My contribution to this work was model and mesh generation as well as running the simulations at Quasi-static and high strain-rates for tension, compression, simple-shear, and plane strain deformation conditions. All data acquisition post processing and figure generation was completed by myself along with the first draft. The text was written in a standard student-mentor relationship with the help of Daniel Savage at Los Alamos National Laboratory.

A parametric study into the influence of Taylor-type scale-bridging artifacts on accuracy of multi-level crystal plasticity finite element models for Mg alloys

Jacob Weiss [1], Daniel J. Savage [2], Marko Knezevic [1, *]

[1] Department of Mechanical Engineering, University of New Hampshire, Durham, NH 03824, USA

[2] Los Alamos National Laboratory, Los Alamos NM 87545, USA

[*] Corresponding author at: University of New Hampshire, Department of Mechanical Engineering, 33 Academic Way, Kingsbury Hall, W119, Durham, New Hampshire 03824, United States. E-*mail address*: marko.knezevic@unh.edu (M. Knezevic).

Abstract

Meshing grain structures explicitly to incorporate microstructure dependent material behavior in modeling tools for metal forming processes and structural components is unfeasible. Grain-to-polycrystal meso-level homogenization theories are employed to embed polycrystal plasticity constitutive laws in finite element (FE) frameworks, which hence relate the meso-scale to the macro-scale response. A Taylor-type polycrystal plasticity (T-CP) theory is often used at the meso-scale within FE frameworks (T-CPFE) owing to its simplicity and computational efficiency. The theory relies on the iso-strain constraint imposed over constituent grains at each integration point. The constraint can be relaxed by spreading orientation distributions over finite elements in a mesh. This work seeks to establish an optimal number of crystal orientations to spread over integration

points for accurate modeling of Mg alloys. Quasi-static and high strain-rates simulations of tension, compression, simple-shear, and plane strain deformation conditions are performed and post-processed to reveal the differences in predicted mechanical fields between T-CPFE and an explicit polycrystalline grain microstructure of an AZ31 Mg alloy. Moreover, several flow stress curves of the alloy are simulated and compared with measured data. A range of meshes with variable degree of relaxed constraints at integration points are suitably designed and used in the simulations. The performance of the six crystals per integration point is established to be a sweet spot in smoothing local deformation while allowing heterogenous deformation over the mesh. As such, the relaxed Taylor homogenization can provide tractable part level simulations of Mg alloys.

Keywords: Crystal plasticity; Homogenization schemes; Taylor-type model; Finite element method; Microstructures

1. Introduction

Reducing structural weight is a strategy to reduce consumption of fossil-fuels in transportation. Mg alloys are being increasingly evaluated to contribute to such efforts owing to a set of desirable properties (Cho et al., 2009; Mordike and Ebert, 2001). Mechanical behavior of Mg alloys has been extensively studied experimentally and modeled (Lou et al., 2007). Crystal plasticity models considering crystallography of hexagonal close packed (HCP) crystal structure and deformation mechanisms of slip and twinning have been particularly effective at capturing the evolution of strength and underlying microstructure during plastic deformation of Mg alloys (Proust et al., 2007; Tam et al., 2021). In these models, a polycrystalline aggregate response is a result of the collective responses of constituent grains having different crystal orientation and size/shape (Kocks et al., 1998). The aggregate response can be obtained using spatially resolved full-field and mean-field homogenization schemes.

The full-field mechanics tools account for grain-to-grain interactions under uniform macroscopic loading over a suitably discretized spatio-temporal domain while calculating inhomogeneous mechanical fields defined in term of stress and strain stemming from complex grain structures, multiple phases, and non-uniform boundary conditions (Jahedi et al., 2015; Keshavarz and Ghosh, 2015; Lebensohn et al., 2012). Beginning from the work presented in (Peirce et al., 1982), the finite element (FE) method computational tools have been extensively used to solve such mechanical fields to sub-grain resolution (Diard et al., 2002; Lim et al., 2014; Zecevic et al., 2015; Zhao et al., 2008). Various tools have been developed to construct FE meshes representative of grain structures to run full-field models (Barrett et al., 2018). Green's function methods provide an alternative to FE solvers of the field equations over spatial domains (Lebensohn, 2001). These methods are attractive because the fast Fourier transform (FFT) algorithms can be used to solve

the convolution integral representing equilibrium in stress under the strain compatibility over voxel-based microstructural cells yielding substantial computational efficiency (Eghtesad et al., 2017; Lebensohn et al., 2008; Liu et al., 2010). These works bring insight into internal stresses developed within grains due to plastic incompatibilities. Grain averaged stresses predicted by full-field models have been validated through high-energy synchrotron X-ray diffraction measurements (Abdolvand et al., 2015; Cocke et al., 2021; Erinosho et al., 2016; Naragani et al., 2021). Nevertheless, the full-field modes are costly in terms of compute resources requiring substantial ram and cpus to perform a simulation. Moreover, efforts have just begun towards modeling of discrete twin domains and phase transformations within full-field individual grains (Ardeljan et al., 2015; Cheng and Ghosh, 2017; Knezevic et al., 2016a). Performing forming simulations is not tractable using full-field models.

The mean-field mechanics tools homogenize the surroundings of each grain without accounting for grain-to-grain interactions in linking the local behavior of grains to that of a polycrystalline aggregate (Knezevic et al., 2008; Knezevic and Savage, 2014; Lebensohn and Tomé, 1993). While less accurate, these tools have several other advantage over the full-field tools such as improved computational speed, large strain deformations are easier to treat, and their implementation is simpler, especially the implementations of deformation twinning and phase transformations (Feng et al., 2022). Mean-field models have also been experimentally validated via methods such as high-energy synchrotron X-ray diffraction but not to the level of details as full-field models (Barrett et al., 2020; Ferreri et al., 2022). The most commonly used mean-field homogenization schemes tradeoff computational efficiency and accuracy such that the homogeneous effective medium (HEM) self-consistent (SC) models are more accurate, while full constrains (FC) Taylor-type models and more computationally efficient and simple (Hartley et al., 2008; Taylor, 1938). In the

Taylor-type models, each grain is assumed to experience the same strain as the aggregate, while the grain-to-grain (full-field) or grain-to-HEM (SC) interactions are not included. As a result, the FC Taylor-type models violate the equilibrium over grains. The equilibrium conditions across the grain boundaries are violated because the vertex stress states required to activate multiple slip in each grain vary from grain to grain. The FC Taylor-type models are less suitable to simulate plastic deformation of low-symmetry polycrystalline metals because the strong constraints that these models impose upon strains are incompatible with the shortage of independent slip systems (Tomé et al., 1991). This can create complex artifacts such as unrealistic slip activation stresses. The effect is more pronounced in strongly textures low symmetry metals with unfavorably oriented grains to accommodate deformation.

Given that the FC Taylor-type models provide computational efficiency with reasonable accuracy, they have been coupled with implicit FE frameworks (Kalidindi et al., 1992; Zecevic and Knezevic, 2018). In such coupled framework, every integration point (IP) embeds a polycrystal whose response is obtained by the Taylor-type iso-strain homogenization. Variable strain fields over FE IPs provide local boundary conditions to interrogate Taylor-type models while relaxing the iso-strain homogenization assumption. The coupled Taylor-type polycrystal plasticity (T-CP) theory and implicit FEs is termed T-CPFE (Ardeljan et al., 2016). The T-CPFE framework is a two-level model consisting of the meso-level homogenization using the Taylor model and the macro-level homogenization induced by FEs. The latter relaxes the iso-strain assumption of the Taylor model as a polycrystal is spread over FE IPs, while each grain embedded at a given IP experiences the same applied deformation gradient/strain. In summary, the FE homogenization occurs over many Taylor-type models running at FE IPs relaxing the Taylor-type mode constraints.

Significantly, T-CPFE performs well in modeling mechanical response and texture evolution of anisotropic metals like Mg alloys (Feather et al., 2019; Feather et al., 2021b).

Alternative methodologies aimed at relaxing the Taylor-type model constraints have been extensively researched (Van Houtte et al., 1999; Van Houtte et al., 2005). These methodologies involve grain cluster sub-models as an approach to achieve predictions that lie between mean-field schemes and spatially resolved solutions (Eisenlohr et al., 2009; Engler et al., 2005; Riyad et al., 2023). The addition of grain cluster aggregates allows for the relaxtion of the assumption of homogenous strain in each consituent. However, these approaches can lead to an oversetimation of the polycrustaline strength and rate of texture evoltuion owing to the rigidity of the clusters made up of crystals interacting under certain boundry condtions (Roters et al., 2010; Van Houtte et al., 2002). FE implementations of VPSC (visco-plastic self-consistent) (Knezevic et al., 2013b; Segurado et al., 2012) and EPSC (elasto-plastic self-consistent) (Zecevic et al., 2017; Zecevic and Knezevic, 2017) homogenizations embedding a sub-polycrystal at ever FE IP have also been developed. Since SC iterations follow an initial Taylor guess, these models are several times slower than the Taylor-type models. The primary advantage of such multi-level analyises with a meso-level homogoenization scheme is that relevant and analitical information can be taken into account into macroscopic simulations and analyses (Tjahjanto et al., 2015). While one grain per IP leads to excessive relaxation, many grains per IP promote excessive constraints. While one grain per IP maximizes computational efficiency, many grains per IP slow down calculations. The parametric work performed here is aimed at providing guidance on effective use of these multi-level models to provide appropriate level of relaxation for accuracy.

A large number of simulations are performed including tension, compression, shear, and plane strain compression under quasi-static and high strain rates using a range of relaxed T-CPFE models

as well as a full field polycrystalline grain model. Variances in mechanical fields as functions of mesh density and dispersal of initial polycrystal texture over the FE meshes are determined between the relaxed T-CPFE and full-field calculations for alloy AZ31. Moreover, several flow stress curves are simulated using a range of relaxed T-CPFE models are compared with measured data for alloy AZ31 to evaluate differences in the predictions including activities of deformation modes and texture evolution. Based on the comprehensive data, homogenization artifacts and optimal relaxation of the constraints are discussed for accurate modeling involving the multi-level models.

2. Modeling framework

In this section, the finite deformation T-CPFE model relevant to the study and simulation setups are summarized. In the first sub-section, salient kinematics are focused on for completeness of the present work, while in the second sub-section, the FE meshes and a grain structure are defined for the parametric study. The T-CFPE model defined here is a multi-level formulation that bridges the constitutive response of single crystals and part scale geometries. The model was originally developed in (Ardeljan et al., 2016) and extended and calibrated in (Feather et al., 2021b) for the experimental data presented in this work. The model was set to consider strain rate sensitivities inherent to deformation mechanisms for modeling of quasi-static and high strain rate deformation of AZ31. The model is summarized below, while the dislocation density-based hardening law and associated parameters are the same as those in (Feather et al., 2021b) and are not repeated here.

2.1 T-CPFE formulation

The T-CPFE model is implemented as a user material subroutine (UMAT) in Abaqus Standard. The implicit FE solver of Abaqus iteratively provides a guess displacement field at current time, τ (t+Δt), under imposed boundary conditions over the FE model. An iso-deformation gradient, **F**, available at each IP is used to interrogate the UMAT at each gauss. The UMAT solves for Cauchy stress, $\overline{\boldsymbol{\sigma}}$, calculates the Jacobian, and updates state variables. Tensor quantities are denoted as bold letters; tensor components and scalars are italic and not bold letters; s, α, t, and β are used to denote slip systems, slip modes, twin systems, and twin modes, respectively; $\cdot$ is used for a dot product, while $\otimes$ is for a tensor product. N^{sl} and N^{tw} are the total number of slip and twin systems.

The stress at each IP is volume averaged over crystal stresses of grains and twins as

$$\overline{\boldsymbol{\sigma}} = \langle \boldsymbol{\sigma} \rangle = \sum_{k=1}^{N_{grains}} v_k \boldsymbol{\sigma}_k \,, \tag{1}$$

where k numbers grains and twins, v are weights, and $\langle\ \rangle$ stands for the volume average.

Grains/twins embedded at a given FE IP experience the same applied iso-deformation gradient, **F**, according to the Taylor-type model constraint. The tensor **F** is decomposed into its elastic and plastic components as

$$\mathbf{F} = \mathbf{F}^e \mathbf{F}^p. \tag{2}$$

The rate of change of $\mathbf{F}^p$ is

$$\dot{\mathbf{F}}^p = \mathbf{L}^p \mathbf{F}^p. \tag{3}$$

Integrating Eq. (3) from time at the beginning of the given strain increment, t, to the current time, $\tau = t+\Delta t$, produces

$$\mathbf{F}^p(\tau) = exp(\mathbf{L}^p(\tau)\Delta t)\mathbf{F}^p(t). \quad (4)$$

The constitutive relations at the grain level are

$$\mathbf{T} = \mathbf{C}\mathbf{E}^e, \text{ with } \mathbf{T} = \mathbf{F}^{e^{-1}}\{(det\mathbf{F}^e)\boldsymbol{\sigma}\}\mathbf{F}^{e^{-T}} \text{ and } \mathbf{E}^e = \frac{1}{2}\{\mathbf{F}^{e^T}\mathbf{F}^e - \mathbf{I}\}, \quad (5)$$

with $\mathbf{T}$ as the second Piola-Kirchhoff stress tensor, $\mathbf{E}^e$ as the Lagrangian strain tensor, and $\mathbf{C}$ as the fourth-order elastic stiffness tensor. The stiffness tensor per grain is calculated based on elastic crystal constants: C_{11} = 59,500 MPa, C_{12} = 26,100 MPa, C_{13} = 21,800 MPa, C_{33} = 65,600 MPa, C_{44} = 16,300 MPa for Mg (Duvvuru et al., 2007; Knezevic and Kalidindi, 2007; Landry and Knezevic, 2015; Slutsky and Garland, 1957). $\mathbf{F}^e$ must be known to calculate stress using $\mathbf{F}^e(\tau) = \mathbf{F}\mathbf{F}^{p^{-1}}(\tau) = \mathbf{F}\mathbf{F}^{p^{-1}}(t)\{\mathbf{I} - \Delta t\mathbf{L}^p(\tau)\}$ for what $\mathbf{L}^p$ must be known. $\mathbf{L}$ is additively decomposed to its plastic, $\mathbf{L}^p$, and elastic, $\mathbf{L}^e$, parts. The former consists slip and twinning shearing contributions as

$$\mathbf{L} = \mathbf{L}^e + \mathbf{L}^p = \mathbf{L}^e + \mathbf{L}^{sl} + \mathbf{L}^{tw} = \mathbf{L}^e + \sum_s^{N^{sl}} \dot{\gamma}^s \mathbf{S}_0^s + \sum_t^{N^{tw}} \dot{f}^t S^t \mathbf{S}_0^t. \quad (6)$$

In Eq. (6), $\mathbf{S}_0^s = \mathbf{b}_0^s \otimes \mathbf{n}_0^s$ and $\mathbf{S}_0^t = \mathbf{b}_0^t \otimes \mathbf{n}_0^t$ are Schmid tensors for slip, *s*, and twinning, *t*, in the reference configuration, $_0$. These Schmid tensors are based $\mathbf{b}_0^s$ and $\mathbf{b}_0^t$ indicating Burgers vectors and $\mathbf{n}_0^s$, and $\mathbf{n}_0^t$ indicating plane normal vectors. $\dot{\gamma}^s$ is the rate of shearing, while S^t is the intrinsic shear strain for twin systems. The rate of change of twin volume fraction is $\dot{f}^t = \frac{\dot{\gamma}^t}{S^t}$ (Kalidindi, 1998; Van Houtte, 1978). Basal **a** $\{0001\}\langle\bar{1}\bar{1}20\rangle$, prismatic **a** $\{\bar{1}100\}\langle\bar{1}\bar{1}20\rangle$, and pyramidal **c**+**a** $\{\bar{1}\bar{1}22\}\langle\bar{1}\bar{1}2\bar{3}\rangle$ slip modes, **c**-axis extension $\{10\bar{1}2\}\langle\bar{1}011\rangle$ (TT1) and **c**-axis contraction $\{10\bar{1}1\}\langle10\bar{1}\bar{2}\rangle$ (CT2) twin modes, and double twinning sequence $\{10\bar{1}1\} - \{10\bar{1}2\}$ (DTW) was allowed to activate.

The power-law relationship is used to calculate the shear rates for slip and twinning i.e. $\dot{\gamma}^s$ and $\dot{\gamma}^t$, in the visco-pastic framework (Asaro and Needleman, 1985; Hutchinson, 1976; Kalidindi, 1998). Given that the power-law equations are equivalent for slip and twinning (with twinning being restricted to carry out only positive shearing), the power-law equation for slip systems is presented only

$$\dot{\gamma}^s=\dot{\gamma}_0 \left(\frac{|\tau^s|}{\tau_c^s(\dot{\varepsilon},T)}\right)^{\frac{1}{m}} \text{sign}(\tau^s) \text{ with } \tau^s = \mathbf{T}\cdot\mathbf{S}_0^s, \tag{7}$$

where $\dot{\gamma}_0$ is a reference value for shearing rate ($\dot{\gamma}_0 = 0.001\ \text{s}^{-1}$), τ^s is the resolved shear stress on system *s*, τ_c^s is a threshold value to slip, and $\frac{1}{m}$ is the power-law exponent with m representing a strain-rate sensitivity. The exponent, $\frac{1}{m} = n$, must be properly set to ensure selection of slip/twin systems accommodating plastic strains, while not introducing any inappropriate *constant structure* strain-rate sensitivity (constant structure means constant τ_c^s and constant dislocation density). Increase of the exponent over 20 does not alter slip system activities, and thus does not alter the direction of strain rate or stress but only the magnitude of the stress. Small values of the exponent like <100 are numerically easy to handle but prevent simulating high strain-rate deformation because of unrealistically high values of stress (Knezevic et al., 2016b; Zecevic et al., 2016). If n is too small like $n < 20$, the selection of active slip systems is not unique. On the other hand, big values of the exponent like >100 cause numerical challenges in solving the equations become they become extremely stiff. However, the strain-rate sensitivity values are realistic for alloys and stress values are normal. The sensitivity reduces with increasing *n* up to a strain rate insensitive limit of $n \to \infty$. The sensitivity due to the exponent must not be interchanged with a strain-rate sensitive evolution of threshold resistances, τ_c^s, and governing dislocation density as described by the thermodynamics of slip (Follansbee and Kocks, 1988; Kocks et al., 1975). This strain-rate

sensitivity is referred to as the *evolving structure* sensitivity as opposed to the constant structure sensitivity governed by the exponent. The T-CPFE model represents both of these sources of strain rate sensitivity. The evolving structure sensitivity is embedded in the hardening law (Feather et al., 2021b), while the power-law exponent sensitivity is handled using a recently developed scheme referred to as the *k*-modification (*k*-mod) method (Knezevic et al., 2016b). The method was implemented in T-CPFE in (Feather et al., 2021b).

In the method, an applied plastic stretching tensor at each IP, $\mathbf{D}^{app}$, is appropriately modified to influence the magnitude of stress in grains as

$$\mathbf{D}^{p} = \frac{\mathbf{D}^{app}}{|\mathbf{D}^{app}|}|\mathbf{D}^{app}|^{\frac{1}{k+1}} \text{ with } \mathbf{D}^{p} = \frac{1}{2}\left(\mathbf{L}^{p} + \mathbf{L}^{p^{T}}\right), \tag{8}$$

The inverse relation is

$$\mathbf{D}^{app} = \mathbf{D}^{p}|\mathbf{D}^{app}|^{\frac{k}{k+1}} = \mathbf{D}^{p}|\mathbf{D}^{p}|^{k}. \tag{9}$$

Eqs. (8) and (9) indicate that $\mathbf{D}^{p}$ attains unity as *k* rises. Given an applied stretching, $\mathbf{D}^{app}$, scaled according to $\lambda\mathbf{D}^{app}$, the modified stretching used for evaluating stress in grains is $\lambda^{\frac{1}{k+1}}\mathbf{D}^{p}$. Consequently, the grain stresses, $\mathbf{T}$ and $\boldsymbol{\sigma}$ scale correspondingly i.e. $\lambda^{\frac{1}{(k+1)n}}\boldsymbol{\sigma}$. The homogenized stress is $\lambda^{\frac{1}{(k+1)n}}\overline{\boldsymbol{\sigma}}$. Therefore, the *k*-mod adjusts the strain rate sensitivity, *m*, using both *n* and *k*: $m=1/((k+1)n)$.

Since the *k*-mod method changes the rate of plastic stretching in grains from $\mathbf{D}^{app}$ to $\mathbf{D}^{p}$, to ensure that every grain accommodates $\mathbf{D}^{app}$, the calculated shearing rates must be adjusted as

$$\mathbf{D}^{p,app} = \frac{\left|\mathbf{D}^{app}\right|}{\left|\mathbf{D}^{app}\right|^{\frac{1}{k+1}}}\sum_{s}\mathbf{P}_{0}^{s}\dot{\gamma}^{s} = \sum_{s}\mathbf{P}_{0}^{s}\dot{\gamma}_{k-\mathrm{mod}}^{s} \text{ with } \mathbf{P}_{0}^{s} = \frac{1}{2}(\mathbf{S}_{0}^{s} + (\mathbf{S}_{0}^{s})^{T}), \tag{10}$$

so that the shearing rates in T-CPFE are

$$\dot{\gamma}^{s}_{k-\mathrm{mod}} = \frac{\left|\mathbf{D}^{app}\right|}{\left|\mathbf{D}^{app}\right|^{\frac{1}{k+1}}} \dot{\gamma}_0 \left(\frac{\left|\mathbf{T}\cdot\mathbf{P}^{s}_{0}\right|}{\tau_c{}^{s}} \right)^{n} \mathrm{sgn}\left(\mathbf{T}\cdot\mathbf{P}^{s}_{0}\right). \tag{11}$$

2.2 Finite element model meshes

The FE models with grid meshes shown in Fig. 1(a-f) and Fig. 2 were generated using ABAQUS Standard 2019 meshing tools. The various mesh densities in Fig. 1 were chosen to allow for multiples of a set of 1,012 weighted orientations to be placed at FE IPs. This ensures that the resulting model behavior is not a function of the polycrystal orientation component volumes and allows a wide range of mesh and Taylor polycrystal combinations to be tested, thereby isolating effects of homogenization. The chosen element type is a continuous three-dimensional eight node and integration point linear hexahedral element (C3D8). Applying conventional knowledge that the full-field grain model should most accurately account for grain-to-grain interactions, the 1,012 polycrystalline grain model, Fig. 1(h), is taken as a reference model to which all other models in Table.1 and Fig.1 are compared. The wights of 1,012 orientations correspond to size of the grains of the grain model.

The full-field 1,012 grain model was generated using Sculpt meshing tool along with Cubit Meshing and Geometry Toolkit developed by Sandia National Laboratories according to the procedure developed in (Feather et al., 2021a). Volume fractions of grains and interfaces to create the grain boundaries were defined in dream.3d (Groeber and Jackson, 2014). The voxelated microstructure is meshed with Cubit/Sculpt to create the hexahedral mesh. A smoothing step is

preformed to clean up the interface planes and resolve the voxelated stair step grain boundaries, ensuring the quality of the hexahedral mesh boundaries.

To explore homogenization artifacts at large strains along with exact comparisons between Taylor polycrystal sizes, a second set of models are generated according to Table 2 as shown in Fig. 2.

Table 1. Finite element model names, meshes size, and orientation statistics distributing the 1012 weighted orientations across models. The CIP number specifies the number of crystals per integration point, IP (i.e. the size of the Taylor polycrystal) and the FF designation stands for full-field, explicit grain structure model.

Name	CIP1012	CIP48	CIP9	CIP6	CIP3	CIP1	CIP1-FF
# Elements per mesh	1x1x1 =1	6x7x6 =252	11x12x11 =1452	13x13x12 =2028	13x26x12 =4056	24x23x23 =12696	594,100
# Elements x # IP per element x # 1012	1x8x1012 =8096	252x8x48 =96786	1452x8x9 =104544	2028x8x6 =97344	4056x8x3 =97344	12696x8x1 =101568	-
# Orientations in multiples of 1012 + difference	1012x8 +0 =8096	95x1012 +628 =96768	103x1012 +308 =104544	96x1012+ 192 =97344	96x1012+ 192 =97344	100x1012 +368 =101568	1012

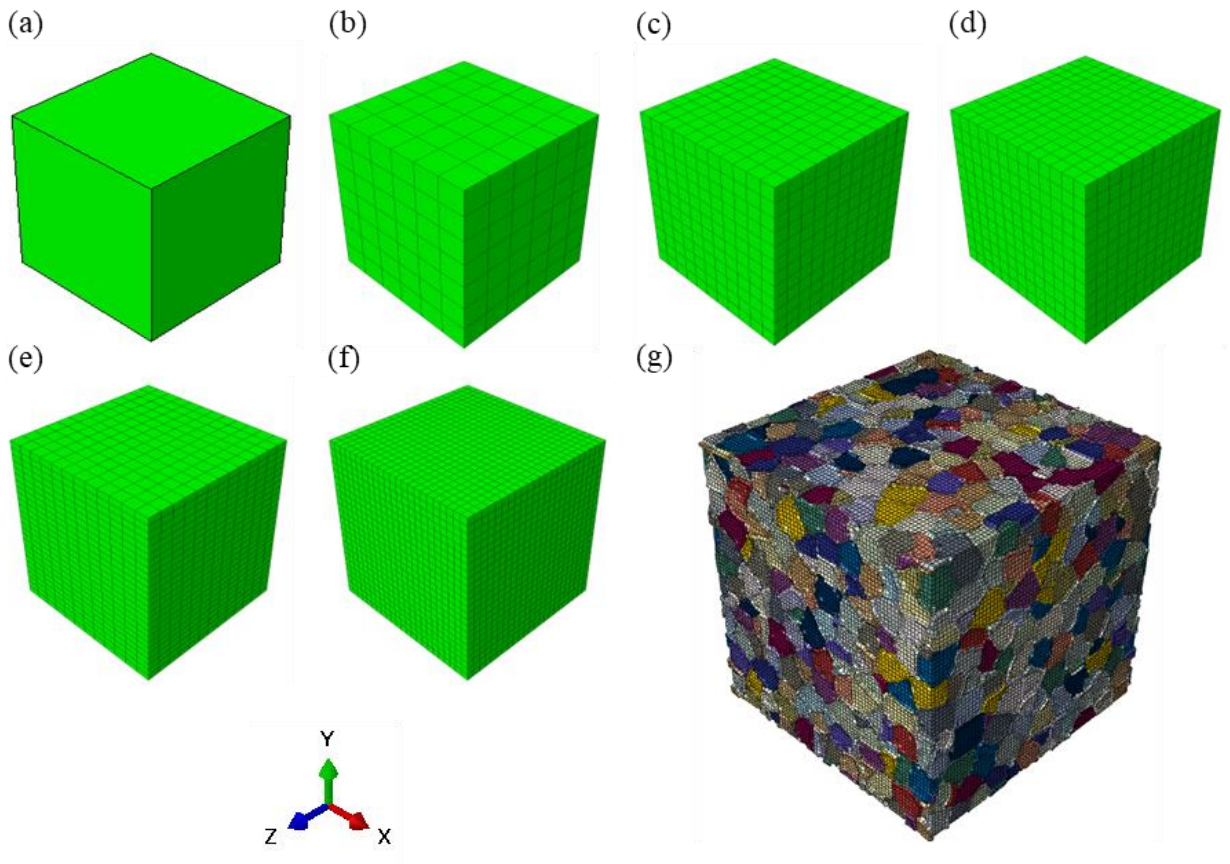

Figure 1. Finite element models used to compare the influence of Taylor-type homogenization artifacts on accuracy. The models are labeled according to Table 1 based on the number of embedded weighted crystals per integration point (CPI): (a) CIP1012, (b) CIP48, (c) CIP9, (d) CIP6, (e) CIP3, (f) CIP1, and (g) CIP1-FF (i.e. the explicit grain structure full field (FF) model containing 1,012 grains).

Table 2. Finite element model meshes size and statistics enabling the exact comparison of texture consisting of 3,072 unweighted orientations. The CIP#E designation stands for the number of crystals per integration point (IP).

Name	CIP384E	CIP3072E	CIP48E	CIP6E	CIP1E
# Elements per mesh	1x1x1=1	1x1x1=1	2x2x2=8	4x4x4=64	24x24x24=13824
# Crystals per IP	384	3072	48	6	1
# Orientations in multiples of 3072	1x8x384= 3072	1x8x3072= 24576	8x8x48= 3072	6x8x64= 3072	1x8x13824= 36x3072= 110592

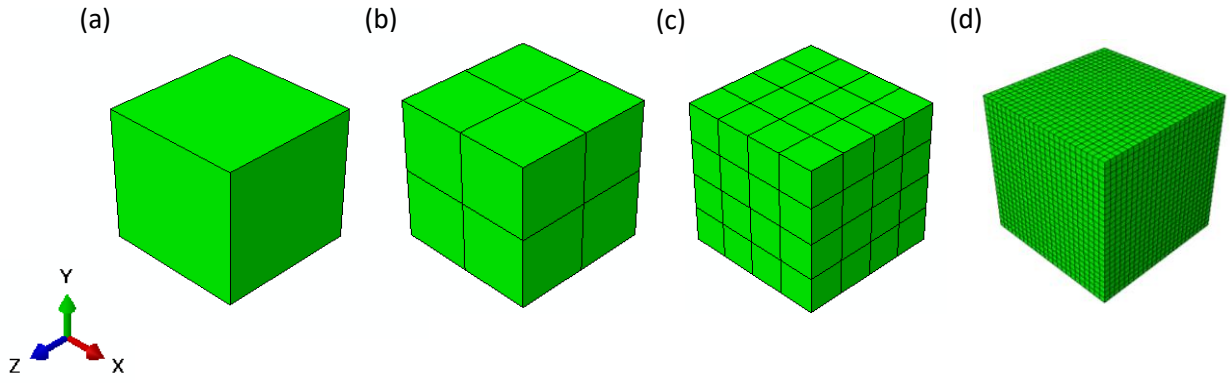

Figure 2. Finite element models according to Table 2: (a) CIP384E & CIP3072E, (b) CIP48E, (c) CIP6E, and (d) CIP1E.

Tension and compression boundary conditions were prescribed by defining a displacement on normal to a surface while the lateral surfaces were free. The shear cases were defined similarly to the tension and compression case, but the prescribed displacement was along the x on the positive z face, and the negative z face was constrained in the x direction. Plane-strain was preformed where there was no strain in the x direction and deformation only occurred on the y-z plane. All

simulations were run to 0.1 strain except for the 1,012 polycrystalline grain model which was run only to 0.02 strain due to the explicit twin nucleation and growth not being modeled in the FE framework.

3. Experimental data

The experimental data compared with the models in this study is from (Kurukuri et al., 2014). The rolled sheet of Mg alloy AZ31B annealed in the O-temper condition was used. The alloy had equiaxed grains with a 12-μm average diameter. Pole figures of the initial texture in the sheet are shown in Fig 3. The sheet has a strong basal texture and most grains have their c-axis orientated in the normal direction (ND) or z. There is slight spreading in the rolling direction (RD) as compared to the transverse direction (TD). Mechanical loading type (e.g. tension, compression, shear, plane strain), rate, and direction, (e.g. RD, TD, ND) relative to the initial rolled sheet crystallographic texture, determine the activity of the various deformation mechanisms that accommodate plasticity.

The alloy was tested under strain-rates from $10^{-3}s^{-1}$ to $10^{3}s^{-1}$ at room temperature. The flow stress in RD compression is roughly strain-rate insensitive for the early portion of deformation. However, the alloys exhibits more strain-rate sensitive behavior with strain. The alloy is stronger in ND compression relative to the RD compression exhibiting some strain-rate sensitivity in ND. The rate of strain hardening is higher for higher strain-rates. In tension, the alloy exhibits high strain-rate sensitivity. Moreover, the alloy shown pronounced tension-compression asymmetry. The asymmetry increases with strain-rate. More detains can be found in (Kurukuri et al., 2014).

From electron backscattered diffraction (EBSD) orientation data an orientation distribution function (ODF) was reconstructed and 3,072 orientations sampled from the ODF using MTEX. The unweighted orientations, 3,072, were compacted using generalized spherical harmonics (GSH) methodology (Eghtesad et al., 2018) to 1,012 weighted orientations and used for the polycrystalline grain structure and comparison microstructures. The GSH methodology ensured that the 3,072 and 1,012 ODFs were not appreciably different.

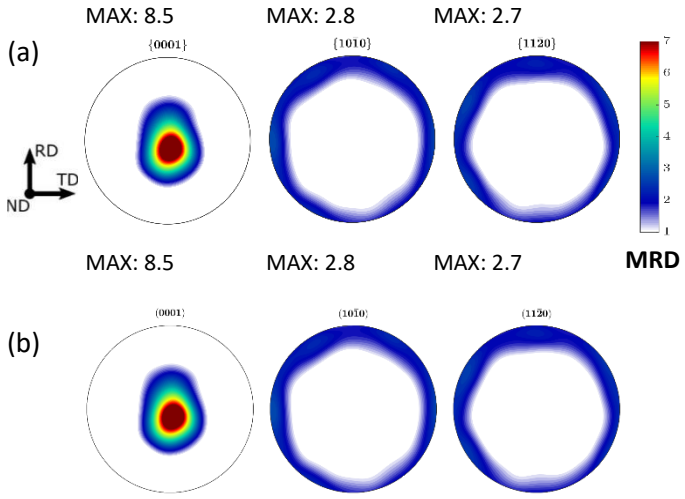

Figure 3. Pole figures showing the initial texture of AZ31 alloy: (a) 3072 unweighted orientations and (b) 1012 weighted orientations. The texture was measured using EBSD.

4. Results

The results of the parametric study are split into two sections: i) initial yield behavior and deformation activities without twin reorientation and a comparison with a full-field explicit grain model and ii) large strain deformation activities and stress response with twin reorientation enabled and a comparison made with experimental data.

4.1 Effects of homogenization scheme at 2% strain

The percent error of the polycrystal averaged von Mises stress at 2% strain between the reference full-field explicit grain model (CIP1-FF) and other models from Table 1 are shown in Fig. 4. The loading cases A-I are summarized in the Fig 4 caption. The largest stress error occurs in CIP1, while the smallest error has CIP6 compared to CIP1-FF. The error is also large for CIP1012. The CIP9 and CIP3 models perform slightly worse than CIP6. Because twin reorientation is disabled, texture variation at 2% should be negligible and the resulting errors are tightly tied to the effect of homogenization on slip and twin activities. There is no trend that suggests certain loadings promote or suppress the differences. We hypothesize the poor stress performance of CIP1 is due to the lack of smoothness in the response at an integration point, while in the CIP1-FF case, the grain domains deform together and do not have the same degree of heterogeneity.

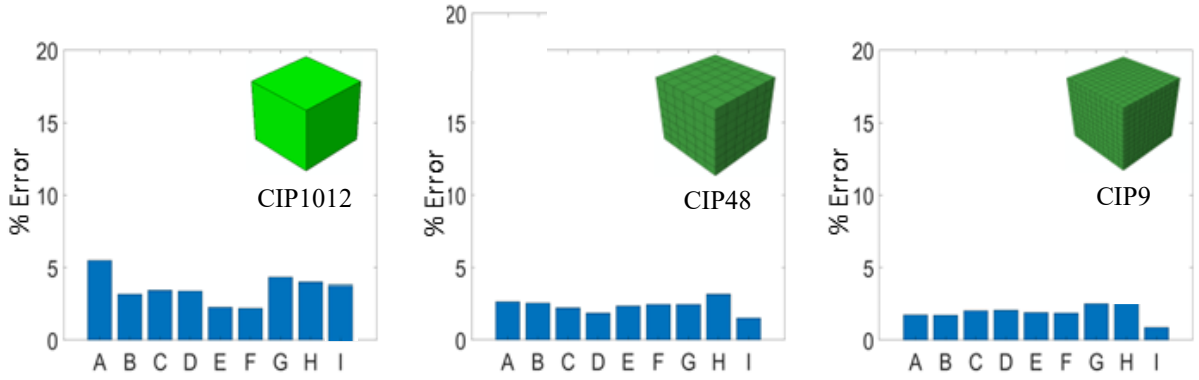

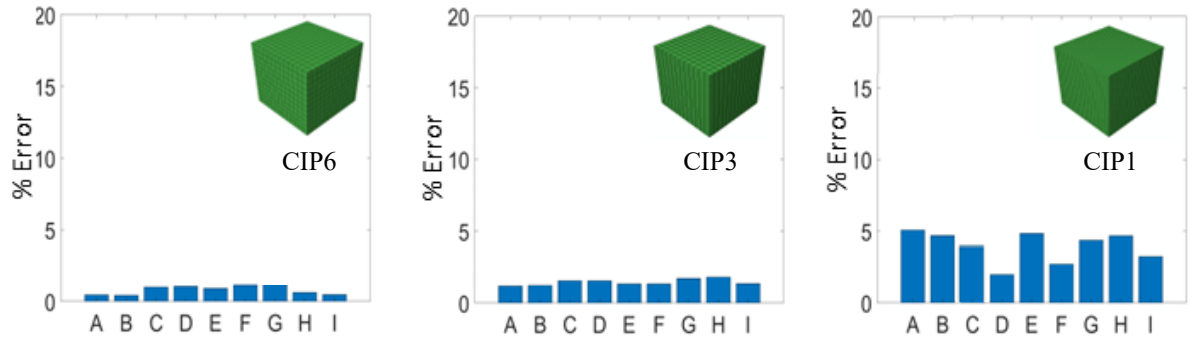

Figure 4. Percent error in von Mises stress at a true strain of 0.02 for the models indicated in the plots relative to the explicit grain structure model CIP1-FF. The loading cases per comparison are: (A) compression in RD under 0.001/s strain rate, (B) compression in RD under 1000/s strain rate, (C) compression in ND under 0.001/s strain rate, (D) compression in ND under 1000/s strain rate, (E) tension in RD under 0.001/s strain rate, (F) tension in RD under 1000/s strain rate, (G) YZ shear under 0.001/s strain rate, (H) YZ shear under 1000/s strain rate, (I) plane strain compression in the XZ direction with no strain occurring in the Y direction under a strain rate of 0.001/s. Note that grain re-orientation due to twinning was not active in all these simulations.

Active slip and twinning systems for the above simulation cases are plotted in Fig. 5 as relative activities for each loading direction and strain rate. The RD compression (A,B) has basal slip and TT1 as the most active, while the ND compression (C,D) is primarily accommodated by pyramidal c+a and basal slip. The RD tension (E,F) is primarily accommodated by prismatic and basal slip. Simple shear (G,H) has predominately basal slip active with some pyramidal c+a and prismatic slip. Plane strain compression (I) exhibits a combination of pyramidal c+a and basal slip. Fig. 5h shows CIP1-FF model for a reference set of activities. Notably, no loading direction or strain rate among the Taylor type models have large differences in activity trends and all simulation have

relatively small errors in von Mises stress (<6%) as compared to the larger full-field models. Nevertheless, CIP6 has slightly more similar slip activities to CIP1-FF compared to other cases, which is consistent with the von Mises errors presented in Fig. 4. However, based on slip activities and stresses at 2% strain all models could likely achieve similar yield values and activities by slight adjustments of hardening parameters. By including twinning and texture evolution in the following section, the compounding effects of these small difference in slip activities will be explored at larger strains.

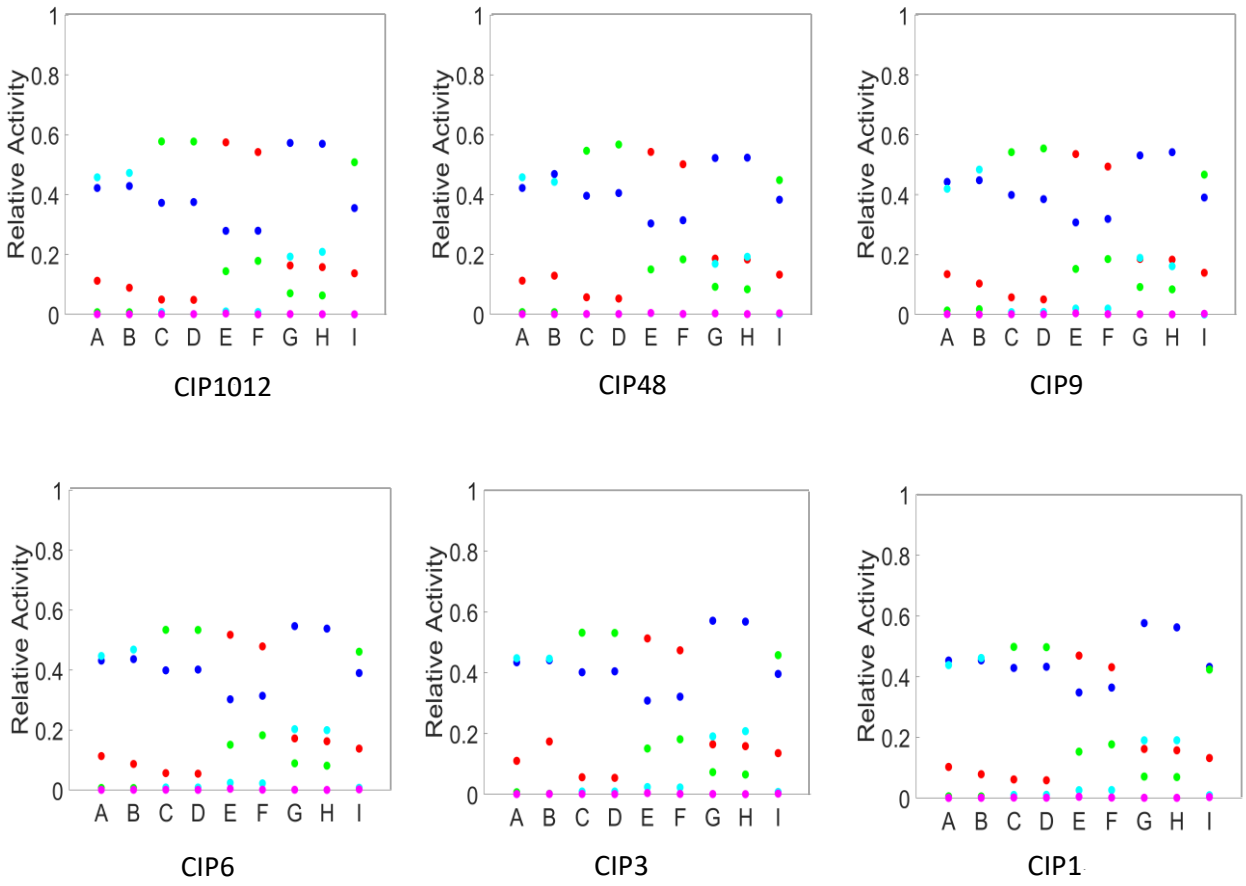

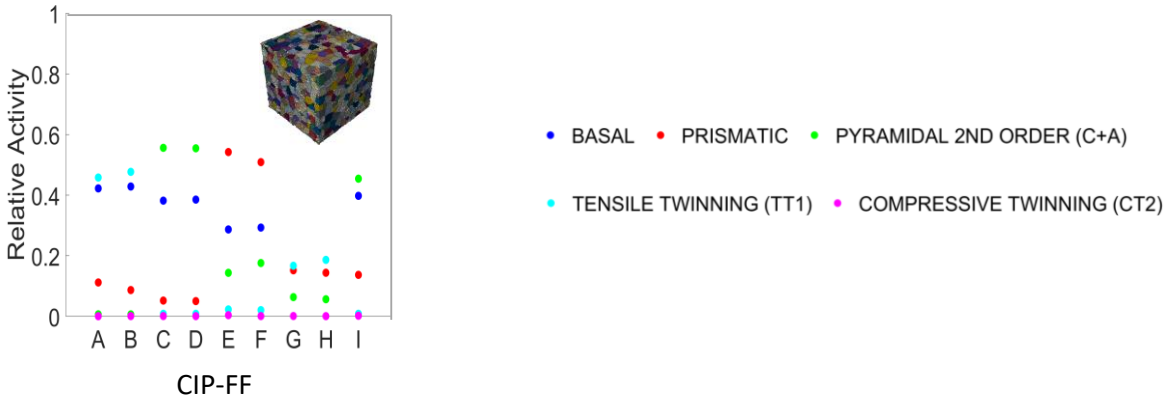

Figure 5. Relative activities of deformation modes at a true strain of 0.02 predicted using the models indicated in the plots. The loading cases are the same as in Fig. 4. Note that grain re-orientation due to twinning was not active in all these simulation cases.

4.2 Large strain behavior

At large strains it is no longer realistic to compare the CIP1-FF model with Taylor models due the lack of twin induced reorientation in CIP1-FF which is inherent to Mg alloys. As a reference, we show the effects of Taylor assumption relaxation with comparisons to experimental data (Kurukuri et al., 2014). With twin reorientation enabled the simulations are run to a strain of 0.1, while the experimental data is to a strain of roughly 0.08. To ensure an exact representation of the polycrystal, the models of Fig. 2 and Table 2 are utilized. In what follows we compare the stress-strain behavior for RD compression and tension at strain-rates of 0.001/s and 1000/s and ND compression at strain-rates of 0.001/s and 1000/s.

Comparisons between experimental stress-strain curves and the models of Table 2 are provided in Fig. 6. In RD tension and compression there are some minor signatures of homogenization effects and only CIP1E at a strain-rate of 1000/s exhibits a change in the initial twinning regime.

Compression along ND and the c-axis fiber where pyramidal c+a slip is most activate exhibits strong sensitivity to the homogenization. The model was calibrated with CIP6E in (Feather et al., 2021b) and represents the best fit that could be achieved with the CIP6E model. The comparison of the early strain behavior in section 4.1 suggests CIP6E should perform well; nonetheless, there are clear model deficiencies in the saturation of hardening which is related to the sensitive interplay between slip modes. This may be explained by the evolution of the stress-strain fluctuations with texture evolution (Tomé, 1999) and approximations in the twinning model. Figs. 7 and 8 quantify the differences observed in Fig. 6.

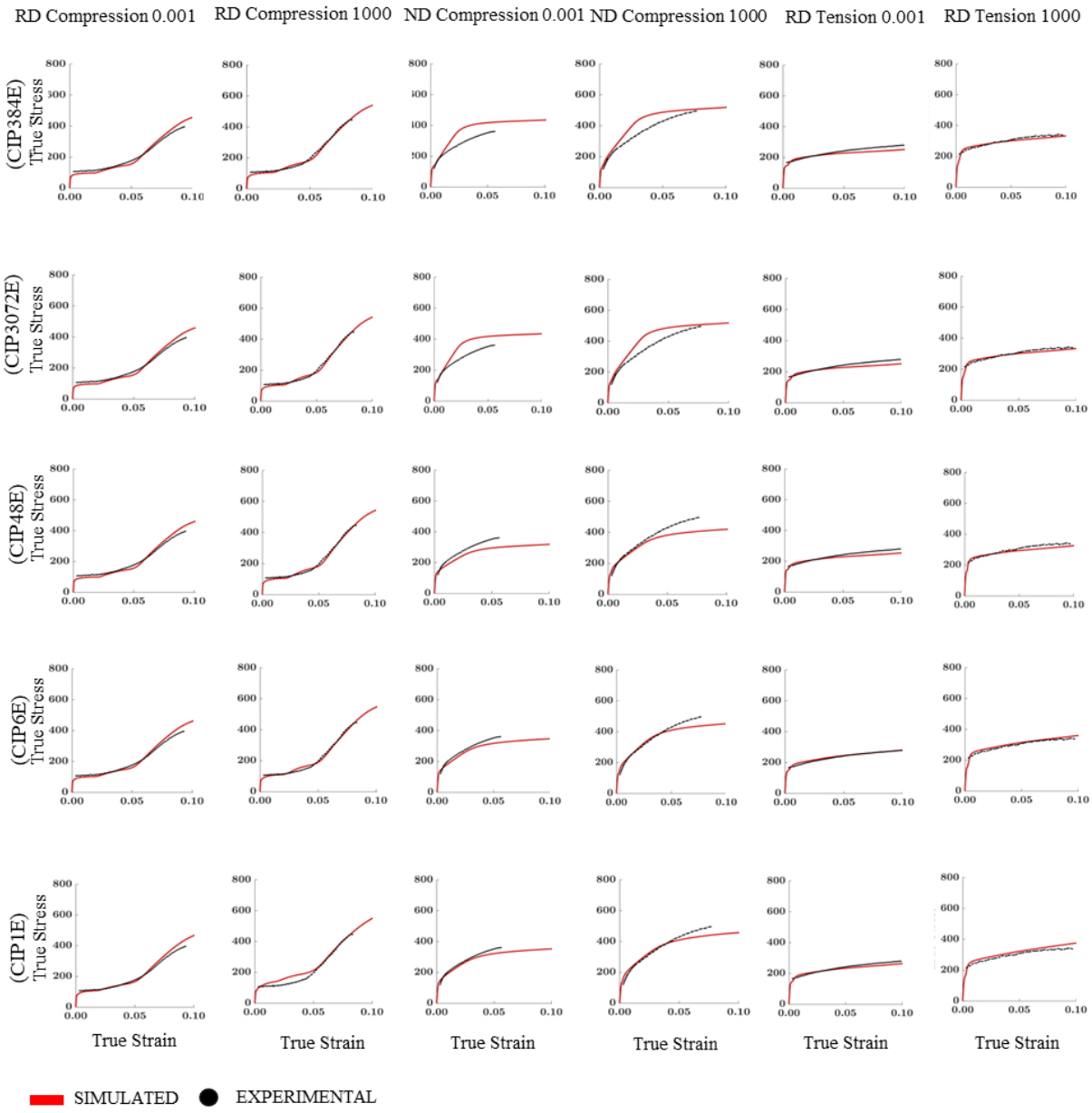

Figure 6. Comparison of simulated true stress-strain curves using the models from Fig. 2 and Table 2 as indicated in the figure and experimentally measured data.

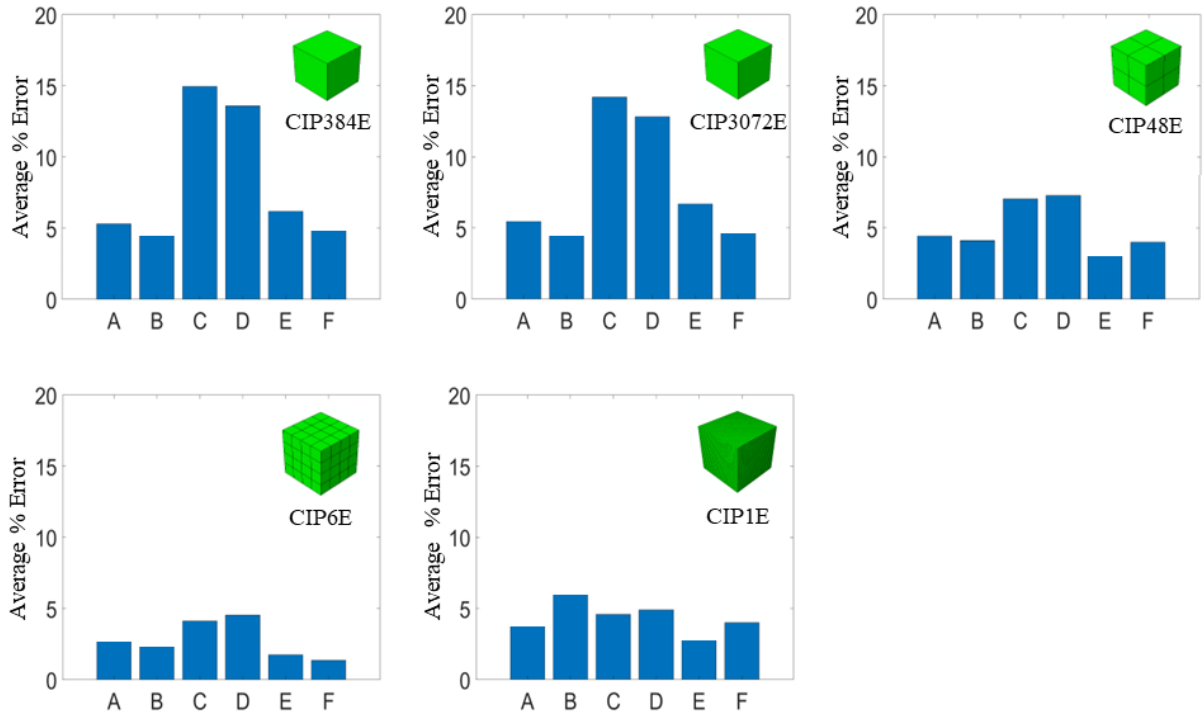

Figure 7. Average percent error in flow stress between the simulated and measured data from Fig. 6. The loading cases are labeled the same as in Fig. 4.

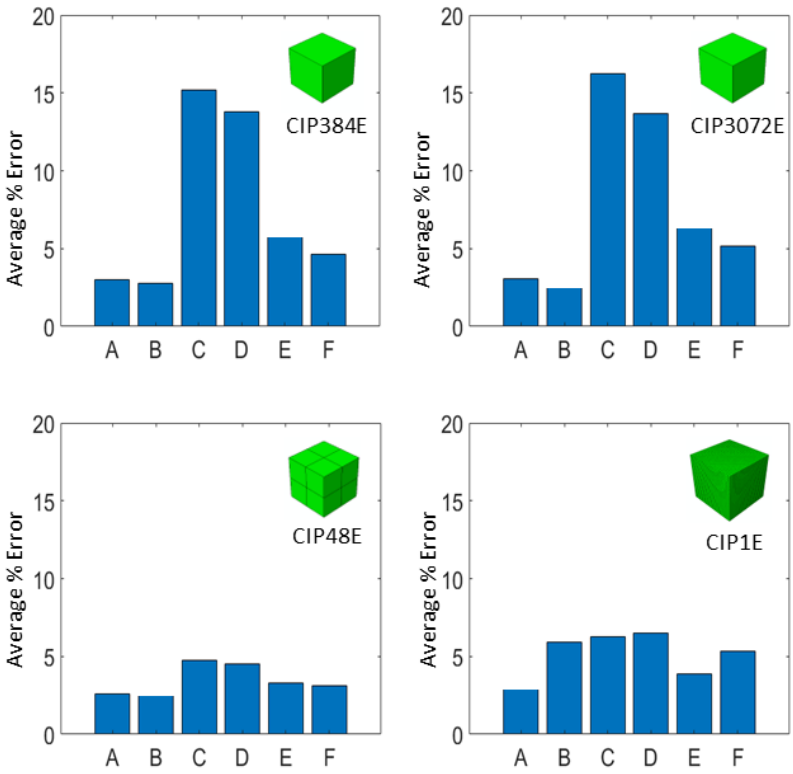

Figure 8. Average percent error in predicted flow stress between the models indicated in the figure and the CIP6E model from Fig. 6. The loading cases are labeled the same as in Fig. 4.

The relative activities of deformation mechanisms accommodating plastic deformation of Fig. 6 stress-strain curves are provided in the appendix. Some subtle differences in the activities are apparent. While the compression twinning activities at small strains are similar, the ratio of pyramidal c+a and basal slip are slightly different amongst the cases for the compressions in ND, which manifest in the stress-strain hardening response variations. The divergent behavior in ND is primarily for the CIP3072E and CIP384E models, while the CIP48E and CIP6E models exhibit similar activities. Moreover, there is a small shift in the twinning propensity and pyramidal slip in the case of RD compression using CIP1E, which is not present in other cases. Since the evolution

of texture is driven by the activities, only small variations in texture intensities are observed and are provided for completeness in the appendix.

5. Discussion

Infinitely rigid interactions (the Taylor-type constraint) between grains and their surrounding medium result in no fluctuations over the polycrystal mesh. The Taylor constraint assumption has been repeatedly shown to be suboptimal for plastically anisotropic material such as Mg alloys due to stiff and soft crystal directions requiring different interaction strengths with surrounding grains (Lebensohn and Tomé, 1993; Savage et al., 2020). The result of the rigid constraint is an increase in the flow stress due to pronounced activation of some slip systems at the expense of others. To model flow stress, the slip resistances must be unrealistically adjusted to suppress over activation of e.g. pyramidal slip systems (Knezevic et al., 2013a; Wu et al., 2008). This is not an issue just limited to Taylor polycrystals or Mg alloys. Self-consistent models also suffer from linearization assumptions and have led to the relative directional compliance formulation of (Barrett et al., 2020; Tomé, 1999) which dynamically adjusts interaction strength based on the amount of soft and hard crystals in a polycrystal. Full-field models are an alternative and are most appropriate to run when trying to understand and study fundamental information about a material; however, full-field models are computationally demanding and rely on explicit meshing of the grain structure. The large computational cost precludes part level FE simulations with full-field models. Moreover, limited tools for handling twin domains and phase transformations further make the full-field methods untenable for materials that deform through deformation twinning and phase transformations. The current work evaluates whether relaxation of the homogenization assumption

via finite elements is effective compared to full-field predictions for Mg alloys which exhibit strong anisotropic plasticity.

To evaluate the appropriateness of the stress and strain deviations per model compared to those of the CIP1-FF model, deviations in von Mises stress and effective strain over the FE meshes of Table 1 are computed and presented in Figs. 9 and 10, respectively. A vector of normalized deviations for stress is evaluated using

$$\Delta\bar{\sigma}^k = \frac{\sqrt{(\boldsymbol{\sigma}^k - \overline{\boldsymbol{\sigma}})\cdot(\boldsymbol{\sigma}^k - \overline{\boldsymbol{\sigma}})}}{\sqrt{\frac{3}{2}\bar{\mathbf{s}}\cdot\bar{\mathbf{s}}}} \text{ with } \bar{\mathbf{s}} = \overline{\boldsymbol{\sigma}} - \frac{tr(\overline{\boldsymbol{\sigma}})}{3}\mathbf{I} \tag{12}$$

where $\boldsymbol{\sigma}^k$ is stress at an IP k, $\overline{\boldsymbol{\sigma}}$ is average stress, and $\bar{\mathbf{s}}$ is deviatoric stress. An equivalent equation to Eq (12) is used to calculate the deviations in effective strain. For a single element there is no deviation in stress and strain. As the number of elements increase the number of crystals per integration point decrease. We see for CIP6 the best performance in position, breadth, and height of the distribution compared to the CIP1-FF. As mentioned in section 4.1, the poor performance of the CIP1 model stems from heterogeneity in the mesh which is not present in the CIP1-FF model due to the present of grain domains. These heterogeneities manifest themselves in both Figs. 9 and 10 as even multi model stress and strain distributions. It is worth noting for some cases CIP9 has more similar strain and stress deviations compared to CIP6 when compared to CIP1-FF. It is apparent that CIP3 is too few grains per integration point resulting with overestimation of the deviations and CIP48 is too many resulting in underestimation of the deviations. Running 3, 6, 9, and 48 crystals per integration point with a same large mesh to rule out any mesh size effect yields no appreciably different deviations to these shown here.

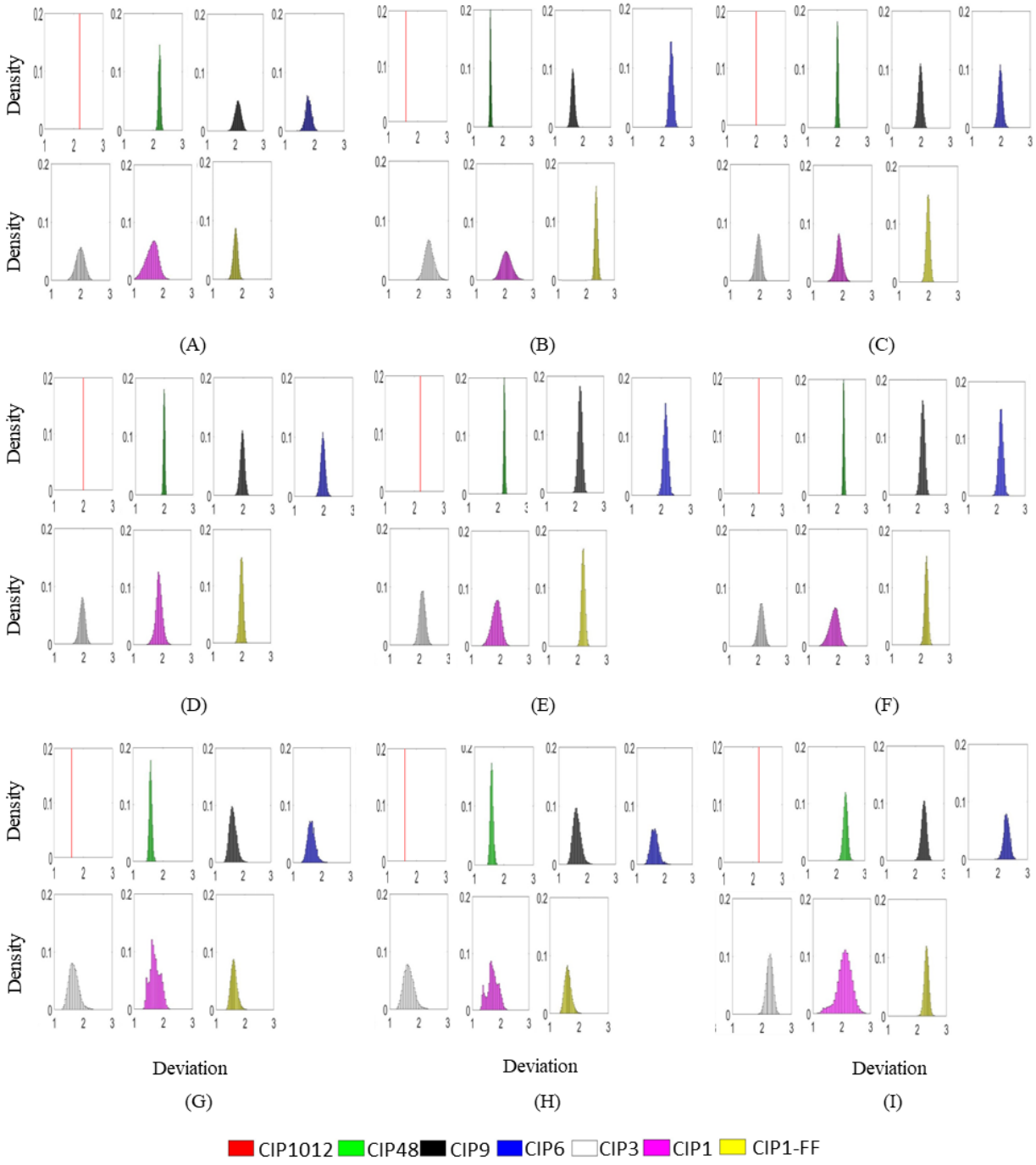

Figure 9. Histograms of von Mises stress deviation at 2% true strain after the loadings as in Fig. 4.

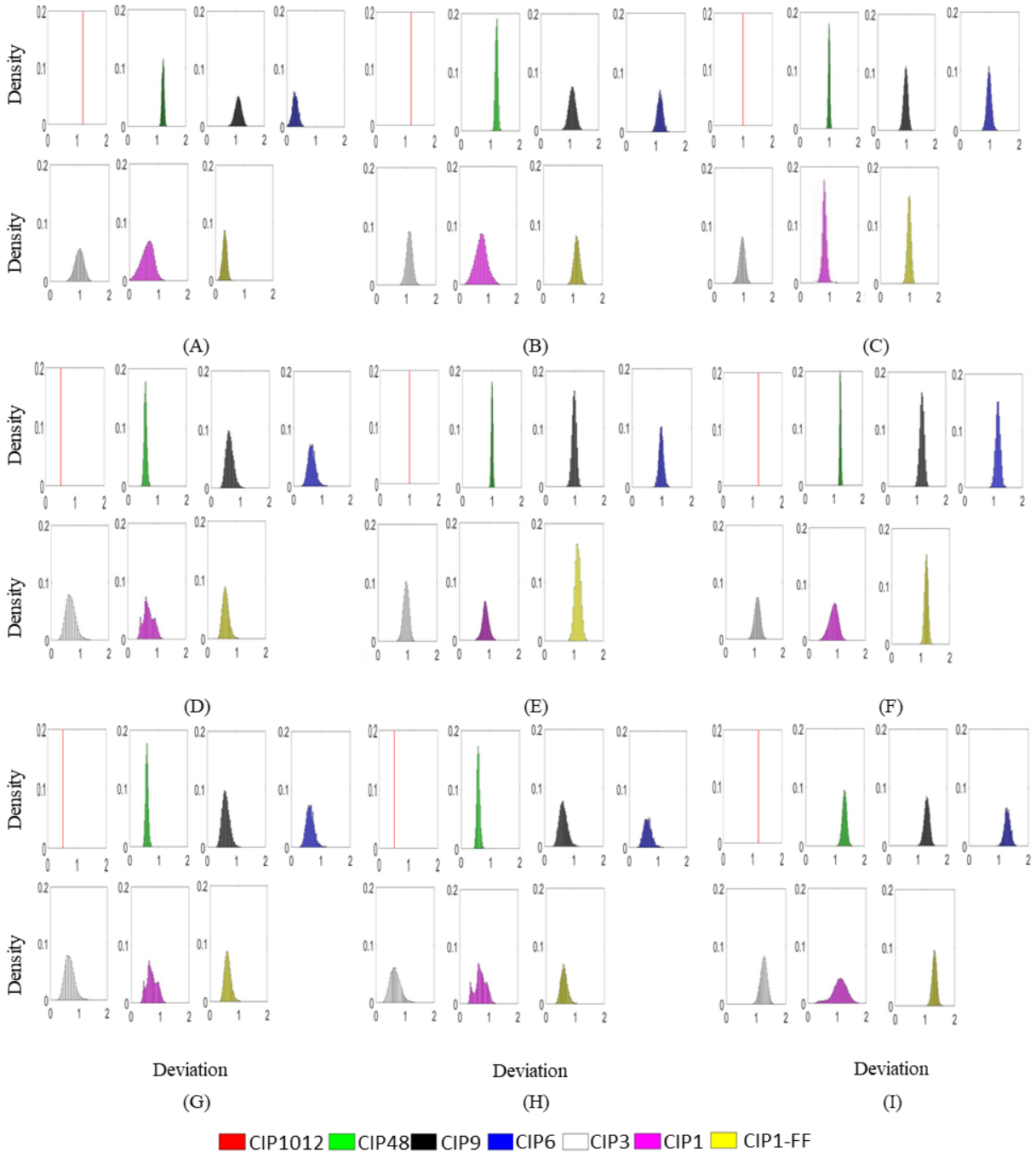

Figure 10. Histograms of logarithmic strain deviation at 2% true strain after the loadings as in Fig. 4.

The results of section 4 and the deviation plots in Figs. 9 and 10 suggest a relaxed Taylor model can be identified for Mg AZ31 alloys such that stress and strain deviation when compared to a full-field model are similar. The methodology for evaluating stress distributions here can be applied to evaluate whether the relaxed constraints are suitable for other plastically anisotropic materials. For AZ31, when six crystals are embedded per FE IP, the relaxed methodology facilitates the closest response to a full field polycrystalline grain model for both CIP6E 64 element and CIP6 2028 element models. Therefore, the performance of the six crystals per IP is established to be a sweet spot in smoothing local deformation while allowing heterogenous deformation over the mesh. Including more or less crystals per IP degrades the similarity. The worst performing configuration was one crystal per IP. The methodology presented here can be generalized to other homogenization methodologies such as SC or Sachs homogenizations in the FE frameworks. For the AZ31 material studied in this work a tradeoff is possible between homogenization artifacts and a continuum response at the Taylor polycrystal level that can be traded to optimize computational efficiency in bridging mesoscale to the macroscale. Embedding six crystals per IP is favorable for computationally tractable part level simulations of Mg alloys.

6. Conclusion

In this work, the deviation of progressive relaxation of the Taylor-type constraint assumption from a full-field polycrystalline grain structure simulation is determined for a plastically anisotropic polycrystal of Mg alloy AZ31. We established that the relaxation with six crystals per integration gave the best mechanical field comparison to the full-field model for AZ31, having the most similarities between stress-strain curves, deformation mode activities, and stress-strain deviations when compared with the full field model. We found that one crystal per integration point without

explicit grain structure performs poorly due to excessive heterogeneity resulting from the absence of coherent deformation domains. The parametric study conducted here demonstrated a methodology for identifying an appropriate relaxed Taylor-type model. The methodology could be employed to evaluate other homogenization scheme in a FE framework when plasticity is anisotropic and affected by homogenization assumptions. Using this approach, one can identify tradeoffs in model fidelity at the expense of time and compute resources. In addition, the work confirmed that homogenizations schemes like Taylor or more involved SC could be adopted to ease the complexity of full-field simulations in finite elements.

Acknowledgements

This research was performed under the CAREER Grant No. CMMI-1650641 sponsored by the U.S. National Science Foundation. D.J.S. gratefully acknowledges the Seaborg Institute for financial support under a post-doctoral fellowship through the Los Alamos National Laboratory LDRD program.

Appendix A

This appendix presents predicted activities of deformation modes (Fig. A1) and texture evolution (Fig. A2) for deformation cases presented in Fig. 6.

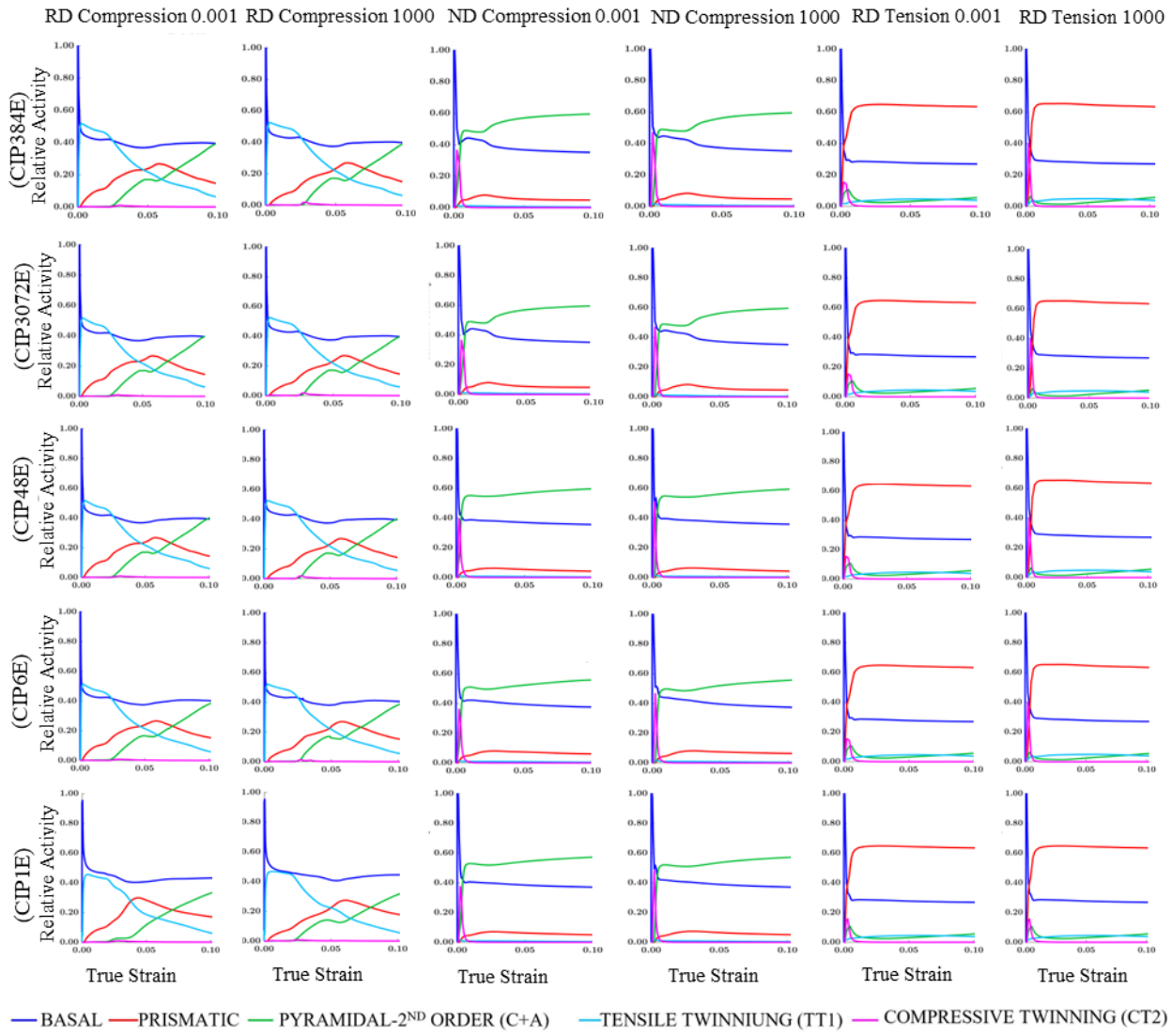

Figure A1. Relative activities of deformation modes predicted during the simulations presented in Fig. 6 using the models indicated in the figure.

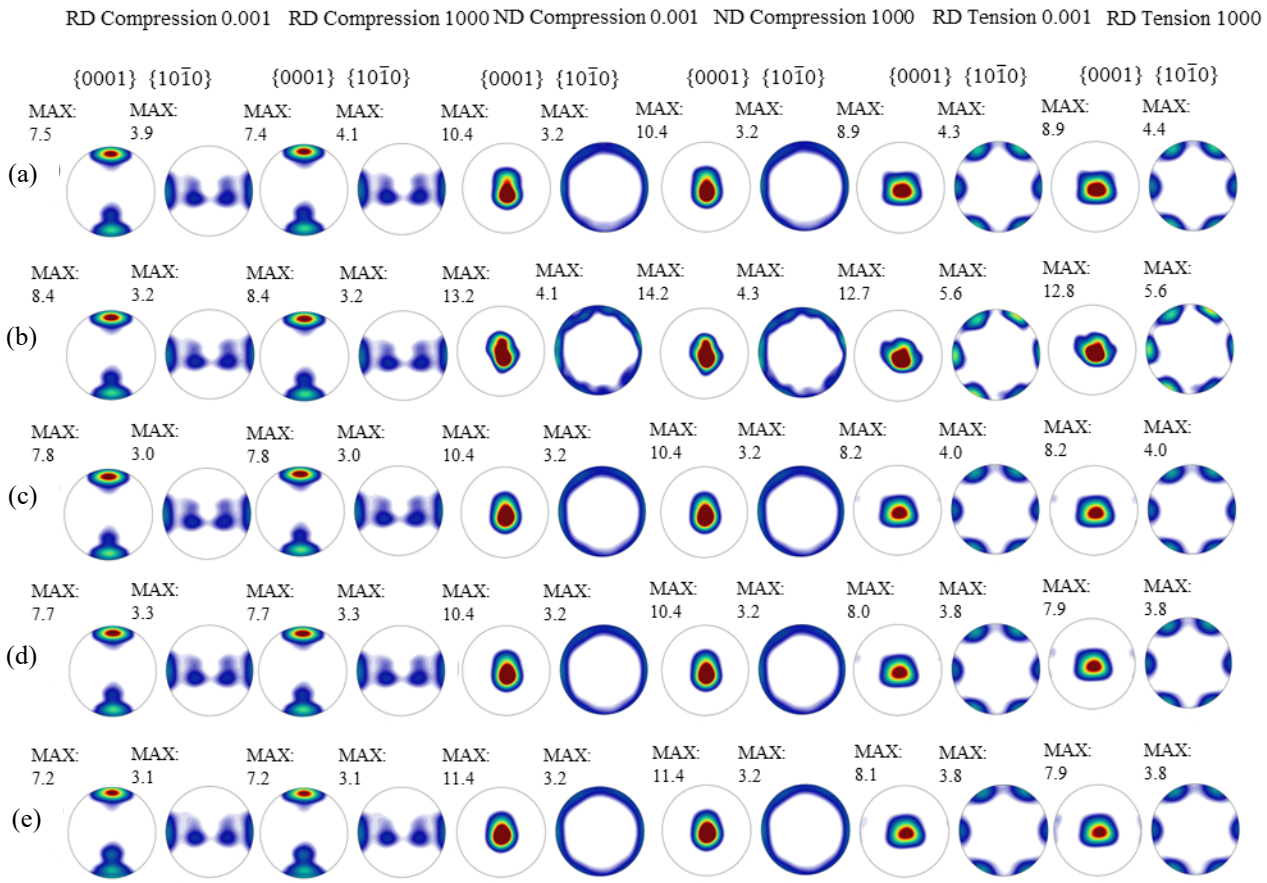

Figure A2. Pole figures showing texture predicted at a true strain of 0.1 for the loading directions and strain rates as in Fig. 6: (a) 1 element 384 crystals, (b) 1 element 3072 crystals, (c) 8 elements 48 crystals, (d) 64 elements 6 crystals, and (e) 13824 elements 1 crystal. The sample frame and intensity bar are the same as in Fig. 3.

References

Abdolvand, H., Majkut, M., Oddershede, J., Wright, J.P., Daymond, M.R., 2015. Study of 3-D stress development in parent and twin pairs of a hexagonal close-packed polycrystal: Part I – in-situ three-dimensional synchrotron X-ray diffraction measurement. Acta. Mater. 93, 246-255.

Ardeljan, M., Beyerlein, I.J., McWilliams, B.A., Knezevic, M., 2016. Strain rate and temperature sensitive multi-level crystal plasticity model for large plastic deformation behavior: Application to AZ31 magnesium alloy. Int. J. Plast. 83, 90-109.

Ardeljan, M., McCabe, R.J., Beyerlein, I.J., Knezevic, M., 2015. Explicit incorporation of deformation twins into crystal plasticity finite element models. Computer Methods in Applied Mechanics and Engineering 295, 396-413.

Asaro, R.J., Needleman, A., 1985. Texture development and strain hardening in rate dependent polycrystals. Acta Metall. Mater. 33, 923-953.

Barrett, T.J., McCabe, R.J., Brown, D.W., Clausen, B., Vogel, S.C., Knezevic, M., 2020. Predicting deformation behavior of α-uranium during tension, compression, load reversal, rolling, and sheet forming using elasto-plastic, multi-level crystal plasticity coupled with finite elements. J. Mech. Phys. Solids 138, 103924.

Barrett, T.J., Savage, D.J., Ardeljan, M., Knezevic, M., 2018. An automated procedure for geometry creation and finite element mesh generation: Application to explicit grain structure models and machining distortion. Comput. Mater. Sci. 141, 269-281.

Cheng, J., Ghosh, S., 2017. Crystal plasticity finite element modeling of discrete twin evolution in polycrystalline magnesium. J. Mech. Phys. Solids 99, 512-538.

Cho, K., Sano, T., Doherty, K., Yen, C., Gazonas, G., Montgomery, J., Moy, P., Davis, B., DeLorme, R., 2009. Magnesium technology and manufacturing for ultra lightweight armored ground vehicles. DTIC Document.

Cocke, C.K., Rollett, A.D., Lebensohn, R.A., Spear, A.D., 2021. The AFRL Additive Manufacturing Modeling Challenge: Predicting Micromechanical Fields in AM IN625 Using

an FFT-Based Method with Direct Input from a 3D Microstructural Image. Integrating Materials and Manufacturing Innovation 10, 157-176.

Diard, O., Leclercq, S., Rousselier, G., Cailletaud, G., 2002. Distribution of normal stress at grain boundaries in multicrystals: application to an intergranular damage modeling. Comput. Mater. Sci. 25, 73-84.

Duvvuru, H.K., Knezevic, M., Mishra, R.K., Kalidindi, S.R., 2007. Application of microstructure sensitive design to FCC polycrystals. Materials science forum 546, 675-680.

Eghtesad, A., Barrett, T.J., Knezevic, M., 2018. Compact reconstruction of orientation distributions using generalized spherical harmonics to advance large-scale crystal plasticity modeling: Verification using cubic, hexagonal, and orthorhombic polycrystals. Acta. Mater. 155, 418-432.

Eghtesad, A., Zecevic, M., Lebensohn, R.A., McCabe, R.J., Knezevic, M., 2017. Spectral database constitutive representation within a spectral micromechanical solver for computationally efficient polycrystal plasticity modelling. Comput. Mech., 1-16.

Eisenlohr, P., Tjahjanto, D.D., Hochrainer, T., Roters, F., Raabe, D., 2009. Comparison of texture evolution in fcc metals predicted by various grain cluster homogenization schemes. International Journal of Materials Research 100, 500-509.

Engler, O., Crumbach, M., Li, S., 2005. Alloy-dependent rolling texture simulation of aluminium alloys with a grain-interaction model. Acta. Mater. 53, 2241-2257.

Erinosho, T.O., Collins, D.M., Wilkinson, A.J., Todd, R.I., Dunne, F.P.E., 2016. Assessment of X-ray diffraction and crystal plasticity lattice strain evolutions under biaxial loading. Int. J. Plast. 83, 1-18.

Feather, W., Lim, H., Knezevic, M., 2021a. A numerical study into element type and mesh resolution for crystal plasticity finite element modeling of explicit grain structures. Computational Mechanics 67, 1-23.

Feather, W.G., Ghorbanpour, S., Savage, D.J., Ardeljan, M., Jahedi, M., McWilliams, B.A., Gupta, N., Xiang, C., Vogel, S.C., Knezevic, M., 2019. Mechanical response, twinning, and texture evolution of WE43 magnesium-rare earth alloy as a function of strain rate: Experiments and multi-level crystal plasticity modeling. Int. J. Plast. 120, 180-204.

Feather, W.G., Savage, D.J., Knezevic, M., 2021b. A crystal plasticity finite element model embedding strain-rate sensitivities inherent to deformation mechanisms: Application to alloy AZ31. Int. J. Plast. 143, 103031.

Feng, Z., Pokharel, R., Vogel, S.C., Lebensohn, R.A., Pagan, D., Zepeda-Alarcon, E., Clausen, B., Martinez, R., Gray, G.T., Knezevic, M., 2022. Crystal plasticity modeling of strain-induced martensitic transformations to predict strain rate and temperature sensitive behavior of 304 L steels: Applications to tension, compression, torsion, and impact. Int. J. Plast. 156, 103367.

Ferreri, N.C., Feng, Z., Savage, D.J., Brown, D.W., Clausen, B., Sisneros, T.A., Knezevic, M., 2022. In-situ high-energy X-ray diffraction and crystal plasticity modeling to predict the evolution of texture, twinning, lattice strains and strength during loading and reloading of beryllium. Int. J. Plast. 150, 103217.

Follansbee, P., Kocks, U., 1988. A constitutive description of the deformation of copper based on the use of the mechanical threshold stress as an internal state variable. Acta Metall. 36, 81-93.

Groeber, M.A., Jackson, M.A., 2014. DREAM. 3D: A digital representation environment for the analysis of microstructure in 3D. Integrating Materials and Manufacturing Innovation 3, 5.

Hartley, C.S., Dawson, P.R., Boyce, D.E., Kalidindi, S.R., Knezevic, M., Tomé, C., Lebensohn, R., Semiatin, S.L., Turner, T.J., Salem, A.A., 2008. A comparison of deformation textures and mechanical properties predicted by different crystal plasticity codes. AIR FORCE RESEARCH LAB WRIGHT-PATTERSON AFB OH MATERIALS AND MANUFACTURING ….

Hutchinson, J.W., 1976. Bounds and self-consistent estimates for creep of polycrystalline materials. Proceedings of the Royal Society of London. Series A, Mathematical and Physical Sciences 348, 101-126.

Jahedi, M., Ardeljan, M., Beyerlein, I.J., Paydar, M.H., Knezevic, M., 2015. Enhancement of orientation gradients during simple shear deformation by application of simple compression. J. Appl. Phys. 117, 214309.

Kalidindi, S.R., 1998. Incorporation of deformation twinning in crystal plasticity models. J. Mech. Phys. Solids 46, 267-271.

Kalidindi, S.R., Bronkhorst, C.A., Anand, L., 1992. Crystallographic texture evolution in bulk deformation processing of FCC metals. J. Mech. Phys. Solids 40, 537-569.

Keshavarz, S., Ghosh, S., 2015. Hierarchical crystal plasticity FE model for nickel-based superalloys: Sub-grain microstructures to polycrystalline aggregates. International Journal of Solids and Structures 55, 17-31.

Knezevic, M., Daymond, M.R., Beyerlein, I.J., 2016a. Modeling discrete twin lamellae in a microstructural framework. Scr. Mater. 121, 84-88.

Knezevic, M., Kalidindi, S.R., 2007. Fast computation of first-order elastic-plastic closures for polycrystalline cubic-orthorhombic microstructures. Comput. Mater. Sci. 39, 643-648.

Knezevic, M., Kalidindi, S.R., Fullwood, D., 2008. Computationally efficient database and spectral interpolation for fully plastic Taylor-type crystal plasticity calculations of face-centered cubic polycrystals. Int. J. Plast. 24, 1264-1276.

Knezevic, M., Lebensohn, R.A., Cazacu, O., Revil-Baudard, B., Proust, G., Vogel, S.C., Nixon, M.E., 2013a. Modeling bending of α-titanium with embedded polycrystal plasticity in implicit finite elements. Mater. Sci. Eng. A 564, 116-126.

Knezevic, M., McCabe, R.J., Lebensohn, R.A., Tomé, C.N., Liu, C., Lovato, M.L., Mihaila, B., 2013b. Integration of self-consistent polycrystal plasticity with dislocation density based hardening laws within an implicit finite element framework: Application to low-symmetry metals. J. Mech. Phys. Solids 61, 2034-2046.

Knezevic, M., Savage, D.J., 2014. A high-performance computational framework for fast crystal plasticity simulations. Comput. Mater. Sci. 83, 101-106.

Knezevic, M., Zecevic, M., Beyerlein, I.J., Lebensohn, R.A., 2016b. A numerical procedure enabling accurate descriptions of strain rate-sensitive flow of polycrystals within crystal visco-plasticity theory. Computer Methods in Applied Mechanics and Engineering 308, 468-482.

Kocks, U., Argon, A., Ashby, M., 1975. Thermodynamics and Kinetics of Slip. Prog. Mater. Sci. 19, 110-170.

Kocks, U.F., Tomé, C.N., Wenk, H.-R., 1998. Texture and Anisotropy. Cambridge University Press, Cambridge, UK.

Kurukuri, S., Worswick, M.J., Ghaffari Tari, D., Mishra, R.K., Carter, J.T., 2014. Rate sensitivity and tension–compression asymmetry in AZ31B magnesium alloy sheet. Philosophical Transactions of the Royal Society A: Mathematical, Physical and Engineering Sciences 372, 20130216.

Landry, N., Knezevic, M., 2015. Delineation of First-Order Elastic Property Closures for Hexagonal Metals Using Fast Fourier Transforms. Materials 8, 6326-6345.

Lebensohn, R., 2001. N-site modeling of a 3D viscoplastic polycrystal using fast Fourier transform. Acta. Mater. 49, 2723-2737.

Lebensohn, R.A., Brenner, R., Castelnau, O., Rollett, A.D., 2008. Orientation image-based micromechanical modelling of subgrain texture evolution in polycrystalline copper. Acta. Mater. 56, 3914-3926.

Lebensohn, R.A., Kanjarla, A.K., Eisenlohr, P., 2012. An elasto-viscoplastic formulation based on fast Fourier transforms for the prediction of micromechanical fields in polycrystalline materials. International Journal of Plasticity 32–33, 59-69.

Lebensohn, R.A., Tomé, C.N., 1993. A self-consistent anisotropic approach for the simulation of plastic deformation and texture development of polycrystals: Application to zirconium alloys. Acta Metall. Mater. 41, 2611-2624.

Lim, H., Carroll, J.D., Battaile, C.C., Buchheit, T.E., Boyce, B.L., Weinberger, C.R., 2014. Grain-scale experimental validation of crystal plasticity finite element simulations of tantalum oligocrystals. Int. J. Plast. 60, 1-18.

Liu, B., Raabe, D., Roters, F., Eisenlohr, P., Lebensohn, R.A., 2010. Comparison of finite element and fast Fourier transform crystal plasticity solvers for texture prediction. Modelling and Simulation in Materials Science and Engineering 18, 085005.

Lou, X.Y., Li, M., Boger, R.K., Agnew, S.R., Wagoner, R.H., 2007. Hardening evolution of AZ31B Mg sheet. Int. J. Plast. 23, 44-86.

Mordike, B.L., Ebert, T., 2001. Magnesium: Properties - applications - potential. Mater. Sci. Eng. A 302, 37-45.

Naragani, D., Shade, P., Musinski, W., Boyce, D., Obstalecki, M., Pagan, D., Bernier, J., Beaudoin, A., 2021. Interpretation of intragranular strain fields in high-energy synchrotron X-ray experiments via finite element simulations and analysis of incompatible deformation. Mater. Des. 210, 110053.

Peirce, D., Asaro, R.J., Needleman, A., 1982. An analysis of nonuniform and localized deformation in ductile single crystals. Acta Metall. 30, 1087-1119.

Proust, G., Tomé, C.N., Kaschner, G.C., 2007. Modeling texture, twinning and hardening evolution during deformation of hexagonal materials. Acta. Mater. 55, 2137-2148.

Riyad, I.A., McWilliams, B.A., Pramanik, B., Knezevic, M., 2023. Correlated structure viscoplastic self-consistent polycrystal plasticity: Application to modeling strain rate sensitive deformation of Ti-6Al-4 V. Int. J. Plast. 163, 103571.

Roters, F., Eisenlohr, P., Hantcherli, L., Tjahjanto, D.D., Bieler, T.R., Raabe, D., 2010. Overview of constitutive laws, kinematics, homogenization and multiscale methods in crystal plasticity finite-element modeling: Theory, experiments, applications. Acta. Mater. 58, 1152-1211.

Savage, D.J., Beyerlein, I.J., Mara, N.A., Vogel, S.C., McCabe, R.J., Knezevic, M., 2020. Microstructure and texture evolution in Mg/Nb layered materials made by accumulative roll bonding. Int. J. Plast. 125, 1-26.

Segurado, J., Lebensohn, R.A., Llorca, J., Tomé, C.N., 2012. Multiscale modeling of plasticity based on embedding the viscoplastic self-consistent formulation in implicit finite elements. Int. J. Plast. 28, 124-140.

Slutsky, L.J., Garland, C.W., 1957. Elastic Constants of Magnesium from 4.2 K to 300 K. Physical Review 107, 972-976.

Tam, K.J., Vaughan, M.W., Shen, L., Knezevic, M., Karaman, I., Proust, G., 2021. Modelling dynamic recrystallisation in magnesium alloy AZ31. Int. J. Plast. 142, 102995.

Taylor, G.I., 1938. Plastic strain in metals. Journal of the Institute of Metals 62, 307-324.

Tjahjanto, D.D., Eisenlohr, P., Roters, F., 2015. Multiscale deep drawing analysis of dual-phase steels using grain cluster-based RGC scheme. Modelling and Simulation in Materials Science and Engineering 23, 045005.

Tomé, C.N., 1999. Self-consistent polycrystal models: A directional compliance criterion to describe grain interactions. Modelling and Simulation in Materials Science and Engineering 7, 723-738.

Tomé, C.N., Lebensohn, R.A., Kocks, U.F., 1991. A model for texture development dominated by deformation twinning: Application to zirconium alloys. Acta Metall. Mater. 39, 2667-2680.

Van Houtte, P., 1978. Simulation of the rolling and shear texture of brass by the Taylor theory adapted for mechanical twinning. Acta Metall. Mater. 26, 591-604.

Van Houtte, P., Delannay, L., Kalidindi, S.R., 2002. Comparison of two grain interaction models for polycrystal plasticity and deformation texture prediction. Int. J. Plast. 18, 359-377.

Van Houtte, P., Delannay, L., Samajdar, I., 1999. Quantitative prediction of cold rolling textures in low-carbon steel by means of the LAMEL model. Textures and Microstructures 31, 109-149.

Van Houtte, P., Li, S., Seefeldt, M., Delannay, L., 2005. Deformation texture prediction: from the Taylor model to the advanced Lamel model. Int. J. Plast. 21, 589-624.

Wu, X., Kalidindi, S.R., Necker, C., Salem, A.A., 2008. Modeling anisotropic stress-strain response and crystallographic texture evolution in α-titanium during large plastic deformation

using Taylor-type models: Influence of initial texture and purity. Metall. Mater. Trans. A 39A, 3046-3054.

Zecevic, M., Beyerlein, I.J., Knezevic, M., 2017. Coupling elasto-plastic self-consistent crystal plasticity and implicit finite elements: Applications to compression, cyclic tension-compression, and bending to large strains. Int. J. Plast. 93, 187-211.

Zecevic, M., Beyerlein, I.J., McCabe, R.J., McWilliams, B.A., Knezevic, M., 2016. Transitioning rate sensitivities across multiple length scales: Microstructure-property relationships in the Taylor cylinder impact test on zirconium. Int. J. Plast. 84, 138-159.

Zecevic, M., Knezevic, M., 2017. Modeling of Sheet Metal Forming Based on Implicit Embedding of the Elasto-Plastic Self-Consistent Formulation in Shell Elements: Application to Cup Drawing of AA6022-T4. JOM 69, 922-929.

Zecevic, M., Knezevic, M., 2018. A new visco-plastic self-consistent formulation implicit in dislocation-based hardening within implicit finite elements: Application to high strain rate and impact deformation of tantalum. Computer Methods in Applied Mechanics and Engineering 341, 888-916.

Zecevic, M., McCabe, R.J., Knezevic, M., 2015. A new implementation of the spectral crystal plasticity framework in implicit finite elements. Mechanics of Materials 84, 114-126.

Zhao, Z., Ramesh, M., Raabe, D., Cuitiño, A.M., Radovitzky, R., 2008. Investigation of three-dimensional aspects of grain-scale plastic surface deformation of an aluminum oligocrystal. Int. J. Plast. 24, 2278-2297.

Chapter 3: Assessing strength of phases in a quadruplex high entropy alloy via high-throughput nanoindentation to clarify origins of strain hardening

This chapter has been submitted to Materials Characterization journal on April 25th, 2023.

My contribution to this work was material preparation, EBSD imaging, all nanoindentation data acquisition, analysis, and figures. Correlated phase transformation and hardness parameters were obtained by myself. Evgenii Vasilev also took some EBSD and tested tensile specimens. The original first draft was written by myself and further written in a standard student-mentor relationship.

Assessing strength of phases in a quadruplex high entropy alloy via high-throughput nanoindentation to clarify origins of strain hardening

Jacob Weiss, Evgenii Vasilev, Marko Knezevic*

Department of Mechanical Engineering, University of New Hampshire, Durham, NH 03824, USA.

* Corresponding author at: University of New Hampshire, Department of Mechanical Engineering, 33 Academic Way, Kingsbury Hall, W119, Durham, New Hampshire 03824, United States. E-*mail address*: marko.knezevic@unh.edu (M. Knezevic).

Abstract

This paper describes the main findings from an experimental investigation into local and overall strength and fracture behavior of a microstructurally flexible, quadruplex, high entropy alloy (HEA), $Fe_{42}Mn_{28}Co_{10}Cr_{15}Si_5$ (in at%). The alloy consists of metastable face-centered cubic austenite (γ), stable hexagonal epsilon martensite (ε), stable body-centered cubic ferrite (α), and stable tetragonal sigma (σ) phases. The overall behavior of the alloy in compression features a great deal of plasticity and strain hardening before fracture. While the contents of diffusion created α and σ phases remain constant during deformation, the fraction of ε increases at the expanse of γ due to the diffusionless strain induced γ→ε phase transformation. High-throughput nanoindentation mapping is used to assess the mechanical hardness of individual phases

contributing to the plasticity and hardening of the alloy. Increasing the fraction of the dislocated ε phase during deformation due to the transformation is found to act as a secondary source of hardening because γ and ε exhibit similar hardness at a given strain level. While these two phases exhibit moderate hardening during plasticity, significant softening is observed in σ owing to the phase fragmentation. While the phase transformation mechanism facilitates accommodation of the plasticity, the primary source of strain hardening in the alloy is the refinement of the structure during the transformation inducing a dynamic Hall-Petch-type barrier effect. Results pertaining to the evolution of microstructure and local behavior of the alloy under compression are presented and discussed clarifying the origins of strain hardening. While good under compression, the alloy poorly behaves under tension. Fracture surfaces after tension feature brittle micromechanisms of fracture. Such behavior is attributed to the presence of the brittle σ phase.

Keywords: High entropy alloys; Phase transformations; Microstructures; Nanoindentation; Hardness maps

1. Introduction

A class of sophisticated metallic materials termed high entropy alloys (HEAs) are being developed to enhance the contrasting material properties of strength and ductility [1-3]. Beginning with equiatomic HEA like $Fe_{20}Mn_{20}Ni_{20}Co_{20}Cr_{20}$ which exhibits good strength, ductility, and fracture toughness, other variants of the Fe-Mn-Ni-Co-Cr systems like $Fe_{40}Mn_{27}Ni_{26}Co_5Cr_2$ (at. %) are being explored [4-8]. The chief advantage of HEAs is in their flexibility to tune microstructural features through adjusting their composition and processing. To this end, dual phase HEAs consisting of Fe-Mn-Co-Cr were developed. For example, an $Fe_{50}Mn_{30}Co_{10}Cr_{10}$ (at. %) system consists of a face-centered cubic (FCC) austenite (γ) phase, which is metastable. The phase undergoes strain-induced phase transformation into a dislocated hexagonal close-packed (HCP) epsilon-martensite phase (ε) while accommodating plastic strains [7, 9]. The mechanism is often referred to as the TRIP (transformation induced plasticity) since it accommodates plastic strains like dislocation slip. Because multi-phase, these HEAs offer flexibility to design volume fraction and distribution of phases to improve ductility and strength tradeoffs [4, 5, 7]. The distribution can be achieved by varying processing methodologies such as rolling, high pressure torsion, and friction stir processing [10-12]. Studies on increasing alloying elements such as Cr at the expense of Fe and Mn on γ phase in dual phase HEA have been reported in [13, 14]. Increasing the Cr content furthers the driving force of $\gamma \rightarrow \varepsilon$ transformation [10]. The present work is concerned with characterizing a $Fe_{42}Mn_{28}Co_{10}Cr_{15}Si_5$ (in at%) HEA designed to exhibit pronounced TRIP. The alloy has a quadruplex structure consisting of stable body-centered cubic ferrite (α) and stable tetragonal sigma (σ) phases in addition to metastable γ and stable ε. The particular focus of the work is to assess the strength of individual phases via

high-throughput nanoindentation and attempt to clarify origins of strain hardening during plastic deformation of the alloy.

Nanoindentation is conceived as a technique to measure and understand the localized mechanical properties of metallic materials including HEAs [15-17]. To date, hardness mapping has been utilized to explore spatial variations in a variety of metal alloys [18, 19]. However, only a handful of such experiments along with some atomistic simulations have been performed on nanoindentation of HEAs [20]. Atomistic simulations of nanoindentation of HEAs are challenging due to compositional complexities [21]. Nevertheless, such simulations were successful in revealing the effects of localized chemical composition changes on the mechanical properties of complex multicomponent HEAs [22-24]. Nanoindentation studies revealed the effects of single crystal crystallographic orientations on nanoindentation response and underlying defect structures [25]. Moreover, studies into the effects of twin boundaries on nanoindentation response and underlying dislocation activity found that the twin boundaries inhibit dislocation penetration through the analysis of the plastic zone underneath the indentation [26]. Another study analyzed the influences of alloy composition, crystal structure, grain size, and twin boundary distance on the nanoimprinted properties of several HEAs [27].

While various aspects of the mechanical response of HEA alloys under deformation by nanoindentation were investigated in the pre-mentioned studies, the role of local hardness in individual phases on strain hardening of multi-phase HEAs was not rationalized. Localized hardness mapping is a relatively new experimental technique that has been underutilized in only a few studies involving HEAs [28-30]. We subject a complex $Fe_{42}Mn_{28}Co_{10}Cr_{15}Si_5$ (in at%) HEA to nanoindentation over relatively large areas at varying strain levels to understand its hardening behavior more holistically. An experimental investigation into tailoring the content of phases and

grain structure for high strength of the alloy using rolling, friction stir processing, and compression was performed in our earlier study [10]. Hardness maps obtained over selected areas in the present study provide complementary insights into the mechanical properties of evolving HEA microstructural phases.

The evolution of microstructure was measured by optical microscopy, electron back scatter diffraction (EBSD), and neutron diffraction (NeD). The as-received material was a rolled plate having a quadruplex structure consisting of metastable γ, stable σ, stable ε, along with some stable α phases. The evolution of phase fractions and texture per phase was measured. Simple compression data was taken from [10], while simple tension testing of the alloy was performed in the present work. In addition to measuring the overall properties, localized hardness Young's modulus maps over increasing levels of strain are measured. To this end, instrumented indentation testing (IIT) with the KLA Nano Indenter® systems employing the Oliver-Pharr method is used to automatically determine the sought properties from the recorded load-displacement history throughout the experiment [31]. These maps are correlated with the EBSD maps over the same areas, given that the resolution, scan size, and sample preparation requirements between the nanoindentation and EBSD mappings are comparable, to elucidate the relative hardness of individual phases. The roles of transformation of phases and hardness per phase on hardening during compression are conveyed in this paper. These comprehensive results are presented as discussed as necessary for the development of crystal plasticity models able to partition strain accommodation by individual phases in complex high entropy alloys. Predicting overall mechanical performance of such alloys requires the guidance and validation in terms of phase specific mechanical properties.

2. Experimental Procedures

2.1 Material processing

The HEA rolled plate's composition studied in the present work was $Fe_{42}Mn_{28}Co_{10}Cr_{15}Si_5$ in atomic percent. The plate was manufactured at Sophisticated Alloys Inc. An ingot of 50.8 mm in thickness was cast and then heat treated at 1100℃ for two hours to achieve homogenization of the structure. After the heat treatment, the material was rolled into a plate 8.9 mm in thickness in multiple passes.

2.2 Mechanical testing

Wire electric discharge machining (EDM) was utilized to make specimens for compression testing, while tensile dog-bone specimens were machined using a lathe. Compression stress-strain data was taken from our earlier work [10]. Two additional cylindrical specimens 3 mm in diameter and 4.8 mm in height were deformed to 0.21 compressive strain and to fracture for microstructural characterization and nanoindentation. Tensile specimens were made with an axis in-plane (IP) aligned with the plate rolling direction (RD). The gauge section of the dog-bone specimens was 28 mm in length and 5 mm in diameter. An MTS biaxial servohydraulic machine of 250 kN capacity was used to perform the tensile tests at room temperature under a constant strain rate of 10^{-3}/s. An MTS 623.12E-24 extensometer was used to measure displacement. Three tensile tests were performed to fracture to ensure reputability of the results. The measured curves were on top of each other.

2.3 Microstructural characterization

Optical microscopy and EBSD using a scanning electron microscope (SEM) were used to determine and characterize the microstructure of the alloy. Optical images were taken using an Olympus OLS5000 microscope. The images were taken using either laser or visible light. EBSD was performed using a Tescan Lyra (Ga) field emission SEM. Scans were taken in field mode with a beam intensity (BI) of 20.05-20.07 at a voltage of 20kV. The working distance was set at 9 mm and the scans were conducted at 615 fps at a 16 x16 bin size. Multiple scans were taken for each strain level to ensure repeatability of the results. All scans contained over 600,000 points with a step size of 0.4 μm. Post processing of the data was performed using OIM analysis software package.

Samples from all strain levels were prepared by grinding with 320, 400, 600, 800, and 1200 grit SiC papers with 6lb force per sample till plane. Post grinding, the samples were polished with a TriDent mat using 3 μm diamond suspension at 150 rpm for 5 minutes, followed by a TriDent mat with 1 μm diamond suspension at 150 rpm for 5 minutes. Lastly, vibratory polishing with a 0.05 μm colloidal silica suspension for 12 hours was conducted to ensure preferable indexing and high confidence index (CI) on the EBSD scans. No etching was necessary after vibratory polishing.

Energy dispersive spectroscopy (EDS) was also completed to observe the elemental composition of phases that were present.

Finally, NeD was completed in Los Alamos Neutron Science Center at Los Alamos National Laboratory for a few specimens, initial and deformed in compression [10, 32]. Maud

software was used to analyze the experimental data to obtain orientation distributions. Pole figures were plotted in MTEX.

2.4 Nanoindentation

Nanoindentation is a tool for exploring mechanical behavior at small length scales [33]. The technique interrogates materials locally and is only semi-destructive, while allowing extraction of diverse properties including elastic and plastic. Nanoindentation was performed using a KLA Instruments iMicro Nano indenter with a Berkovich tip. Each specimen was initially marked in four corners with a large indentation before EBSD was taken. After EBSD, each specimen was placed into the nano indenter to measure harness maps in the same area as the EBSD scan took place. The technique results in correlated EBSD and nanoindentation mapping. Areas of 150 μm x 150 μm were always chosen for indenting inside each sample EBSD scan. Using Nanoblitz 3D, a built in KLA indenting function, 22,500 indents were placed in the 150x150 grid with a 1 μm spacing at a force of 750 μN per specimen. Hardness maps, Young's modulus, and correlated phase hardness maps were produced using KLA's post processing software.

The process of NanoBlitz 3D nanoindentation involves forcing the Berkovich tip into the surface of an investigated material. An indentation load (P) is applied as a constant while the resulting indentation depth and contact stiffness are continuously recorded by the instrument. The measured values per indent are then converted into elastic modulus and hardness through the Oliver-Pharr indentation equations [31]. To this end, the analysis of the load and displacement by the instrument yields a contact penetration depth (h_c) and corresponding contact area ($A_c =$

$\hat{A}_c(h_c)$) per indent to obtain Young's modulus ($E_{IIT} = (1 - v_s^2)\left[\frac{2}{S}\sqrt{\frac{A_c}{\pi}} - \frac{1-v_i^2}{E_i}\right]$) and hardness ($H_{IIT} = \frac{P_{max}}{A_c}$), where subscripts *i* and *s* correspond to indented and sample. *S* is beginning of the unloading slope. The obtained hardness relating the force on the indenter to the projected contact area per indent is referred to as instrumented indentation testing (IIT) hardness. IIT is sometimes called high speed nanoindentation or high throughput nanoindentation. Evidently, IIT determines material properties without the need to measure the contact area upon where the indenter is withdrawn from the material. Knowing the contact depth over which the probe contacts the material, the contact area, A_c, can be calculated through an area function, $\hat{A}_c(h_c)$. The function is dependent on the geometry of the probe. For the Berkovich tip indenter, which is a three-sided pyramid made of diamond, the function is: $A_c = 24.56h_c^2 + Ch_c$ with C = 150 nm.

Vickers (or Knoop) hardness (HV) can also be obtained by using the mean contact area or Meyer hardness conversion through the KLA iMicro indenter software using: $\text{HV} = 94.52 \cdot H_{IIT}$. In contrast to HV governed by ISO 6507 and ASTM E384, IIT governed by ISO 14577 and ASTM E2546 is fast (~1 second per indent). Standard HV relies on a 4-sided Vickers pyramid to obtain one value of hardness at a single force and penetration depth. HV hardness is a ratio of an applied load (kg) to the surface contact area between the indenter and the sample. In contrast, IIT uses a 3-sided Berkovich pyramid probe. Young's modulus and hardness maps are obtained effectively and can be analyzed statistically. IIT is a technique developed for performing large numbers of indentations in short periods of time. Indents are performed over a user defined grid.

To produce high quality property maps over a user defined grid, the considerations of load level and resulting indentation depth, stress fields, and underlying elastic and plastic zones underneath the indenter are important. While the entire elastic zone is sufficient for the modulus

measurements, the elastic–plastic deformation zone is required for the hardness measurements. The fields from neighboring indents should not overlap. Therefore, consideration of grid resolution is also important and needs to be carefully defined. We have explored multiple grids while establishing appropriate in-plane indentation spacing between indents to obtain high quality maps presented in the results section of the paper.

3. Results

3.1 Mechanical testing for overall properties

True stress – true strain curves are recorded during compression along the through-thickness (TT)/ND and in-plane (IP)/RD and in tension along RD for the as rolled materials (Fig. 1). As observable, the specimen in IP condition exhibits larger amounts of ductility. The material is approximately isotropic and can accumulate more compressive strain in IP than in TT. The ultimate strength between IP and TT samples are alike, where IP is slightly higher at 1300 MPa while TT has an ultimate strength of 1250 MPa. The material in tension has a yield stress of about 300 MPa and an ultimate tensile strength (UTS) of 520 MPa. The material exhibits poor ductility. To justify the strength and hardening behavior of the material undergoing substantial phase transformation during deformation, microscopy, and nanoindentation characterizations were carried out for establishing phase-hardness correlations, as presented in the following sections.

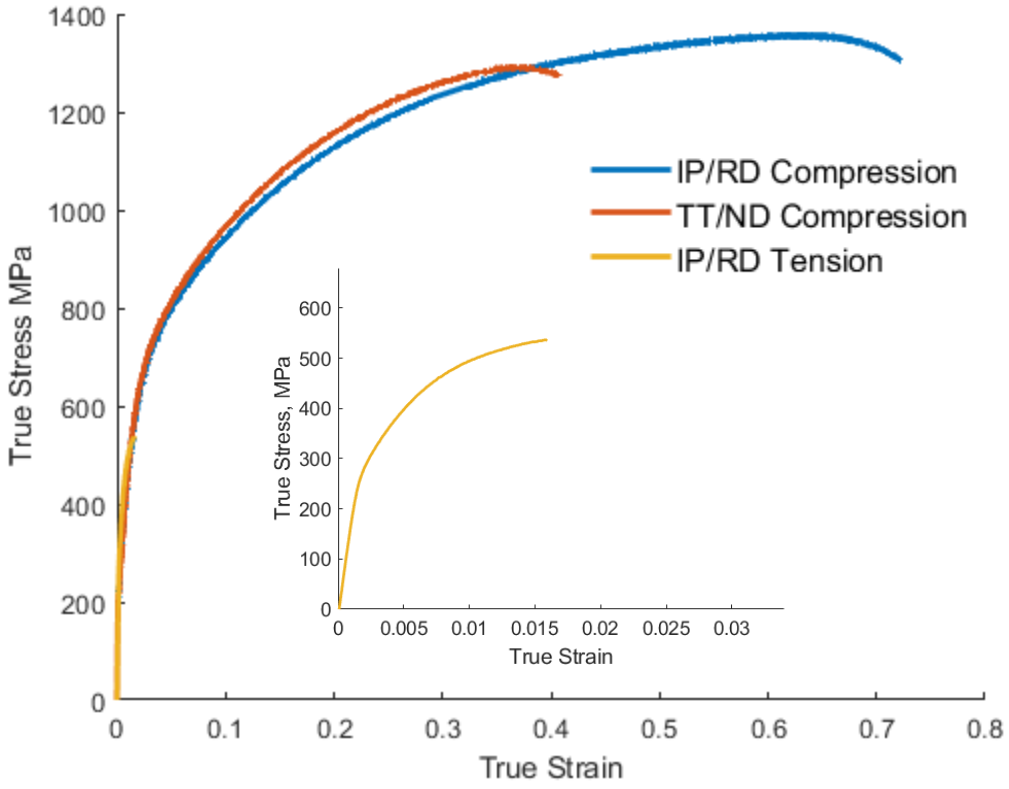

Fig. 1: True stress – true strain curves for the as-rolled specimens of the alloy tested along IP and TT directions in compression and along IP direction in tension to fracture. The plot of the tensile curve is zoomed in for clarity.

3.2 Microstructural characteristics

Inverse pole figure (IPF) maps and corresponding phase maps of the alloy are shown in Fig. 2 for the TT direction. Four phases are identified with green, red, yellow, and blue colors which correspond to γ-austenite, ε-martensite, σ-sigma, and α-ferrite phases, respectively. We would like to point out that ferrite phase designation is specific to one of the BCC phases in

steels. Since our material has quite a complex composition which is not exactly steel, simply calling the ferrite phase as BCC phase may be more appropriate. From the perspective of indexing and determining the type of lattice giving the best fit for a given pattern in EBSD, α-ferrite, δ-ferrite, or α-martensite have no difference because they all have similar lattice constants. As will be shown shortly in an image quality (IQ) map, the BCC phase in the HEA is not the α-martensitic because the intensity is low. Phase fractions based on multiple maps are indicated in the caption. The as-received initial material consists predominantly of γ phase with α being the least prevalent. The average grain size for γ was estimated to be 20 μm for the as rolled samples.

Another IPF map along with its phase map, and an energy dispersive spectroscopy (EDS) elemental map was taken. Luckily the map included more of the BCC phase, and we selected it to perform nanoindentation as indicated in the phase map. γ-austenite and ε-martensite are a solid solution of all 5 elements (Fe, Mn, Co, Cr, Si), and σ-phase is an intermetallic with increased Cr content in a tetragonal structure. Further analyses showed that the σ phase also has a higher Si content. Interestingly, the BCC phase also shows more of Cr. We have added a black overlay highlight for the BCC phase in the Cr composition map. With a higher percentage of Cr in wt%, there is a higher probability of σ-sigma phase forming in stainless steels [34]. In our case, using Si in addition to Cr in higher amounts for Fe-Mn-Co-Cr systems turned out that we got more σ-sigma precipitation [35, 36]. The kernel average misorientation (KAM) map of the initial structure shows a slightly higher presence of geometrically necessary dislocations (GNDs) in the σ-phase relative to the other phases.

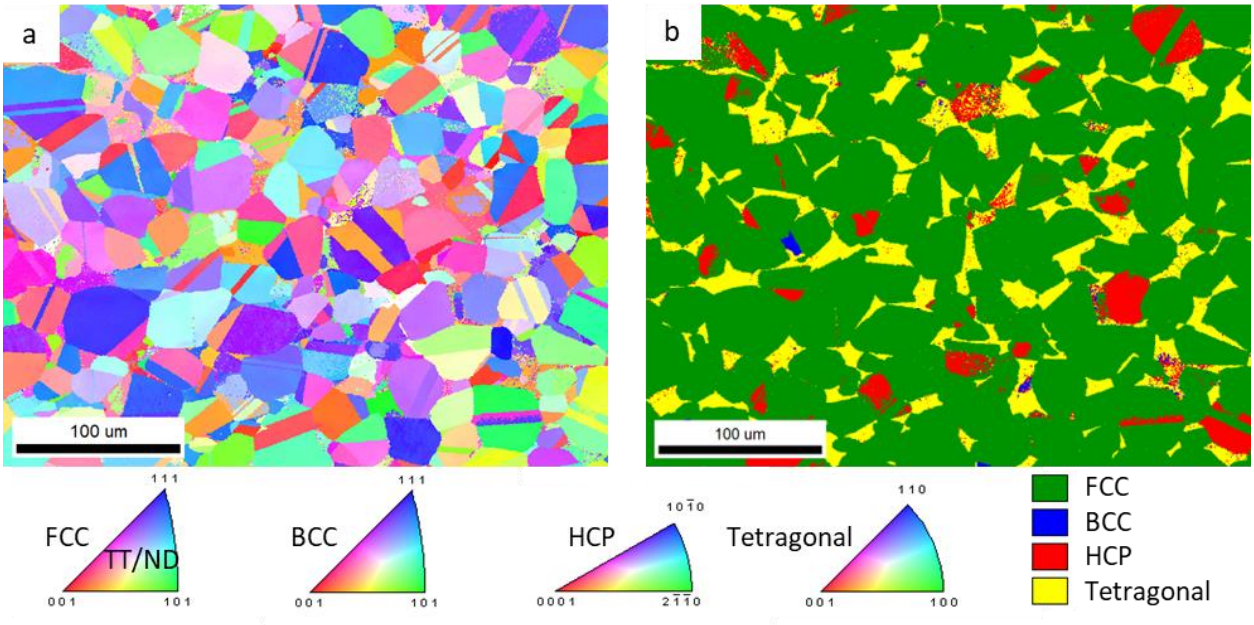

Fig. 2: (a) IPF and (b) phase maps for a specimen of the as-rolled HEA plate. Perpendicular to the maps is the sample TT direction. The colors in the IPF map represent the orientation of the TT/ND plate axis with respect to the crystal lattice frames according to the coloring in the standard IPF triangles per phase. Multiple maps are used to determine the initial average phase fractions: FCC: 78.4%, HCP: 6.2%, BCC: 0.4%, and Tetragonal: 15.0%.

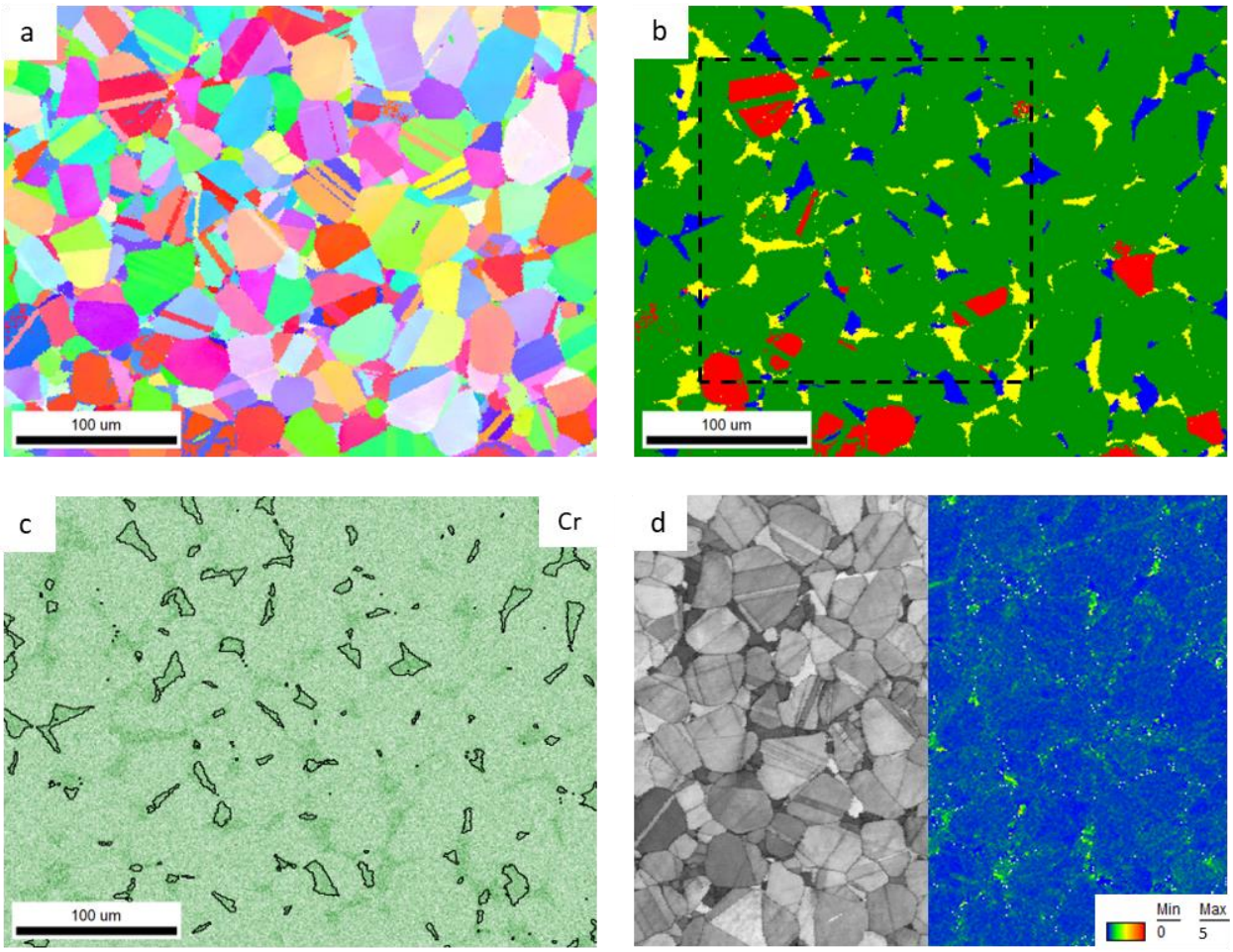

Fig. 3: (a) IPF, (b) phase, (c) EDS Cr composition, (d) half IQ and half KAM maps for a specimen of the as-rolled HEA plate. The frames and colors in the IPF map are the same as those in Fig. 1. The colors in the phase map are the same as those in Fig. 1. The composition map reveals a higher Cr content in the BCC and Tetragonal phases. The IQ and KAM maps show relatively low dislocation density in all phases.

Fig. 4 shows the structure in the alloy at an intermediate strain level and at fracture using IPF and phase maps. Substantial refinement of the structure due to the transformation $\gamma \rightarrow \varepsilon$ can be observed. The maps show slip bands in γ as sheaves of parallel laths that are strung out on the

{111}γ planes carrying out the strain-induced γ→ε martensite transformation. Increasing the content of interfaces in the microstructure with the refinement during deformation increases barriers to mobile dislocations. Such hardening mechanisms are referred to as the dynamic Hall-Petch-type effect. The ability of the alloy to plasticity deform is exhausted with near completion of the transformation. Fig. 5 shows the extent of the transformation with plastic strain under compression measured using EBSD. Crystal orientations with their < 001 > axes parallel to a compression direction easily transform, while crystal orientations compressed around < 011 > and < 111 > cannot transform under compression [37, 38]. The KAM maps of the deformed structures are shown in Fig. 6. Evidently, the presence of GNDs increases in the transforming and deforming phases, ε and γ, while it is smaller in the σ phase. Increased content of dislocations contributes to the local hardness of the phases and also the overall hardening of the alloy.

Fig. 7 shows pole figures of the initial and deformed structures per phase. Texture in the γ phase features the formation of the $\{110\}_{\gamma}$ fiber as expected for compressive of an FCC material [39]. The texture evolution in the ε phase is mainly driven by the TRIP mechanism. The relationship between orientations in the parent γ and child ε phases is $\{111\}_{\gamma}\{0001\}_{\varepsilon}$, $\langle 110\rangle_{\gamma}\langle 2\bar{1}\bar{1}0\rangle_{\varepsilon}$ [40, 41]. Additionally, these two phases are co-deforming by crystallographic slip. Finally, the texture in the σ phase is relatively random and remains such during the compression deformation because the phase does not deform plastically but only floats in the matrix.

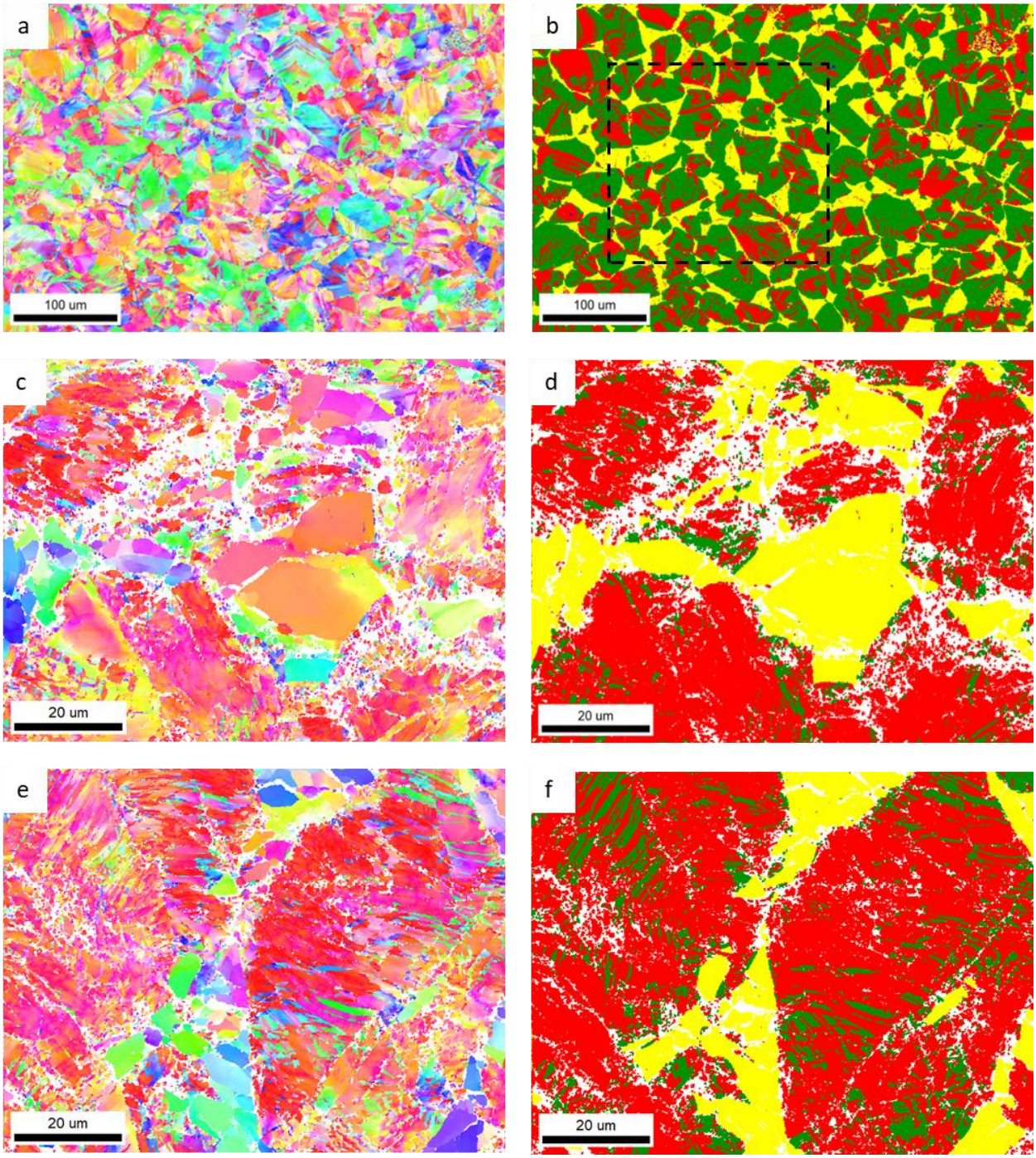

Fig. 4: (a, c, e) IPF and (b, d, f) phase maps for: (a, b) a specimen compressed to 0.21 true strain along TT and (c-f) a specimen compressed to fracture along TT (~0.43 true strain). The frames and colors in the IPF maps are the same as those in Fig. 1. The colors in the phase maps are the same as those in Fig. 1. Multiple maps are used to determine the average phase fractions at 0.21:

FCC: 53%, HCP: 32%, BCC: 0%, and Tetragonal: 15.0%, while at 0.43: FCC: 12%, HCP: 73%, BCC: 0%, and Tetragonal: 15.0%.

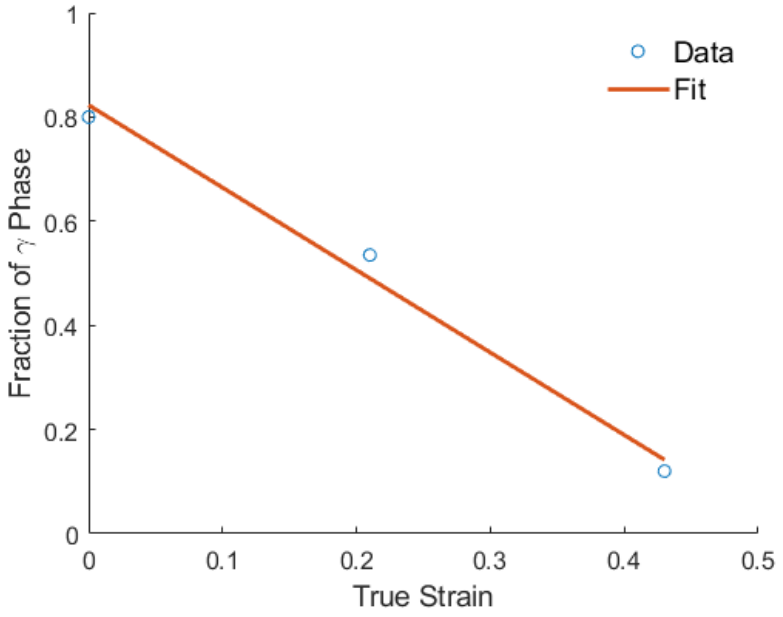

Fig. 5: γ→ε phase fraction transformation from as-rolled material to fracture along TT. The fit is y = -1.48x + 0.82.

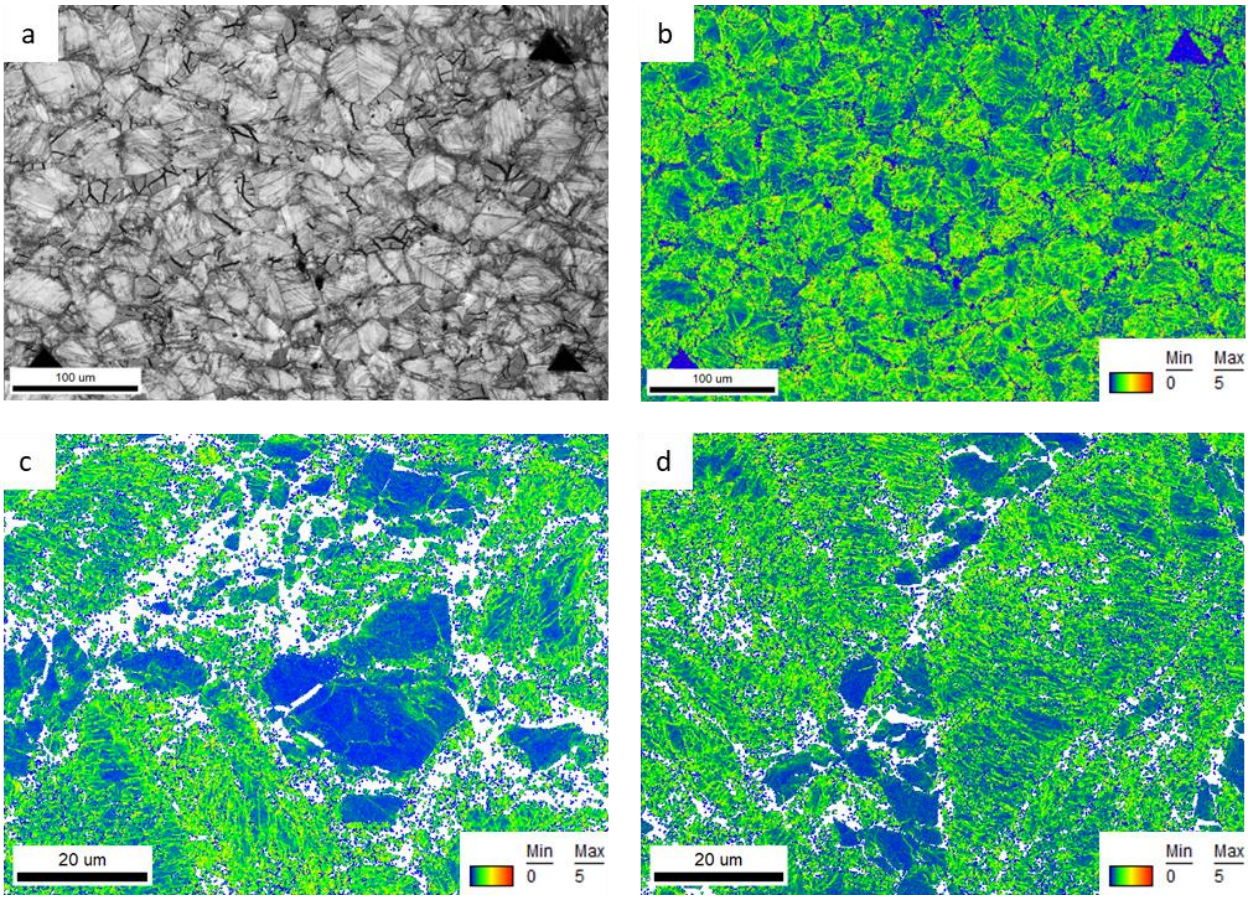

Fig. 6: (a) IQ and (b) KAM maps corresponding to the IPF and phase maps in Fig. 4a and b. (c, d) KAM maps corresponding to the IPF and phase maps in Fig. 4c-f.

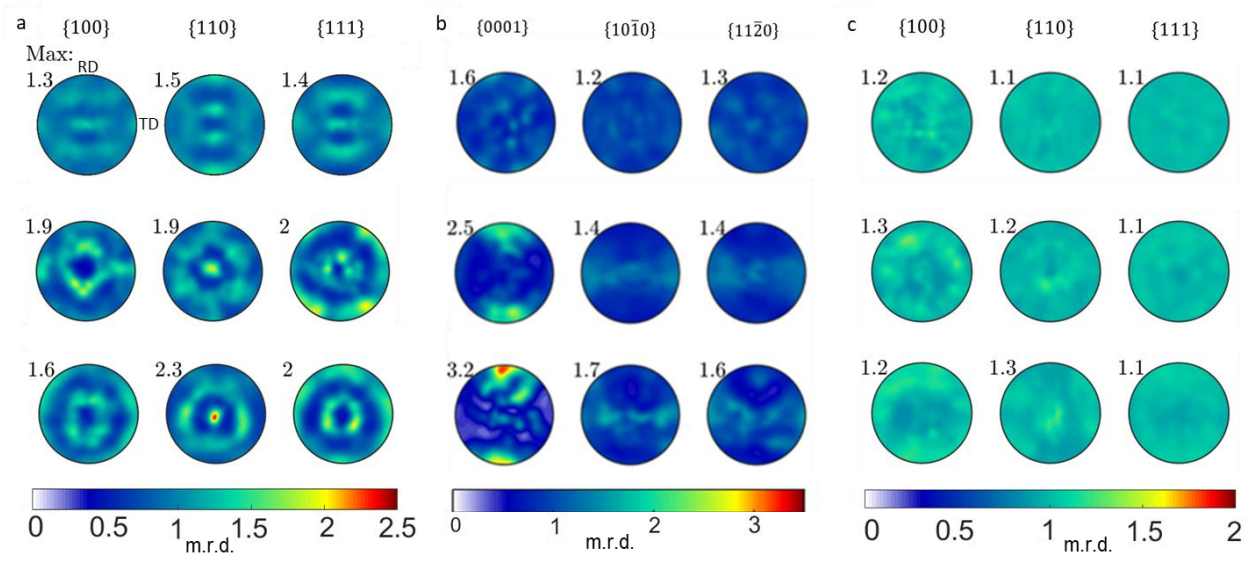

Fig. 7: Stereographic pole figures measured by NeD revealing the evolution of texture per phase in the alloy during compression from initial (top row), to a strain of 0.21 (middle row), and to a strain of 0.43 (bottom row) in (a) austenite, (b) epsilon martensite, and (c) sigma phases.

3.3 Correlated EBSD and nanoindentation mapping for local properties

Initial and strained specimens are subjected to nanoindentation along the TT direction. Two 150x150 µm maps containing 22,500 individual indentations are presented. Appendix A discusses the role of resolution on the results in detail. Fig. 8 displays phase, hardness, correlated phase and hardness, and Young's modulus maps for an initial as-rolled specimen. These maps are the same inner dashed area displayed in Fig. 3b. The KLA software could not distinguish between γ and ε phases based upon hardness alone due to their relative hardness being similar to one another. Integrated software threshold methods to try to separate γ and ε were attempted but were found to be too inaccurate with respect to EBSD phase fraction findings, and therefore their

relative harnesses were calculated together. Fig. 4c shows this phenomenon where only three colors, blue (γ and ε), pink (BCC), and yellow (σ) are shown. σ has the highest hardness. Table 1 presents the average values. The values were verified by performing individual indents per phase using the instrument in both load and displacement control.

Next, measurements of hardness at a higher strain level were conducted. The same procedure as discussed in Fig. 8 was administered for a second specimen pre-compressed to a strain of 0.21. Fig. 9 displays phase, hardness, and correlated phase and hardness maps. These maps are over the same inner dashed area displayed in Fig. 4b. Multiple attempts were made to find and indent the deformed BCC phase, but the phase was never found due to its small volume fraction in the alloy. As for the as-received sample, Fig. 9c correlates phase fractions based upon hardness values. Again, distinguishing between the hardness of γ and ε phases shown in blue was not possible. The relative hardness of γ and ε increased with increasing strain and increased phase fraction of ε. In contrast, the hardness of σ decreased, which is an interesting finding. The finding will be rationalized shortly. Table 2 presents the averaged values. These values were also verified by performing individual indents per phase using the instrument in both load and displacement control.

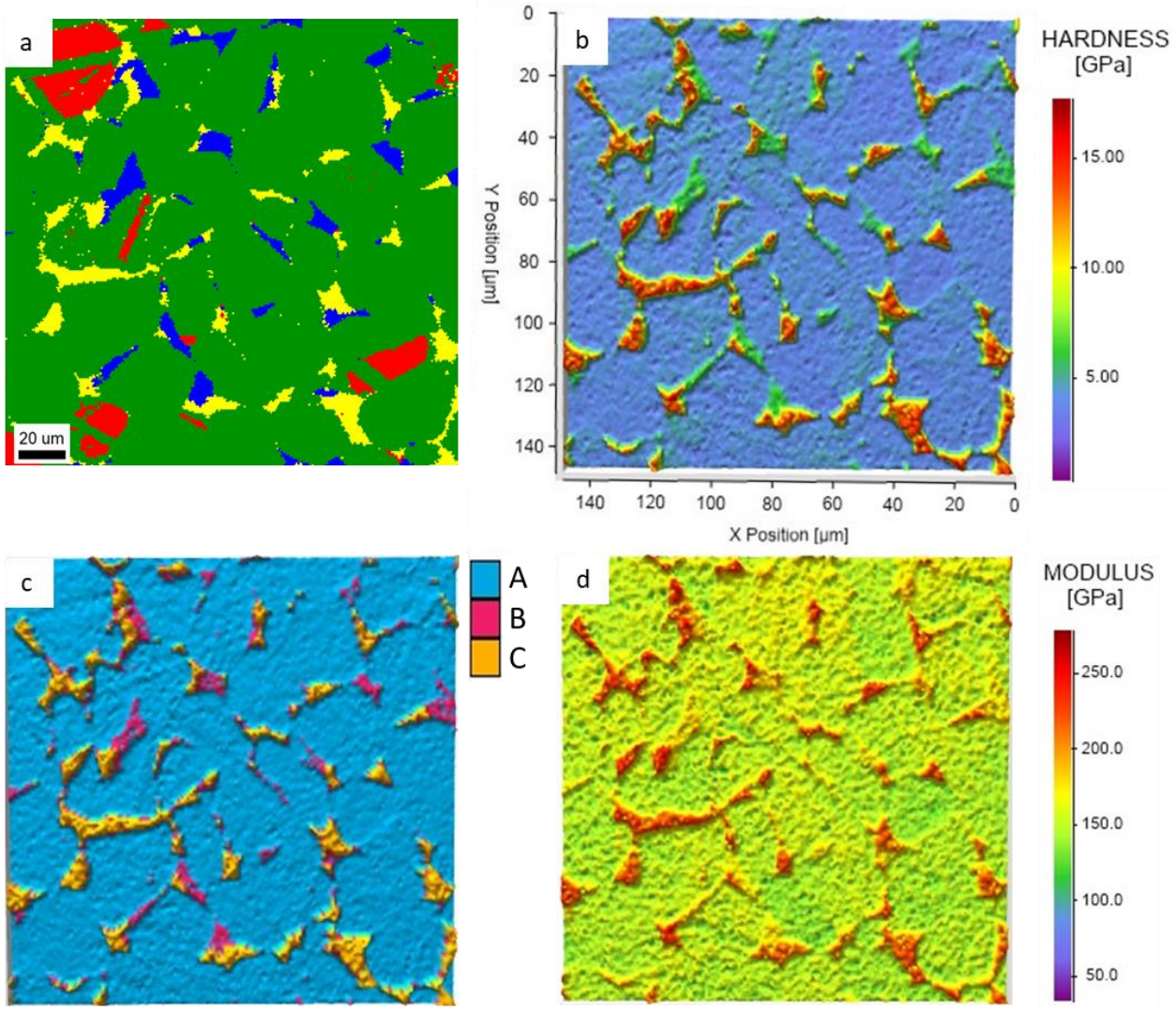

Fig. 8: (a) A sub area of the phase map from Fig. 3b used for nanoindentation to obtain: (b) a hardness map, (c) a correlated phase and harness map, and (d) a Young's modulus map.

Table 1. H_{IIT} and E_{IIT} along with their standard deviation (STDEV) per phase.

Phase	Hardness Mean [GPa]	Hardness STDEV	Modulus Mean [GPa]	Modulus STDEV
A	3.563	0.479	119.2	8.62
B	7.009	0.348	149.4	6.92
C	13.380	1.056	208.5	12.7

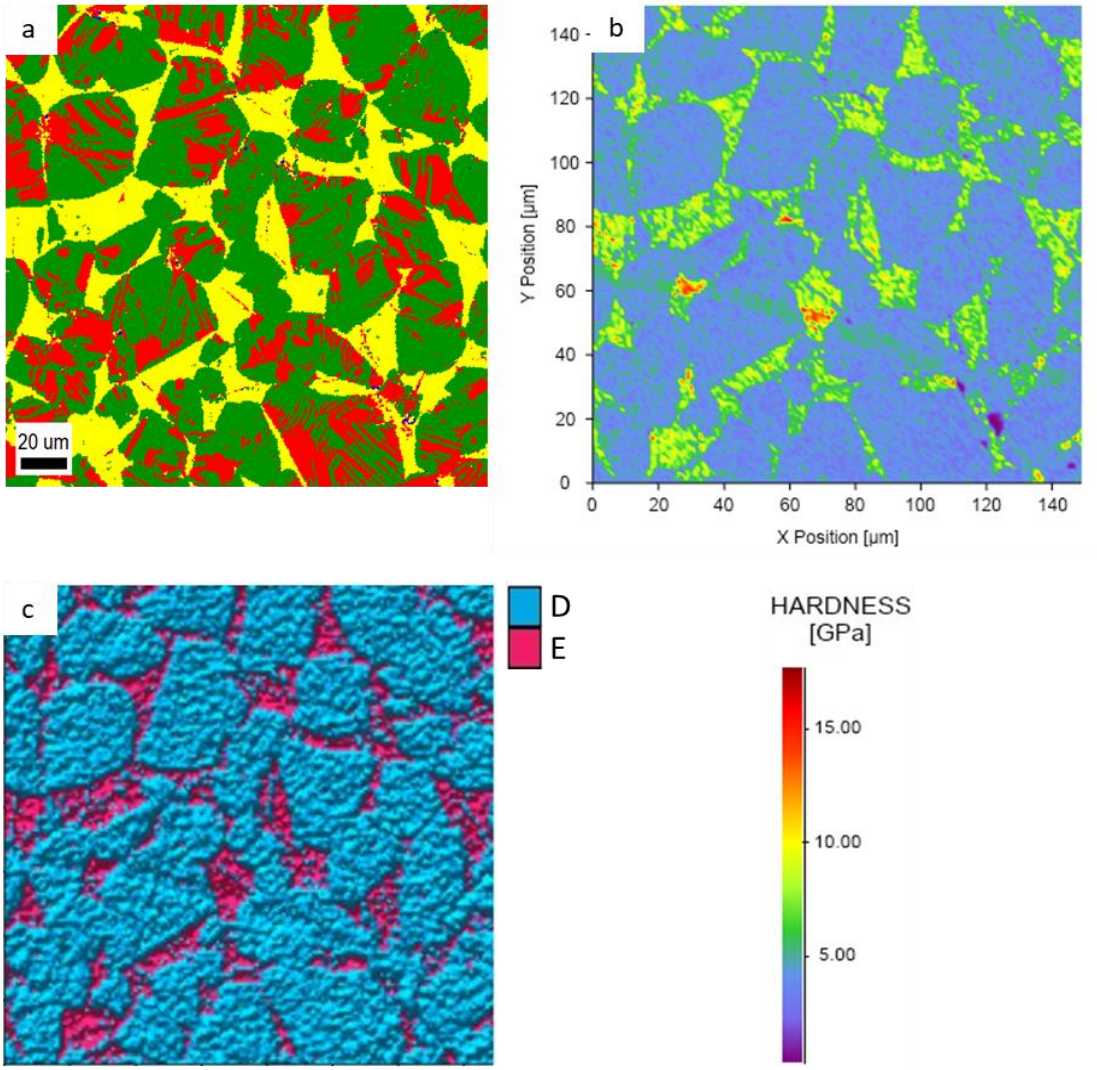

Fig. 9: (a) A sub area of the phase map from Fig. 4b used for nanoindentation to obtain: (b) a hardness map and (c) a correlated phase and harness map.

.

Table 2. H_{IIT} and E_{IIT} along with their standard deviation per phase.

Phase	Hardness Mean [GPa]	Hardness STDEV
D	4.114	0.589
E	8.145	1.699

4. Discussion

Results presented in the previous section in terms of the evolution of microstructure and local behavior of the alloy are used to rationalize and interpret the overall hardening behavior of the alloy. Since nano-hardness response at every individual indent steams from localized microstructural heterogeneities, contributions from strengthening mechanisms such as dislocations and solid solutions to the overall strength can be inferred [42, 43]. In the present study, nano indentation is used to rule out the contribution of dislocation buildups to the strength of the alloy. Phases γ and ε are found to exhibit similar hardness with plastic straining revealing that increasing the fraction of the dislocated ε phase during deformation due to the transformation is not a primary source of strain hardening. Nevertheless, both γ and ε phases exhibit moderate hardening owing to the increase in dislocation density. Measurements suggest an increase in strength due to dislocations of about 15%. Table 3 presents estimated HV based on the H_{IIT} measurements. The relationship between HV and flow stress can be approximated using Tabors equation where HV is first converted from kg_f/mm^2 to MPa by multiplying the HV values by 9.80665 and then dividing by a factor of ~4 or so. In doing so, the initial yield stress of the alloy would be 820 MPa, while that at 0.21 true strain would be 950 MPa based on the HV values for the FCC/HCP phases. The actual yielding of the alloy under compression is at about

600 MPa, while flow strength at 0.21 true strain is 1180 MPa. Evidently, estimates based on HV are inaccurate as is often the case for multi-phase materials. Therefore, the origin of the strength differential from yielding to that at 0.21 true strain can not be owing to solely dislocation driven hardening of individual phase.

The refinement of the structure during the transformation inducing a dynamic Hall-Petch-type barrier effect is a primary source of hardening in the alloy. Restricting the slip length associated with dislocations in γ and ε is found very effective in strain hardening of the alloy. Effective strengthening by structural refinement has been achieved in many HEAs [44, 45].

Moreover, some load transfer between phases contribution to strengthening likely operates under deformation, given the composite structure of the alloy. Such contribution is driven by the volume fraction, morphology, and strength/stiffness of the reinforcement σ phase [46, 47]. Fig. 10 shows images of the structure revealing networks of cracks developing in the σ phase during compression. The σ phase does not deform/reorientate/float but interestingly begins to crack and fragment with plastic strain. The fragments float around in the surrounding γ and ε matrix. It is found that the hardness of the σ phase decreased with the plastic strain in compression. The decrease in the relative hardness of σ is because the nano indenter tip deflects from the cracked floating phase in the surrounding matrix instead of loading uniaxially. As a result of such softening, any load transfer hardening would decrease.

The present study confirmed that the high throughput nanoindentation mapping is an effective way to characterize the relative strength of phases in multi-phase materials. Large quantities of identical tests were performed within relatively short timescales as compared to more traditional methods [48, 49]. While the technique can probe even more complex microstructures consisting of dislocation structures or nanotwins at nano and micro scales,

results attained in the present study show nano-hardness per phase and the evolution of harness per phase during deformation. The increase/decrease in the relative strength per phases was determined for the $Fe_{42}Mn_{28}Co_{10}Cr_{15}Si_5$ (in at%) HEA. However, there are some limitations of the nanoindentation mapping approach. For example, distinguishing separate phases based upon hardness is not possible for phases with similar hardness values, like γ and ε in the present work. Measured values are useful to compare the relative strength of phases while the actual strength cannot be measured. Nevertheless, assessing relative strength between phases is very useful for the development of crystal plasticity models for multi-phase materials [50]. Given the relative strength per phase, the models would be enabled to partition plastic strain accommodation by individual phases in complex high entropy alloys. The combination of nanoindentation experimental approach and advanced crystal plasticity modeling handling phase transformations approach [51] can determine strength per phase along with the evolution of strength and microstructure. The approach will be pursued in future works.

In closing, we show fractography of the specimen pulled to fracture in tension. Brittle micromechanisms of fracture can be observed owing to the brittle σ phase. The fracture surface consists of a rough intergranular fracture with some transgranular facets from grain to grain.

Table 3. Estimated HV in kg_f/mm^2 from H_{IIT} in GPa.

Phase	Initial	ε = 0.21
FCC	336	389
HCP	336	389
Tetragonal	1264	769
BCC	662	N/A

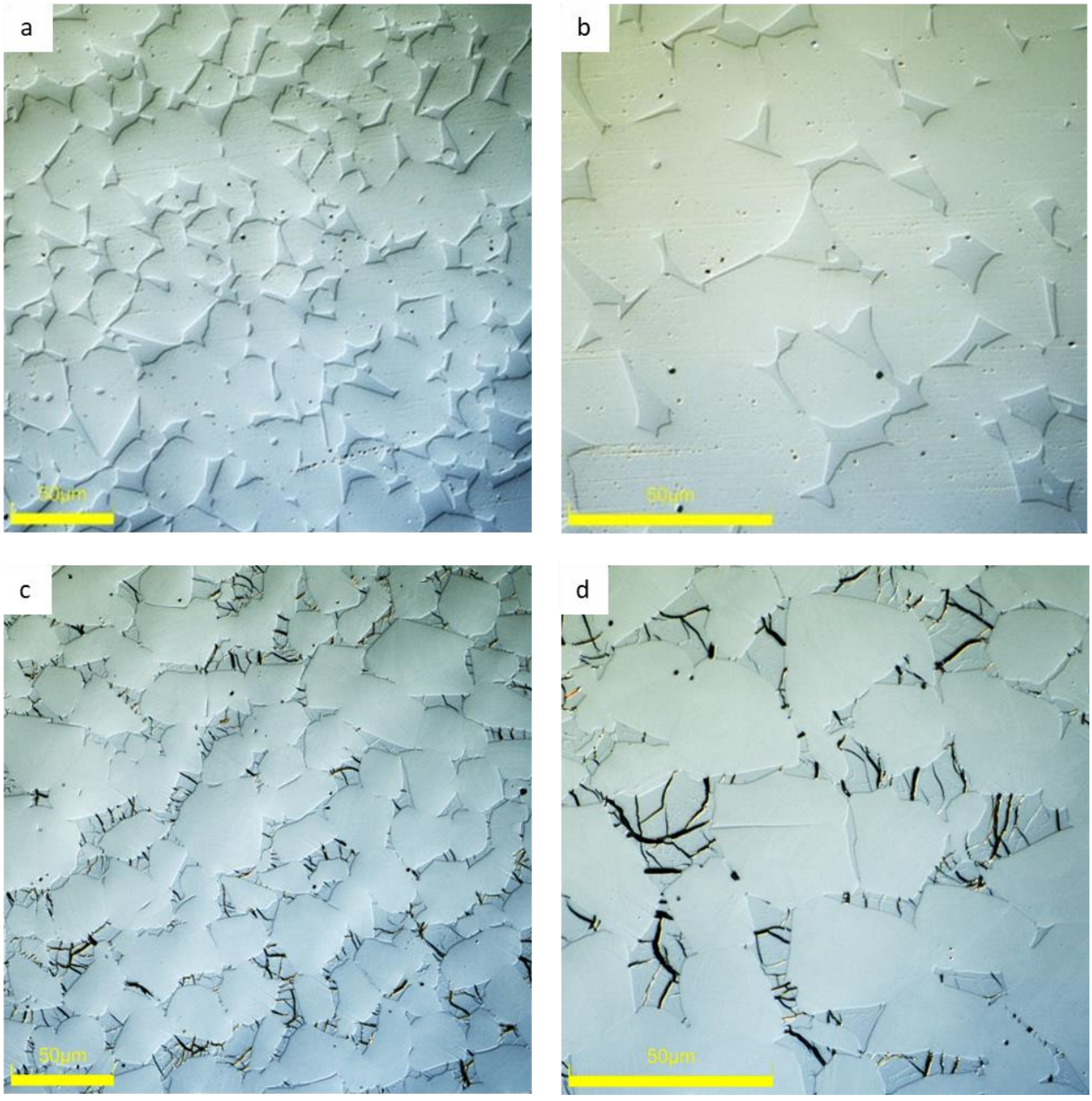

Fig. 10: Optical microscopy images of (a, b) an undeformed initial specimen and (c, d) a compressed specimen along TT to a strain of 0.21. Note networks of cracks developed in sigma

phase after the compression. Perpendicular to the images is the sample TT direction. The scale bars are 50 μm.

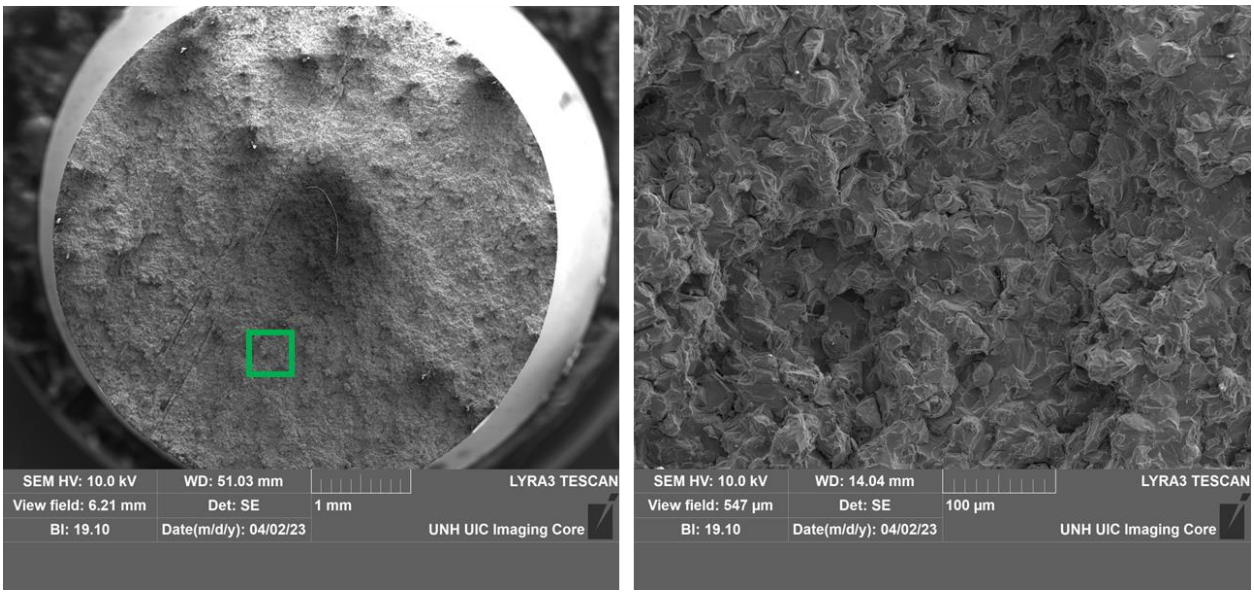

Fig. 11: Secondary electron images showing the fracture surface for a specimen pulled in tension to fracture along RD.

5. Conclusions

In this work, we have characterized the evolution microstructure undergoing strain induced $\gamma \rightarrow \varepsilon$ phase transformation and measured overall strength/ductility in tension and compression along with localized hardness/strength per phase in a quadruplex HEA, $Fe_{42}Mn_{28}Co_{10}Cr_{15}Si_5$ (in at%). The material was investigated in its as-received state and after plastic straining under compression. The emphasis was on assessing the evolution of relative

hardness/strength between individual phases via high-throughput nanoindentation to clarify the origins of strain hardening of the alloy. The main conclusions of the study are:

- The overall behavior of the alloy in compression features a great deal of plasticity and strain hardening before fracture. The plasticity is accommodated through the strain induced $\gamma \rightarrow \varepsilon$ phase transformation to near completion along with dislocation slip in metastable γ and stable ε phases.
- Phases γ and ε are found to exhibit similar hardness with plastic straining revealing that increasing the fraction of the dislocated ε phase during deformation due to transformation is not a primary source of strain hardening. Nevertheless, both γ and ε phases exhibit moderate hardening owing to the increase in dislocation density.
- The contents of diffusion created σ phase remains constant during deformation. The phase floats in the surrounding matrix before beginning to crack at higher strain levels. Cracking and fragmentation of the phase during deformation causes localized softening but not early fracture under compression.
- The primary source of strain hardening in the alloy is the refinement of the structure during the transformation inducing a dynamic Hall-Petch-type barrier effect. The secondary sources are owing to the build up of dislocations in the γ and ε phases with plastic strain and to some load transfer because of the strength/stiffness differential between constituent phases.
- The alloy is found to behave poorly under tension. Fracture surfaces after tension feature brittle micromechanisms of fracture. Such behavior is attributed to the presence of the brittle σ phase. Future work will focus on designing new compositions to suppress the occurrence of the σ phase.

Acknowledgements

This research was supported by the DEVCOM Army Research Laboratory under cooperative agreement no. W911NF-21-2-0149 and the U.S. National Science Foundation under grant no. OIA-1757371.

Data availability

The raw/processed data required to reproduce these findings cannot be shared at this time due to technical or time limitations.

Appendix

Because conducting high-speed nanoindentation mapping and interpreting its results requires appropriate indentation spacing and indentation depth, this appendix presents indents/imprints in specimens after nanoindentation. The results are shown at two applied force levels, 750 μN and 1750 μN. Spacing between indents was 1 μm for both loads, as recommended for sufficient resolution contour plots. The spacing is defined as the distance between the center of one indent to the center of the next. The spacing must also be optimized to prohibit interference between adjacent indents while maximizing indentation coverage for contours of properties over the given grain structures. 0.5 μm between the most right corner of

one indent to the most left corner of another is recommended as optimal to allow for the indents to be as close to one another as possible without interfering. While we have explored broad ranges of spacings and forces for achieving good looking and accurate maps, we chose to show indents under two forces in Fig. A1. Results based on the two loads were very similar and within the standard deviation. However, we regard the second force as an upper bound for achieving accurate results in both phases simultaneously for 1 μm spacing because the indents begin to interact in the FCC/HCP phases. Further increase in the load would still provide accurate measurements in the Tetragonal phase but not in the FCC/HCP phases. Average depth, h_c, over indents was 105 nm in FCC/HCP, 75 nm in BCC, and 55 nm in Tetragonal under 750 μN, while 135 nm in FCC/HCP and 70 nm in Tetragonal under 1750 μN force. The 22,500 indent maps took 6.15 hours to complete, which is approximately 1 second per indent.

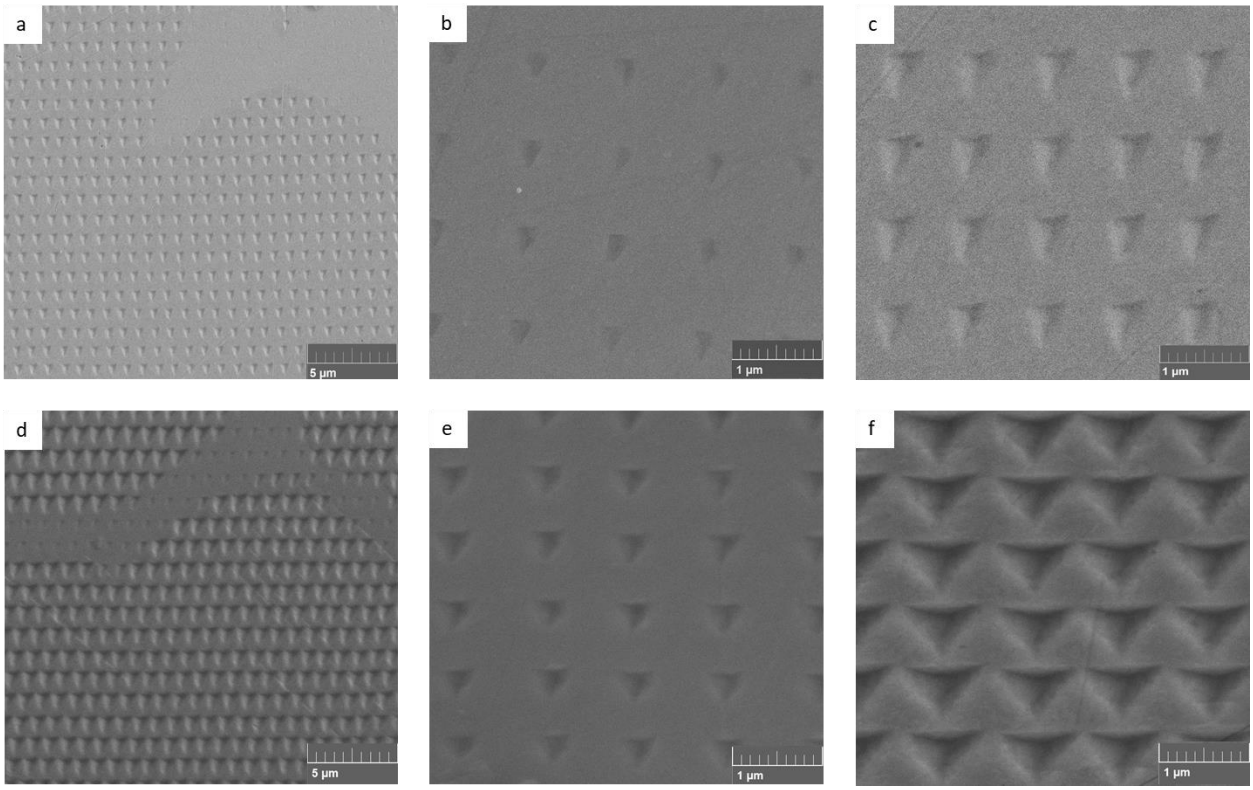

Fig. A1: Secondary electrons images showing indents under (a, b, c) 750 µN force and (d, e, f) 1750 µN force. (b) is a magnified region from (a) in σ phase. (c) is a magnified region from (a) in γ and ε phases. (e) is a magnified region from (d) in σ phase. (f) is a magnified region from (d) in γ and ε phases.

References

[1] B. Cantor, Multicomponent and high entropy alloys, Entropy, 16 (2014) 4749-4768.

[2] J.W. Yeh, S.K. Chen, S.J. Lin, J.Y. Gan, T.S. Chin, T.T. Shun, C.H. Tsau, S.Y. Chang, Nanostructured high-entropy alloys with multiple principal elements: novel alloy design concepts and outcomes, Advanced engineering materials, 6 (2004) 299-303.

[3] B. Cantor, Multicomponent and High Entropy Alloys, Entropy, 2014, pp. 4749-4768.

[4] Z. Li, K.G. Pradeep, Y. Deng, D. Raabe, C.C. Tasan, Metastable high-entropy dual-phase alloys overcome the strength–ductility trade-off, Nature, 534 (2016) 227-230.

[5] Z. Li, C.C. Tasan, K.G. Pradeep, D. Raabe, A TRIP-assisted dual-phase high-entropy alloy: Grain size and phase fraction effects on deformation behavior, Acta. Mater., 131 (2017) 323-335.

[6] Y. Deng, C.C. Tasan, K.G. Pradeep, H. Springer, A. Kostka, D. Raabe, Design of a twinning-induced plasticity high entropy alloy, Acta Materialia, 94 (2015) 124-133.

[7] Z. Li, D. Raabe, Strong and ductile non-equiatomic high-entropy alloys: design, processing, microstructure, and mechanical properties, Jom, 69 (2017) 2099-2106.

[8] M.J. Yao, K.G. Pradeep, C.C. Tasan, D. Raabe, A novel, single phase, non-equiatomic FeMnNiCoCr high-entropy alloy with exceptional phase stability and tensile ductility, Scripta Materialia, 72-73 (2014) 5-8.

[9] B. He, B. Hu, H. Yen, G. Cheng, Z. Wang, H. Luo, M. Huang, High dislocation density–induced large ductility in deformed and partitioned steels, Science, 357 (2017) 1029-1032.

[10] S. Bhowmik, J. Zhang, S.C. Vogel, S.S. Nene, R.S. Mishra, B.A. McWilliams, M. Knezevic, Effects of plasticity-induced martensitic transformation and grain refinement on the evolution of microstructure and mechanical properties of a metastable high entropy alloy, J. Alloys Compd., 891 (2022) 161871.

[11] Y. Zhang, T.T. Zuo, Z. Tang, M.C. Gao, K.A. Dahmen, P.K. Liaw, Z.P. Lu, Microstructures and properties of high-entropy alloys, Progress in Materials Science, 61 (2014) 1-93.

[12] N. Kumar, M. Komarasamy, P. Nelaturu, Z. Tang, P.K. Liaw, R.S. Mishra, Friction Stir Processing of a High Entropy Alloy Al0.1CoCrFeNi, JOM, 67 (2015) 1007-1013.

[13] E. Galindo-Nava, P. Rivera-Díaz-del-Castillo, Understanding martensite and twin formation in austenitic steels: A model describing TRIP and TWIP effects, Acta Materialia, 128 (2017) 120-134.

[14] R. Xiong, H. Peng, H. Si, W. Zhang, Y. Wen, Thermodynamic calculation of stacking fault energy of the Fe–Mn–Si–C high manganese steels, Materials Science and Engineering: A, 598 (2014) 376-386.

[15] A.K. Nair, E. Parker, P. Gaudreau, D. Farkas, R.D. Kriz, Size effects in indentation response of thin films at the nanoscale: A molecular dynamics study, International Journal of Plasticity, 24 (2008) 2016-2031.

[16] C.J. Ruestes, E.M. Bringa, Y. Gao, H.M. Urbassek, Molecular dynamics modeling of nanoindentation, Applied nanoindentation in advanced materials, (2017) 313-345.

[17] C.J. Ruestes, I.A. Alhafez, H.M. Urbassek, Atomistic studies of nanoindentation—A review of recent advances, Crystals, 7 (2017) 293.

[18] N.X. Randall, M. Vandamme, F.-J. Ulm, Nanoindentation analysis as a two-dimensional tool for mapping the mechanical properties of complex surfaces, Journal of Materials Research, 24 (2009) 679-690.

[19] C. Tromas, M. Arnoux, X. Milhet, Hardness cartography to increase the nanoindentation resolution in heterogeneous materials: Application to a Ni-based single-crystal superalloy, Scr. Mater., 66 (2012) 77-80.

[20] I.A. Alhafez, C.J. Ruestes, E.M. Bringa, H.M. Urbassek, Nanoindentation into a high-entropy alloy–An atomistic study, Journal of Alloys and Compounds, 803 (2019) 618-624.

[21] C.J. Ruestes, D. Farkas, Dislocation emission and propagation under a nano-indenter in a model high entropy alloy, Computational Materials Science, 205 (2022) 111218.

[22] C. Varvenne, A. Luque, W.G. Nöhring, W.A. Curtin, Average-atom interatomic potential for random alloys, Physical Review B, 93 (2016) 104201.

[23] R. Pasianot, D. Farkas, Atomistic modeling of dislocations in a random quinary high-entropy alloy, Computational Materials Science, 173 (2020) 109366.

[24] I. Basu, J.T.M. De Hosson, Strengthening mechanisms in high entropy alloys: fundamental issues, Scripta Materialia, 187 (2020) 148-156.

[25] Y. Qi, H. Xu, T. He, M. Feng, Effect of crystallographic orientation on mechanical properties of single-crystal CoCrFeMnNi high-entropy alloy, Materials Science and Engineering: A, 814 (2021) 141196.

[26] S. Shuang, S. Lu, B. Zhang, C. Bao, Q. Kan, G. Kang, X. Zhang, Effects of high entropy and twin boundary on the nanoindentation of CoCrNiFeMn high-entropy alloy: A molecular dynamics study, Computational Materials Science, 195 (2021) 110495.

[27] D.-Q. Doan, T.-H. Fang, T.-H. Chen, Microstructure and composition dependence of mechanical characteristics of nanoimprinted AlCoCrFeNi high-entropy alloys, Scientific reports, 11 (2021) 1-19.

[28] E.D. Hintsala, U. Hangen, D.D. Stauffer, High-throughput nanoindentation for statistical and spatial property determination, Jom, 70 (2018) 494-503.

[29] Y. Chen, E. Hintsala, N. Li, B.R. Becker, J.Y. Cheng, B. Nowakowski, J. Weaver, D. Stauffer, N.A. Mara, High-throughput nanomechanical screening of phase-specific and temperature-dependent hardness in Al x FeCrNiMn high-entropy alloys, Jom, 71 (2019) 3368-3377.

[30] Q. Fan, K. Gan, D. Yan, Z. Li, Nanoindentation creep behavior of diverse microstructures in a pre-strained interstitial high-entropy alloy by high-throughput mapping, Materials Science and Engineering: A, 856 (2022) 143988.

[31] W.C. Oliver, G.M. Pharr, Improved technique for determining hardness and elastic modulus using load and displacement sensing indentation experiments, Journal of Materials Research, 7 (1992) 1564-1580.

[32] H.-R. Wenk, L. Lutterotti, S. Vogel, Texture analysis with the new HIPPO TOF diffractometer, Nuclear Instruments and Methods in Physics Research Section A: Accelerators, Spectrometers, Detectors and Associated Equipment, 515 (2003) 575-588.

[33] S. Pathak, S.R. Kalidindi, Spherical nanoindentation stress–strain curves, Materials Science and Engineering: R: Reports, 91 (2015) 1-36.

[34] T. Liang, X.Q. Hu, X.H. Kang, D.Z. Li, Effect of The Sigma Phase on the Mechanical Properties of a Cast Duplex Stainless Steel during the Ageing Treatment at 850°C, Advanced Materials Research, 684 (2013) 325-329.

[35] S.S. Nene, M. Frank, P. Agrawal, S. Sinha, K. Liu, S. Shukla, R.S. Mishra, B.A. McWilliams, K.C. Cho, Microstructurally flexible high entropy alloys: Linkages between alloy design and deformation behavior, Materials & Design, 194 (2020) 108968.

[36] C.-C. Hsieh, W. Wu, Overview of intermetallic sigma (σ) phase precipitation in stainless steels, International Scholarly Research Notices, 2012 (2012) 732471.

[37] E. Polatidis, W.N. Hsu, M. Šmíd, T. Panzner, S. Chakrabarty, P. Pant, H. Van Swygenhoven, Suppressed martensitic transformation under biaxial loading in low stacking fault energy metastable austenitic steels, Scr. Mater., 147 (2018) 27-32.

[38] D. Goodchild, W.T. Roberts, D.V. Wilson, Plastic deformation and phase transformation in textured austenitic stainless steel, Acta Metall., 18 (1970) 1137-1145.

[39] Z. Feng, R. Pokharel, S.C. Vogel, R.A. Lebensohn, D. Pagan, E. Zepeda-Alarcon, B. Clausen, R. Martinez, G.T. Gray, M. Knezevic, Crystal plasticity modeling of strain-induced martensitic

transformations to predict strain rate and temperature sensitive behavior of 304 L steels: Applications to tension, compression, torsion, and impact, Int. J. Plast., 156 (2022) 103367.

[40] L. Bracke, L. Kestens, J. Penning, Transformation mechanism of α′-martensite in an austenitic Fe–Mn–C–N alloy, Scr. Mater., 57 (2007) 385-388.

[41] Z. Feng, M. Zecevic, M. Knezevic, Stress-assisted (γ→α′) and strain-induced (γ→ε→α′) phase transformation kinetics laws implemented in a crystal plasticity model for predicting strain path sensitive deformation of austenitic steels, Int. J. Plast., 136 (2021) 102807.

[42] T. Maity, K.G. Prashanth, Ö. Balcı, J.T. Kim, T. Schöberl, Z. Wang, J. Eckert, Influence of severe straining and strain rate on the evolution of dislocation structures during micro-/nanoindentation in high entropy lamellar eutectics, International Journal of Plasticity, 109 (2018) 121-136.

[43] R.S. Ganji, P.S. Karthik, K.B.S. Rao, K.V. Rajulapati, Strengthening mechanisms in equiatomic ultrafine grained AlCoCrCuFeNi high-entropy alloy studied by micro-and nanoindentation methods, Acta Materialia, 125 (2017) 58-68.

[44] W. Fu, Y. Huang, J. Sun, A.H. Ngan, Strengthening CrFeCoNiMn0. 75Cu0. 25 high entropy alloy via laser shock peening, International Journal of Plasticity, 154 (2022) 103296.

[45] Y. Liu, Y. He, S. Cai, Effect of gradient microstructure on the strength and ductility of medium-entropy alloy processed by severe torsion deformation, Materials Science and Engineering: A, 801 (2021) 140429.

[46] M. Wang, M. Knezevic, M. Chen, Effects of Fe content on microstructure and mechanical properties of Al-Y eutectic alloys, Mater. Sci. Eng. A, 863 (2023) 144558.

[47] R. Casati, Aluminum matrix composites reinforced with alumina nanoparticles, Springer, 2016.

[48] K. Tao, F.C. Li, Y.H. Liu, E. Pineda, K.K. Song, J.C. Qiao, Unraveling the microstructural heterogeneity and plasticity of Zr50Cu40Al10 bulk metallic glass by nanoindentation, Int. J. Plast., 154 (2022) 103305.

[49] H. Wang, A. Dhiman, H.E. Ostergaard, Y. Zhang, T. Siegmund, J.J. Kruzic, V. Tomar, Nanoindentation based properties of Inconel 718 at elevated temperatures: A comparison of conventional versus additively manufactured samples, Int. J. Plast., 120 (2019) 380-394.

[50] M. Zecevic, Y.P. Korkolis, T. Kuwabara, M. Knezevic, Dual-phase steel sheets under cyclic tension–compression to large strains: Experiments and crystal plasticity modeling, J. Mech. Phys. Solids, 96 (2016) 65-87.

[51] M. Zecevic, M.V. Upadhyay, E. Polatidis, T. Panzner, H. Van Swygenhoven, M. Knezevic, A crystallographic extension to the Olson-Cohen model for predicting strain path dependence of martensitic transformation, Acta. Mater., 166 (2019) 386-401.

Conclusions and Future Work

This work presented the use of a Taylor Type crystal Plasticity Model for studying the mechanical behavior and microstructural evolution of Mg alloys under various loading conditions and strain rates. In this work it was found that CPFE was able to achieve good agreement in dimensional shape change (anisotropy), texture, evolution, twinning evolution, and dislocation density evolution for high strain rate Taylor Cylinder tests using AZ31 Mg alloy. Extrapolating to higher strain rates than those used in calibration is attributed to physical sources of strain rate sensitivities of each slip and twinning mode including inherent constant structure of strain rate sensitivity and dislocation-based hardening strain rate sensitivity. Work under this thesis also found that the relaxation with six crystals per integration gave the best mechanical field comparison to the full-field model for AZ31, having the most similarities between stress-strain curves, deformation mode activities, and stress-strain deviations when compared with the full field model. One crystal per integration point without explicit grain structure preforms badly due to large heterogeneity caused from the absence of explicit deformation domains. A methodology from this work was produced to identify the appropriate relaxed Taylor-type model and could be used to evaluate other homogenization schemes in finite element frameworks when plasticity is anisotropic and impacted by homogenization assumptions. Lastly, microstructure evolution, phase transformation, and hardness parameters of a low SFE $Fe_{42}Mn_{28}Co_{10}Cr_{15}Si_5$ (in at%), HEA were analyzed using rolling and compression. It was found that phase transformation characteristics could be rationalized by nanoindentation along with EBSD and optical microscopy. A brittle tetragonal phase cracks under compressive strain and floats in the surrounding matrix leading to decreased hardness and relative Vickers hardness values for the phase. Gamma FCC transforms to epsilon HCP under plastic deformation leading to strength

hardening and increased ductility of the material. Strain hardening can be attributed to refinement of the structure during the transformation inducing a dynamic Hall-Petch-type barrier effect The measured nano-hardness is strongly correlated with the microstructural heterogeneities within the material.

The work presented here will be improved upon and iterated via future works. Sajjad Najambad is trying to use explicit grain models with different grain densities in FE simulations to quantify geometrically necessary dislocations (GNDs) and calculate the back stress for pure tantalum. He is trying to take advantage of both phenomenological and crystal plasticity formulations developed by Tasnim Oishi and Russell Marki. Tasnim has been introducing a phenomenological law and implementing reverse dislocation density which will be embedded into the hardening law of CPFE. This will be used to investigate the mechanical behavior of commercially pure Ti under continuous bending under tension (CBT) process.